MICRO/MACROSCOPIC FLUID FLOW IN OPEN CELL FIBROUS STRUCTURES

by

Ali Tamayol
M.Sc., Sharif University of Technology, 2005
B.Sc. (Mechanical Engineering), Shiraz University, 1999

DISSERTATION SUBMITTED IN PARTIAL FULFILLMENT OF
THE REQUIREMENTS FOR THE DEGREE OF

DOCTOR OF PHILOSOPHY

In the
Program of Mechatronic Systems Engineering
Faculty of Applied Science

© Ali Tamayol 2011

SIMON FRASER UNIVERSITY

Summer 2011

Approval

Name: **Ali Tamayol**

Degree: **Doctor of Philosophy (PhD)**

Title of Thesis: **MICRO/MACROSCOPIC FLUID FLOW IN OPEN CELL
                       FIBROUS STRUCTURES**

Examining Committee:

                              Chair: _____

                                             Name: Martin Ordonez
                                             Defense Chair
                                             Assistant Professor

                                             _____

                                             Name: Majid Bahrami
                                             Senior Supervisor
                                             Assistant Professor

                                             _____

                                             Name: Bonnie L. Gray
                                             Supervisor
                                             Associate Professor

                                             _____

                                             Name: Michael Eikerling
                                             Supervisor
                                             Associate Professor

                                             _____

                                             Name: Behrad Bahrayni
                                             Internal Examiner
                                             Assistant Professor

                                             _____

                                             Name: Sushanta K. Mitra
                                             External Examiner
                                             Associate Professor
                                             University of Alberta

Date Defended/Approved: **July 14, 2011**

ii

Abstract

Fibrous porous materials are involved in a wide range of applications including composite fabrication, filtration, compact heat exchangers, fuel cell technology, and tissue engineering to name a few. Fibrous structures, such as metalfoams, have unique characteristics such as low weight, high porosity, high mechanical strength, and high surface to volume ratio. More importantly, in many applications the fibrous microstructures can be tailored to meet a range of requirements. Therefore, fibrous materials have the potential to be used in emerging sustainable energy conversion applications.

The first step for analyzing transport phenomena in porous materials is to determine the micro/macroscopic flow-field inside the medium. In applications where the porous media is confined in a channel, the system performance is tightly related to the flow properties of the porous medium and its interaction with the channel walls, i.e., macroscopic velocity distribution.

Therefore, the focus of the study has been on:

- developing new mechanistic model(s) for determining permeability and inertial coefficient of fibrous porous materials;

- investigating the effects of microstructural and mechanical parameters such as porosity, fiber orientation, mechanical compression, and fiber distribution on the flow properties and pressure drop of fibrous structures;

- determining the macroscopic flow-field in confined porous media where the porous structure fills the channel cross-section totally or partially.

A systematic approach has been followed to study different aspects of the flow through fibrous materials. The complex microstructure of real materials has been modelled using unit cells that have been assumed to be repeated throughout the media. Implementing various exact and approximate analytical techniques such as integral technique, point matching, blending rules, and scale analysis the flow properties of such media have been modelled; the targeted properties include permeability and inertial coefficient. In addition, fluid flow through microchannels, fully and partially filled with porous media, has been modelled using a volume-averaged equation, which is a novel approach in Microfluidics.

To verify the developed models, several testbeds have been designed and experimental studies have been conducted with various fluids and porous materials. The proposed models have been verified with the measured data and the experimental results reported by others.

Keywords: Fibrous porous media; Permeability; Inertial coefficient; Theoretical modeling; Numerical simulation; Experimental verification; Confined porous media; Metalfoams; Gas diffusion layers; Sustainable energy; Transport phenomena.

Executive Summary

Fibrous porous materials are involved in a wide range of applications including composite fabrication, filtration, compact heat exchangers, paper production, fuel cell technology, and tissue engineering. In comparison with packed beds of spherical particles, fibrous structures have superior characteristics such as low weight, high porosity, high mechanical strength, and high surface to volume ratio. More importantly, in many applications the fibrous microstructures can be tailored to meet a range of requirements. Therefore, fibrous materials have the potential to be used in emerging sustainable energy conversion applications.

Despite numerous existing studies, the transport characteristics of fibrous media are not fully understood. This is one of the several reasons for the current intense worldwide efforts to investigate transport phenomena in such structures. The first step is to determine the macroscopic flow-field inside and at the interface of the medium. As such, the motivation of the present study is to determine pressure drop and both microscopic and macroscopic flow-field in fibrous materials with focus on the following applications:

Fuel cell technology: Gas diffusion layer (GDL) of polymer electrolyte membrane fuel cells (PEMFCs) is a fibrous porous material with a planar structure. In addition to mechanical support of the membrane, GDL allows transport of reactants, products, and electrons from the bipolar plate towards the catalyst layer and vice versa.

In-plane and through-plane gas permeability of GDL affects the PEM fuel cell performance and plays a key role in the design and optimization process of PEMFCs.

Compact heat exchangers: Open cell metalfoams, formed by small ligaments creating interconnected dodecahedral-like cells, have unique features including: excellent surface-area-to-volume ratio, high temperature tolerance, low density (typically with specific gravity of 0.1), high mechanical strength, and corrosion resistance in comparison with regular steel fins. Foams can be constructed from a wide variety of materials including metals (aluminum, nickel, copper, iron, and steel alloys), polymers, and carbon. As a result of recent decrease in production costs, metalfoams have received a special attention as a candidate for designing compact heat exchangers in the past decade. In-depth understanding of flow in metalfoams is important for any thermal and heat exchanger effectiveness analysis

Filtration: Filtration is a common way for separating particles from the bulk fluid. Usually, a porous structure or membrane is used for trapping the targeted particles. The microstructure of a majority of filtering media is fibrous. An understanding of flow-field and the resulting pressure drop is crucial in the design and optimization of filtration systems.

The morphological parameters that are commonly used to describe porous media include: 1) porosity that is the ratio of the void volume to the total volume and 2) fiber diameter. However, in special cases, other parameters have also been used, e.g., the polytetrafluoro ethylene (PTFE) content for GDLs and pore density, number of pores per unit length, typically expressed in pores per inch (PPI), for metalfoams.

In many applications, the porous media is embedded inside a channel (confined porous media), occupying the entire or part of the channel's cross-section. Mini/microchannels filled with porous media (micro-porous channels) are currently used in filtration, detection of particles, compact heat exchanger design, fuel cell technology, and tissue engineering. Such structures have also been used in biological and life sciences for analyzing biological materials such as proteins, DNA, cells, embryos, and chemical reagents. The performance of the abovementioned systems is tightly linked to the flow properties of the porous media and its interaction with the channel walls.

Objectives

The main goals of the proposed research can be summarized as:

- Developing new mechanistic model(s) for the permeability and the inertial coefficient of fibrous porous materials with 1, 2, and 3 directional microstructures.

- Investigating the effects of microstructural and mechanical parameters such as porosity, fiber orientation, mechanical compression, and fiber distribution on the flow properties and pressure drop of fibrous structures.

- Determining the macroscopic flow-field and the resulting pressure drop in confined porous media, where the microstructure totally or partially fills the channel' cross-section.

The developed models will serve as a powerful tool in design and optimization process for engineers and scientist investigating a variety of areas including fuels cell technology, compact heat exchangers, tissue engineering, and filtration.

Methodology

In this study, a systematic approach is adopted to study various aspects of fluid flow through fibrous materials. The problem is divided into smaller parts where analytical and experimental studies are carried out; Figure 1 shows the road map and the deliverables of the thesis.

The focus of the present study is on developing fundamental models that can accurately predict the flow properties of fibrous porous media. The developed fundamental models can be tailored for each specific application through implementing specific morphological parameters. The random, complex microstructure of real porous materials is modeled using unit cells that are assumed to be repeated throughout the volume. Analysis of the considered unit cells enables one to develop compact solutions with a reasonable accuracy. Then, based on the microstructure and flow characteristics, various exact and approximate analytical techniques such as integral technique, point matching, blending rules, and scale analysis are employed to predict the pressure drop and as a result the permeability. Unlike the majority of the existing studies in the literature, the proposed models are applicable to various materials without a need to find a "tuning parameter". In the moderate Reynolds number flows, numerical simulations are performed to propose accurate and compact relationships for predicting the inertial coefficient in the considered microstructures.

To verify the developed models and proposed correlations, three new experimental test beds have been designed and built at Simon Fraser University to conduct experimental studies with various fluids and materials at different scales.

Although the thrust of the present study is to determine the flow properties of GDLs and metalfoams, the reported results and the approach are applicable to any other fibrous material with similar microstructures.

This dissertation is divided into 5 chapters and 3 appendices. Chapter 1 includes an introduction including a theoretical background on flow through fibrous media. A critical review of the pertinent literature is presented is Chapter 2 to justify the necessity for the research. Chapter 3 includes all the microscopic analysis for determining the flow properties (permeability and inertial coefficient) of fibrous structures. Boundary effects on macroscopic velocity distribution and pressure drop in channels partially and fully filled with porous media is investigated in Chapter 4. Summary and conclusions of the dissertation is presented in Chapter 5. This chapter also includes the possible continuations of the current dissertation. Appendix A includes all the experimental and numerical data collected from various sources and used in the dissertation. Details of the experimental measurements performed in the dissertation are listed in Appendix B. More details on the numerical simulations performed in the dissertation are provided in Appendix C.
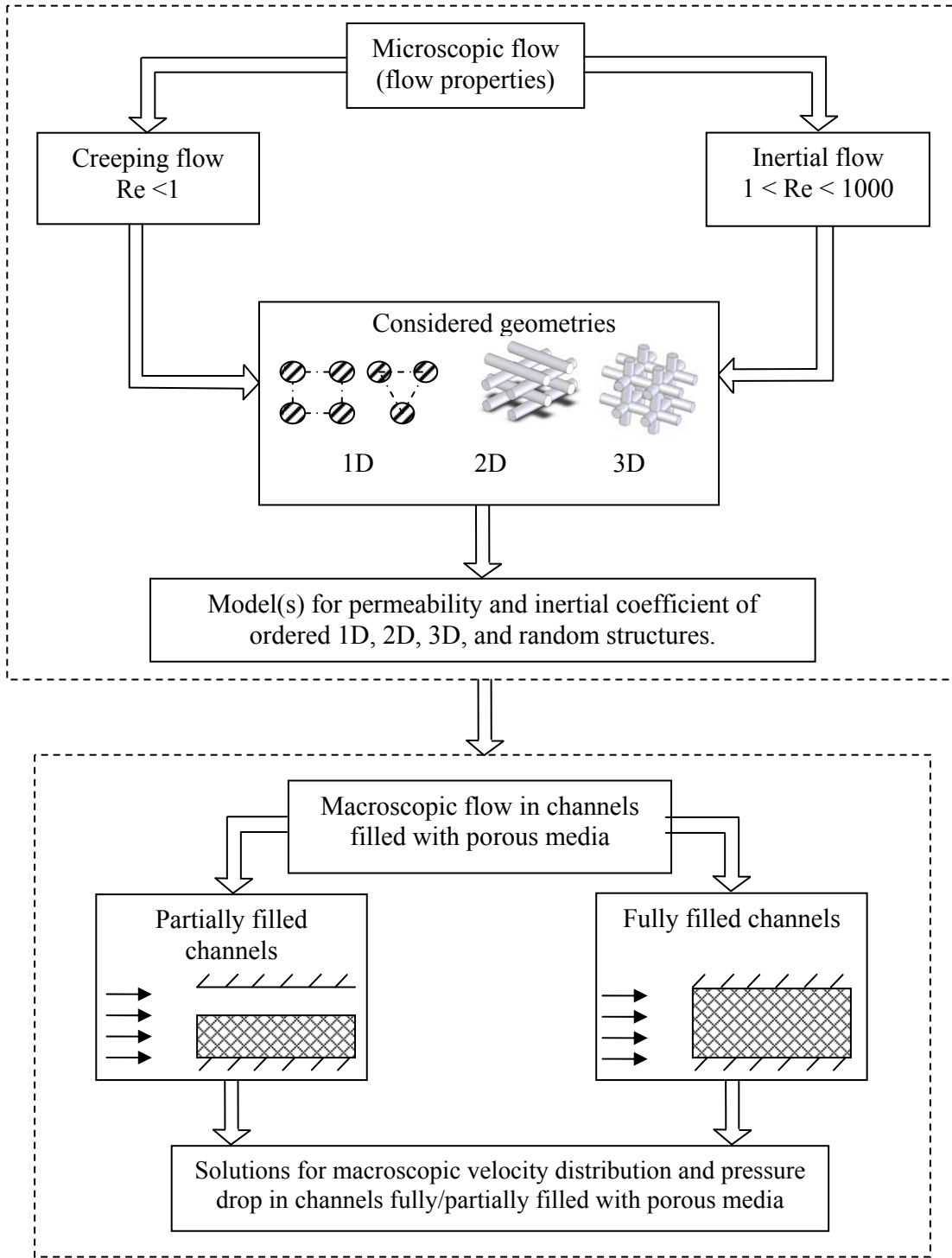
Figure 1: The present research project road map and deliverables.

Dedication

To my family and

my wife

Neda

Acknowledgements

Contents

List of Figures

Glossary

1D   One directional

2D   Two directional

3D   Three directional

A Pore cross-sectional area (normal to flow), m^2

d Fiber diameter, m

D_H Hydraulic diameter of the pore, m

f Fanning friction coefficient

GDL   Gas diffusion layer

F Formation factor

h Microchannel depth, m

I_p Polar moment of inertia of pore cross-section, m^4

I_p^* Dimensionless polar moment of inertia of pore cross-section,

$$I_p^* = I_p / A^2$$

K	Permeability, m^2
K^*	Non-dimensional permeability, $K^* = K/d^2$
k_0	Shape factor
$K_0(.)$	Modified second kind Bessel function
$K_1(.)$	Modified second kind Bessel function
k_k	Kozeny constant
K_{eq}	Equivalent permeability of fiber mixtures, m^2
L	Sample length, m
L_e	Effective length, m
ℓ	Unit cell length in Eq. (3), m
MEA	Membrane electrode assembly
MF	Metalfoam
P	Pressure, N/m^2

PEMFC   Polymer electrolyte membrane fuel cell

PTFE   Polytetrafluoro ethylene

Q Volumetric flow rate, m^3/s

Re   Reynolds number based on fiber diameter, $Re = \rho U_D d / \mu$

r Coordinate system, m

S Distance between adjacent fibers in square arrangement, m

S_x Distance between adjacent fibers in rectangular unit cell in x-direction, m

S_y Distance between adjacent fibers in rectangular unit cell in y-direction, m

SEM   Scanning electron micrograph

u Velocity component, m/s

u_b Velocity at the border of unit cell, m/s

u_{int} Interface velocity, m/s

U_D Volume-averaged superficial velocity, m/s

$U_{D\text{int}}$	Interface volume-averaged superficial velocity, m/s
u_p	Seepage velocity, m/s
v	Velocity component, m/s
w	Velocity component, m/s
W	Microchannel width, m
x	Coordinate system, m
y	Coordinate system, m
z	Coordinate system, m

Greek symbols

α	Constant in Eq. (34)
β	Inertial coefficient, m^{-1}
δ	Distance between surfaces of adjacent fibers, m
ε	Porosity
ε'	Microchannel cross-section aspect ratio

φ	Solid fraction, $\varphi = 1 - \varepsilon$
φ'	Non-dimensional parameter in Eq. (18), $\varphi' = \pi/4\varphi$
η	Dimensionless coordinate, $\eta = 2r/d$
Γ	Perimeter of flow passages, m
μ	Viscosity, $N.s/m^2$
μ_{eff}	Effective viscosity, $N.s/m^2$
μ'	Viscosity ratio, $\mu' = \mu_{eff}/\mu$
θ	Coordinate system
ρ	Density, Kg/m^3
σ	Constant in Eq. (19)
σ_1	Fluid electrical conductivity, S/m
σ_e	Effective electrical conductivity of a porous medium, S/m
τ	Tortuosity factor, $\tau = L_e/L$

1: INTRODUCTION

A volume, partly occupied by a permeable solid or semi-solid phase while the rest is void or occupied by one or several fluids, is called a porous medium [1]. The solid phase can either form a consolidate matrix, e.g., metalfoams, sponges, or be distributed in the fluid phase, e.g., particulate mixtures and granular materials. According to this definition, porous media involve in a diverse range of natural and industrial systems. Consequently, transport phenomena in porous media have been the focus of numerous studies since the 1850s, which indicates the importance of this topic. Most of these studies; however, dealt with low and medium porosity structures such as granular materials and packed beds of spherical particles.

When the solid particles have a cylindrical shape or the solid matrix is formed by high aspect ratio ligaments, the material is called a fibrous porous medium. Fibrous networks can form mechanically stable geometries with high porosity, the ratio of the void volume to the total volume up to 0.99 [2]. Moreover, these fibrous structures feature low-weight, high surface-to-volume ratio, high flow conductivity, high heat transfer coefficient, and high ability to mix the passing fluid [3]. Many natural and industrial materials involved in physiological systems [4], filtration [5], composite fabrication [6], compact heat exchangers [2, 3], paper production [7], and fuel cell technology [8, 9] have a fibrous structure, see Figure 2. As shown in Figure 3, based on the orientation of the fibers in space, fibrous structures can be categorized into three different groups:
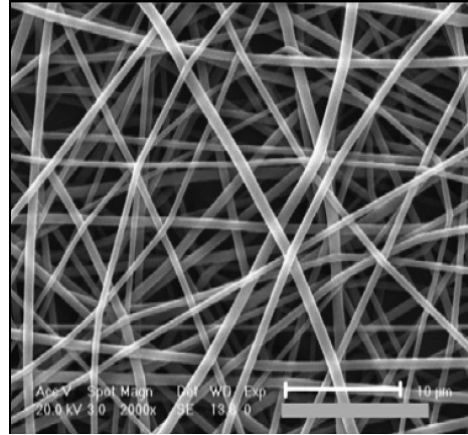
(a)
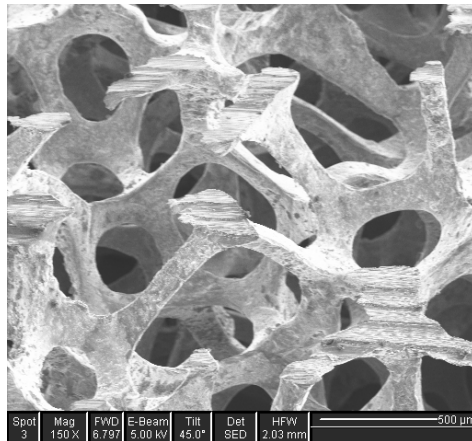
(b)
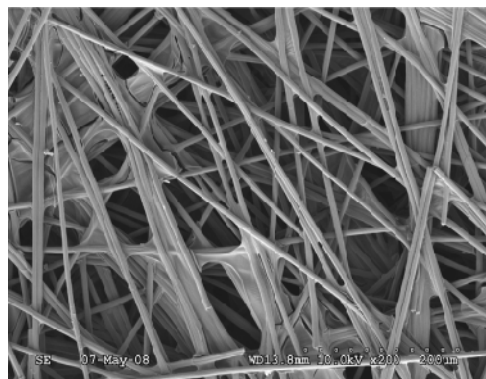
(c)

Figure 2: Scanning electron micrograph (SEM) of fibrous media in different applications a) electrospun fibrous scaffold for tissue engineering [10], b) aluminum foam, and c) Toray carbon paper (GDL).

- one-directional (1D) such as tube banks where the axes of fibers are parallel to each other;

- two-directional (2D), e.g., gas diffusion layer (GDL) of fuel cells, where the fibers axes locate on planes parallel to each other, with an arbitrary distribution and orientation on these planes;

- three-directional (3D) including metalfoams where their axes are randomly positioned and oriented in any given volume. With the exception of the 3D structures, the rest are anisotropic, i.e., the transport properties are direction dependent [11].

Investigation of the transport properties of these materials dates back to 1940s for evaluating properties of fibrous filters, and 1980s for composite fabrication. Development of new materials for novel applications such as fuel cell technology and compact heat exchangers has motivated researchers to investigate the transport properties of such media.

Proton exchange membrane fuel cells (PEMFCs) have shown the potential to be commercialized as green power sources in automotive, electronics, portables, and

(a)   (b)   (c)
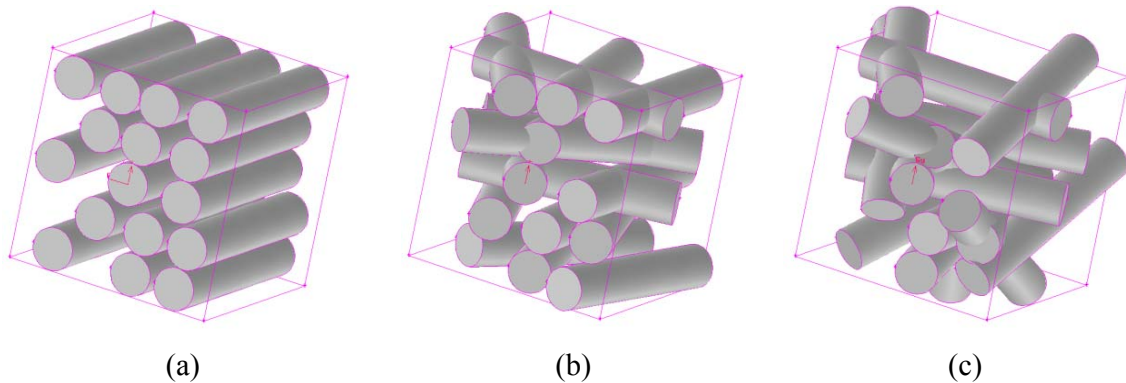
Figure 3: Structures with different fibers orientation; a) one direction (1D), b) two directional (2D), and c) three directional (3D).

stationary applications [12]. PEMFCs complete an electrochemical reaction to combine hydrogen and oxygen releasing heat, water, and electricity which can be used for a variety of application. The membrane electrode assembly (MEA) is the heart of a PEMFC. MEA is comprised of a membrane, loaded by catalyst layers on each side, which is sandwiched between two porous layers named gas diffusion layers (GDLs) [12]. In addition to mechanical support of the membrane, GDL allows transport of reactants, products, and electrons from the bipolar plate towards the catalyst layer and vice versa. Therefore, thermophysical properties of GDLs such as gas and water permeability, thermal, and electrical conductivity affect the PEMFC performance and reliability by affecting reactant access and heat and product removal from catalyst layers [13, 14].

An in-depth knowledge of the variation of these thermophysical properties with operating condition and microstructure is important in designing more reliable and efficient PEMFCs. The important parameters that have been used to describe carbon papers used as GDLs are: 1) porosity, ε (defined as the void to the total volume ratio), 2) fiber diameter, 3) the polytetrafluoro ethylene (PTFE) content of the material.

Improving the thermal performance of thermal management systems by designing more efficient heat exchangers currently receives an intense attention worldwide. In the past decade, as a result of the decrease in the production cost and the unique thermophysical properties, metalfoams have received a special attention [2]. Open cell metalfoams consist of small ligaments forming interconnected dodecahedral-like cells, see Figure 2. The shape and size of these open cells vary throughout the medium which make the structure random and in some cases anisotropic. The geometrical parameters

4

that are reported by manufacturers are: 1) porosity, ε, 2) fiber diameter, and 3) pore density, number of pores per unit length, typically expressed in pores per inch (PPI). These structures can be constructed from a wide variety of materials including metals (aluminum, nickel, copper, iron, and steel alloys), polymers, and carbon.

Determining the relationship between flow and the resulting pressure drop in fibrous porous materials is the first step in the analysis of transport phenomena in porous media. The complex geometry and randomness of porous materials makes developing exact pore-scale velocity distribution highly unlikely. From an engineering view point, however, it usually suffices to predict the macroscopic or volume averaged velocity rather than details of pore scale velocity distribution. As a result, the transport equations that are used in the design and analysis of fibrous systems are the volume averaged forms of the conventional equations.

In the creeping flow regime, according to the Darcy equation the relationship between the volume averaged velocity through porous media, U_D, and the pressure drop is linear [1]:

$$-\frac{dP}{dx} = \frac{\mu}{K} U_D \qquad (1)$$

where K is the permeability and μ is the fluid viscosity. The permeability can be interpreted as the flow conductance of a porous medium for a Newtonian fluid [15]. In higher Reynolds numbers, the relationship between the flow and pressure drop becomes nonlinear and a modified Darcy equation is used [1]:

$$-\frac{dP}{dx} = \frac{\mu}{K}U_D + \beta U_D^2 \qquad (2)$$

where β is the inertial coefficient. However, one needs to know K and β prior to using Eqs. (1) and (2). For a fibrous medium, the flow coefficients depend on the geometrical parameters of the solid matrix including porosity, fiber diameter, fiber shape, fiber distribution in space, fiber orientation relative to flow direction, and surface characteristics of the solid phase such as roughness and its behavior when in contact with the fluid, e.g., hydrophobicity.

The flow coefficients of a porous material are determined either experimentally or through pore scale analysis of the porous media (determining the detail velocity distribution and finding the resulting pressure drop) where both are time consuming and expensive tasks. As a result, having general model(s) or correlation(s) that can accurately estimate the flow properties of different fibrous matrices is a useful tool for engineers.

In applications where a porous material is confined by solid walls, e.g., microchannels filled with porous media (porous channels), or the flow inside the porous media is boundary driven, the boundary effects become significant. Micro-/mini-porous channels have potential applications in filtration [16], detection of particles, and tissue engineering. Moreover such structures have been used in biological and life sciences for analyzing biological materials such as proteins, DNA, cells, embryos, and chemical reagents [17, 18]. In addition, since micro-porous channels offer similar thermal properties such as high heat and mass transfer coefficients, high surface to volume ratio, and low thermal resistances to regular arrays of microchannels in the expense of lower pressure drops; these novel designs can be used in micro-cooling systems.

Another example of flow in confined porous media is channel-to-channel convection in PEMFCs. As a result of pressure difference between neighbor channels in the gas delivery channels of a PEMFC, reactants can pass through GDL in the in-plane direction, see Figure 4b. Channel-to-channel convection affects the reactant distribution in the fuel cell [13, 14].

Boundary driven flow through porous media can be seen in many cases such as channels partially filled porous media, hot spinning, and hot rolling. For example, gas flowing through GDL of fuel cells is driven in the in-plane direction by the flow in the gas delivery channels while is retarded by the porous matrix and the membrane that acts as a solid wall. Figure 4 shows a schematic of different layers in a fuel cell and the flow distribution inside a gas delivery channel and the underneath GDL.

The Darcy and modified Darcy equations are not capable of including the boundary effects on the flow through fibrous media. Therefore, the Brinkman equation [19] is used instead:

$$-\frac{dP}{dx} = \frac{\mu}{K}U_D + \beta U_D^2 + \mu_{eff}\frac{d^2U_D}{dy^2} \tag{3}$$

where μ_{eff} is called the effective viscosity. The Brinkman equation includes a diffusive term that allows applying various boundary conditions. This equation was originally developed for analysis of packed beds of particles [1]. As such, investigation of its validity for fibrous materials and micro-systems is critical.

(a)

Bipolar plate

GDLs

Gas
channels

Membrane

Gas
channels

(b)

Channel to
channel
convection

(c)

In-plane
flow inside
GDL
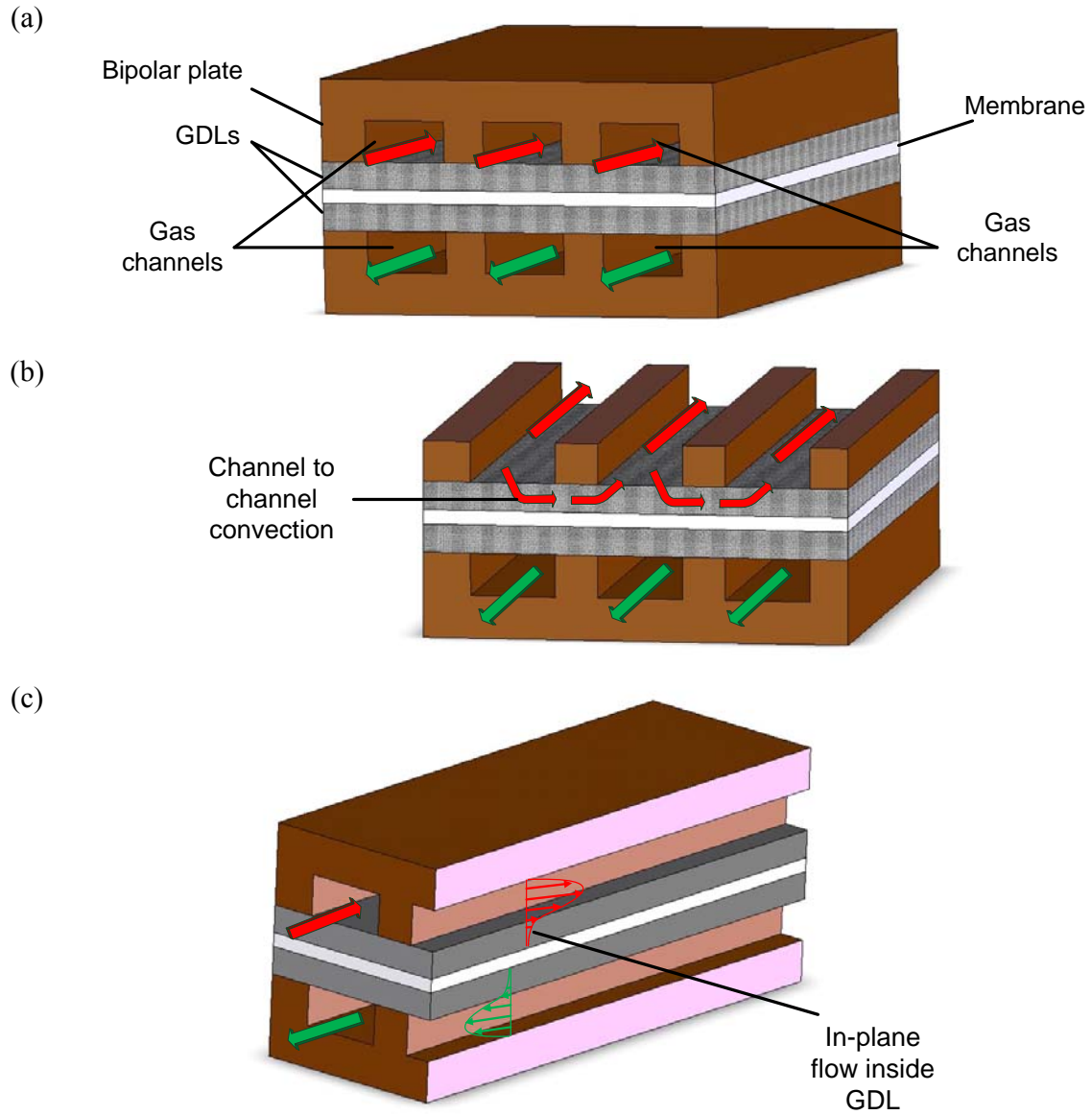
Figure 4: a) Schematic of different layers in a fuel cell, b) channel-to-channel convection, and c) in-plane flow inside GDL in the flow direction.

8

2: LITERATURE REVIEW

The literature of flow through fibrous porous media is very rich. Researchers have used different analytical, numerical, and experimental techniques to determine the flow properties of fibrous materials. In this section, only a selection of the relevant publications and techniques is critically reviewed and discussed.

2.1 Creeping flow through fibrous media

The creeping flow and the permeability have been studied either experimentally or theoretically using capillaric and pore network models, deterministic, blending, and swarm theory approaches.

2.1.1 Capillaric models and pore network modeling approach

The flow of a fluid in many porous media can be modeled to occur in a network of closed conduits. The models based on this approach are called "capillaric permeability models" [20]. The Carman-Kozeny [1] model was based on this approach. In the Carman-Kozeny model, the pressure drop across the porous medium was calculated using an equivalent conduit of uniform but non-circular cross-section. The hydraulic diameter of the equivalent conduit was defined as [1]:

$$D_H = \frac{4 \times \text{void volume of medium}}{\text{surface area of channels in medium}} \tag{4}$$

The seepage velocity, U_p, in the equivalent channels was obtained from a Hagen-Poiseuille type equation [1]:

$$U_p = \frac{\Delta P}{16 D_H^2 k_0 \mu L_e}$$

(5)

where L_e is the equivalent passage length of flow and k_0 is a shape factor. Kozeny assumed that the seepage velocity is related to the volume-averaged velocity through the Dupuit-Forchheimer assumption [21]:

$$U_p = \frac{U_D}{\varepsilon}$$

(6)

Carman [22] argued that the time taken for a fluid element to pass through a tortuous path of length L_e is greater than a straight path of length L, by an amount of $\tau = L_e / L$. Accordingly, he proposed that:

$$U_p = \frac{U_D}{\varepsilon} \tau$$

(7)

where τ is the tortuosity factor. The tortuosity depends on microstructure of porous media and is always greater than or equal to unity. Combining Eqs. (5) the permeability becomes [1]:

$$K = \frac{\varepsilon D_H^2}{16 k_0 \tau^2} = \frac{\varepsilon D_H^2}{16 k_k}$$

(8)

10

The term $k_k = k_0 \tau^2$ is called the Kozeny constant [1]. It should be noted that the Carman-Kozeny model is based on the assumption of conduit flow. However, at high porosity fibrous materials this assumption breaks down.

To improve the accuracy of capillaric approaches, the porous medium has been modeled by more complex networks of interconnected capillaries; this approach is also called pore network modeling [20]. The two main macroscopic properties used to define a porous medium are porosity and permeability that can be interpreted as the storage and the momentum transfer/pressure drop properties, respectively. Capillary network models exploit these in representing the medium as a network of pores and throats. The fluids are stored in the pores, while the volume occupied by throats is zero. The pressure drop is associated with the throats and pores do not apply any resistance against the flow [20]. A schematic of a two-dimensional network with each pore connected to four throats is depicted in Figure 5. For a reasonable accuracy, the considered network should resemble the structure of real porous media. Partly because of the lack of accurate information on the details of pore structure, such network models have not yet been successful to predict the single phase permeability.

The study of Markicevic et al. [23] for employing the pore network modeling to predict the single phase permeability of GDLs showed that adjusting the distribution of the throat sizes is not feasible. However, this approach has been successfully employed for predicting the pattern of water transport in hydrophobic structures such as GDLs [24-26].
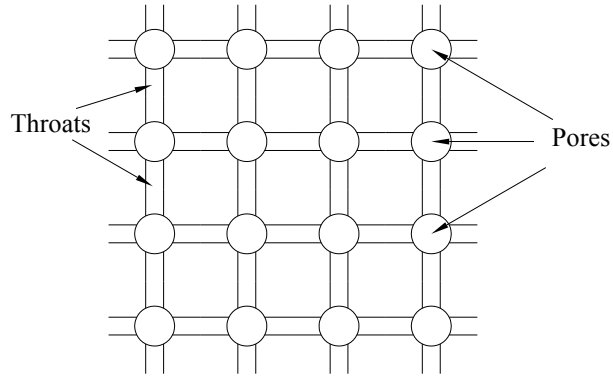
Figure 5: Schematic of capillary networks.

2.1.2 Deterministic approach

Models that use either an explicit or an approximate solution of the Navier-Stokes equations in the pore level are called "deterministic". The deterministic studies can be classified into unit cell approach, random microstructure approach, and swarm theory.

Unit cell approach: A common technique in analyzing fibrous structures is to model the medium with a unit cell which is assumed to be repeated throughout the medium. The unit cell (or basic cell) is the smallest volume which can represent the characteristics of the whole microstructure. Analytical studies of the pore-level flow, in general, solve the Stokes equation (a simplified form of the Navier–Stokes equation, which is valid for creeping flow) for a specified domain with periodic boundary conditions. The studied unit cells in the literature ranged from a single cylinder, ordered arrays of cylinders, to a specific number of cylinders in random arrangements. The relevant existing unit cell models in the literature are listed in Table 1.

Table 1: Summary of the relationships reported for permeability fibrous media.

Authors (Year)	Relationships[1] and Remarks
Happel (1959)	$$K = \frac{1}{32(1-\varepsilon)}\left[-\ln(1-\varepsilon) + \frac{(1-\varepsilon)^2 - 1}{(1-\varepsilon)^2 + 1}\right]d^2$$ • Based on limited boundary method • Developed for 1D fibers (normal flow) • Accurate only for high porosities
Happel (1959)	$$K = \left(2\varphi - \frac{\varphi^2}{2} - \ln\varphi - 1.5\right)\frac{d^2}{16\,\varphi}$$ • Based on limited boundary method • Developed for 1D fibers (parallel flow) • Accurate only for high porosities, $\varepsilon > 0.7$
Kwabara (1959)	$$K = \frac{1}{32(1-\varepsilon)}\left[-\ln(1-\varepsilon) - \frac{3}{2} + 2(1-\varepsilon)\right]d^2$$ • Based on limited boundary method • Developed for 1D fibers • Accurate only for medium to high porosities (normal flow)
Hasimoto (1959)	$$K = \frac{1}{32(1-\varepsilon)}\left[-\ln(1-\varepsilon) - 1.476\right]d^2$$ • Based on Fourier series method • Developed for square arrays of cylinders (normal flow) • Accurate for high porosities
Sangani and Acrivos (1982)	$$K = \frac{1}{32(1-\varepsilon)}\left[\begin{array}{l}-\ln(1-\varepsilon) - 1.476 + 2(1-\varepsilon) \\ -1.774(1-\varepsilon)^2 + 4.076(1-\varepsilon)^3\end{array}\right]d^2$$ • Based on an asymptotic solution • Developed for square arrays of cylinders (normal flow) • Accurate for $\varepsilon > 0.7$
Sangani and Acrivos (1982)	$$K = \frac{1}{32(1-\varepsilon)}\left[\begin{array}{l}-\ln(1-\varepsilon) - 1.490 + 2(1-\varepsilon) \\ -0.5(1-\varepsilon)^2 + 4.076(1-\varepsilon)^3\end{array}\right]d^2$$ • Based on an asymptotic solution • Developed for square arrays of cylinders (normal flow) • Accurate for $\varepsilon > 0.7$

Authors (Year)	Relationships[1] and Remarks
Drummond and Tahir (1984) a	$$K = \frac{d^2}{32(1-\varepsilon)}\left[\frac{-\ln(1-\varepsilon)-1.473+}{\dfrac{2(1-\varepsilon)-0.796\,(1-\varepsilon)^2}{1+0.489\,(1-\varepsilon)-1.605(1-\varepsilon)^2}}\right]$$ • Based on distributed singularities approach • Developed for square arrays of cylinders (normal flow) • Accurate for $\varepsilon > 0.7$
Drummond and Tahir (1984) b	$$K = \left(\frac{-\ln\varphi-1.47633597+}{\dfrac{2\varphi-0.79589781\,\varphi^2}{1+0.48919241\,\varphi-1.60486942\,\varphi^2}}\right)\frac{d^2}{16\,\varphi}$$ • Based on distributed singularities approach • Developed for square arrays of cylinders (parallel flow) • Accurate over the entire range
Van der Westhuizen and Du Plessis (1996)	$$K = \frac{\pi\,\varepsilon\left(1-\sqrt{1-\varepsilon}\right)^2}{96(1-\varepsilon)^{1.5}}d^2$$ • Based on solution of the phase average Navier-Stokes equation • Random unidirectional fiber beds (normal flow)
Sahraoui and Kaviany (1994)	$$K = 0.0606\,\frac{\pi\,\varepsilon^{5.1}}{4(1-\varepsilon)}d^2$$ • Based on curve fit of numerical results (normal flow) • Accurate for $0.4 < \varepsilon < 0.8$
Gebart (1992)	$$K = \frac{4}{9\sqrt{2}\pi}\left(\sqrt{\frac{\pi/4}{1-\varepsilon}}-1\right)^{5/2}d^2$$ • Based on lubrication theory • Developed for square arrays of fibers (normal flow) • Accurate for $\varepsilon < 0.7$
Jackson and James (1986)	$$K = \frac{3}{80}\left[\ln(1-\varepsilon)-0.931\right]d^2$$ • Based on blending technique • For hydrogels • Developed for 3D structures (normal flow) • Accurate only for $\varepsilon > 0.85$

Authors (Year)	Relationships[1] and Remarks
Tomadakis and Sotirchos (1993)	$$K = \frac{\varepsilon}{8(\ln \varepsilon)^2}\left(\frac{(\varepsilon - \varepsilon_p)^{(\alpha+2)}}{(1-\varepsilon_p)^{\alpha}[(\alpha+1)\varepsilon - \varepsilon_p]^2}\right)d^2 ,$$ $\varepsilon_p = 0$, $\alpha = 0$, 1D structures (parallel) $\varepsilon_p = 0.33$, $\alpha = 0.707$, 1D structures (normal) $\varepsilon_p = 0.11$, $\alpha = 0.521$, 2D structures (parallel) $\varepsilon_p = 0.11$, $\alpha = 0.785$, 2D structures (normal) $\varepsilon_p = 0.037$, $\alpha = 0.661$, 3D structures • Based on the analogy between electrical and flow conductions • Developed for over lapping fibers • Developed for 1D, 2D, and 3D structures • Accurate for $\varepsilon < 0.85$
Van Doormaal and Pharoah (2009)	$$K = 0.07\frac{\varepsilon^{4.3}}{1-\varepsilon}d^2 \text{ normal flow}$$ $$K = 0.065\frac{\varepsilon^{3.6}}{1-\varepsilon}d^2 \text{ parallel flow}$$ • Based on curve fit of numerical results • Developed for 2D gas diffusion layers • Accurate only for $0.6 < \varepsilon < 0.8$
Spielman and Goren (1968)	$$\frac{1}{2} + \frac{2\sqrt{K}}{d}K_1\left(\frac{d}{2\sqrt{K}}\right) = \frac{K_0\left(\frac{d}{2\sqrt{K}}\right)}{4(1-\varepsilon)}$$ • Based on swarm method • Developed for 2D filters (normal flow) • Implicit and not easy-to use • K_0 and K_1 are the modified second kind Bessel functions
Spielman and Goren (1968)	$$\frac{1}{3} + \frac{5\sqrt{K}}{3d}K_1\left(\frac{d}{2\sqrt{K}}\right) = \frac{K_0\left(\frac{d}{2\sqrt{K}}\right)}{4(1-\varepsilon)}$$ • Based on swarm method • Developed for 3D filters (normal flow) • Implicit and not easy-to use

Authors (Year)	Relationships[1] and Remarks
Davies (1952)	$$K = \frac{d^2}{4\,(1-\varepsilon)^{3/2}\left[1 + 56(1-\varepsilon)^3\right]}$$ • Based on curve fit on experimental data • Developed for 2D filters (normal flow) • Accurate for $\varepsilon > 0.7$
Dukhan (2006)	$K = a_1 \exp\left[b_1\,\varepsilon\right]$ PPI = 10, $a_1 = 1 \times 10^{-11}$, $b_1 = 0.1$ PPI = 20, $a_1 = 9 \times 10^{-12}$, $b_1 = 0.1$ PPI = 40, $a_1 = 8 \times 10^{-15}$, $b_1 = 0.16$ • Proposed for metalfoams • Based on curve fit

[1] d : fiber diameter, ε : porosity, φ : solid volume fraction = 1 - ε

Kuwabara [27] and Happel [28] studied flow transverse and parallel to a cylinder enclosed in a circular unit cell. In this approach, called the limited boundary method, it was assumed that the interaction of the cylinders with the flow around them was limited to the enclosed region.

Hasimoto [29] and Sparrow and Loeffler [30] used series solutions for determining the permeability of ordered arrangement of cylinders to normal and parallel flow, respectively. Later, Sangani and Acrivos [31], performed analytical and numerical studies on viscous permeability of square and staggered arrays of cylinders for the entire range of porosity, when their axes were perpendicular to the flow direction. Their analytical models were based on Fourier series and lubrication theory for the high and low limits of porosity, respectively [31]. Drummond and Tahir [32] solved Stokes equations for normal and parallel flow towards different ordered structures. They used a distributed singularities method to find the flow-field in square, triangular, hexagonal and rectangular arrays. They [32] compared their results with numerical values of Sangani

and Acrivos [31] for normal flow and Happel [28] for the parallel case. The model of Drummond and Tahir [32] for normal permeability was very close to the analytical model of Sangani and Acrivos [31]; thus, it is only accurate for highly porous materials where $\varepsilon > 0.7$.

Keller [33] and Gebart [34] assumed that the permeability of ordered fibrous structures is controlled by the narrow slots formed between the fibers; they applied the lubrication theory to determine the flow resistance through the gap. It should be noted that the lubrication theory is usually valid in the limit of close-packed fibers, $\varepsilon < 0.65$. The abovementioned models are compared with experimental data in Section 2.4.

The numerical studies on the flow through fibrous media are summarized in Table 2. Several researchers have numerically simulated the creeping flow through ordered cylinders [31, 35-38]. In general, numerical simulations cover a wider range of porosity and fiber distribution in applying the unit cell approach for 1D, 2D, and 3D structures. Sangani and Yao [39] extended the studies of Sangani and Acrivos [31] for ordered structures to 1D cylinders in random distribution. Higdon and Ford [40] used a spectral boundary element formulation to calculate the hydraulic permeability of ordered, monomodal, three dimensional fibrous media. They considered simple cubic (SC), body-centered cubic (BCC), and face-centered cubic (FCC) arrangements of fibers in a unit cell. Applying a singularity method, Clague and Philips [41] computed the permeability of ordered periodic arrays of cylinders and of disordered cubic (periodic) cells of cylindrical fibers. Clague et al. [42] employed a lattice-Boltzmann technique to study similar geometries and extended their studies to include bounded structures. Sobera and Kleijn [37] studied the permeability of 1D and 2D ordered and random fibrous media

both analytically and numerically. Their analytical model was a modification of the scale analysis proposed by Clauge et al. [42]. Boomsma et al. [43] used a finite volume method to solve the flow inside dodecahedral and tetrahedral unit cells to investigate flow properties of metalfoams. Palassini and Remuzzi [44] employed a finite element method to solve the Stokes equation for a tetrahedral array of fibers to predict the flow properties of glomerular basement membrane.

Random microstructure approach: As a result of the recent significant growth of computational power, several researchers have tried to perform simulations on microstructures formed by a higher number of cylindrical fibers. These researchers have generated random microstructures that resemble the actual fibrous materials for different applications.

Clauge and Philips [41] were among the pioneers in employing random microstructure approach. They used a numerical version of slender body theory to determine permeability of monodisperse and polydisperse random fibrous microstructures. Stylianopolous et al. [45], Clauge et al. [42], and Tahir and Tafreshi [46], used finite element, lattice Boltzmann, and finite volume methods, respectively to solve creeping flow inside 3D random fibrous structures. Koponen et al. [47] and Zobel et al. [48] performed numerical simulations for 2D structures using lattice Boltzmann and finite elements methods, respectively.

Hao and Cheng [49] solved creeping flow through a mesh of 2D random fibers over a wide range of porosity $\varepsilon > 0.6$ to model the GDL of PEM fuel cells. They used a Lattice Boltzmann method in their study. In a similar study Nabovati et al. [50]

performed lattice Boltzmann simulations for 3D random structures in the porosity range

of $\varepsilon > 0.15$. They also reported a correlation for calculating permeability. Lattice

Boltzmann simulations of gas flow through several random fibrous structures were

carried out by Vandoormaal and Pharoah [51] over the porosity range of $0.6 < \varepsilon < 0.8$.

They reported numerical results for different fiber orientations which were an order of

magnitude different in a constant porosity.

Table 2: Summary of the selected numerical studies for fibrous media.

Authors	Structure	Flow condition and Remarks[1]
Sangani and Yao (1988)	1D ordered and random arrays of monodisperse cylinders, $0.3 < \varepsilon < 0.9$	• Normal and parallel flow • Re < 1 • Multipole expansion method
Sahraoui and Kaviany (1992)	1D ordered and deformed cylinders, $0.4 < \varepsilon < 0.8$	• Normal flow • Re < 200 • Good agreement with experimental data • Finite volume method
Edwards et al. (1990)	1D ordered monodisperse and polydisperse cylinders, $0.4 < \varepsilon < 0.8$	• Normal flow • Re < 180 • Not in good agreement with Ergun equation • Finite element method
Higdon and Ford (1996)	1D and 3D ordered unit cells, the entire range of porosity	• Normal flow • Re < 180 • Boundary element method
Ghaddar (1995)	1D ordered and random, $0.4 < \varepsilon < 0.8$	• Normal flow • Re < 200 • In good agreement with experimental data • Parallel finite element method
Johson and Deen (1996)	2D unit cell, $\varepsilon = 0.32$	• Normal flow • Re < 1 • Finite element method
Clauge and Philips (1997)	3D random monodisperse and polydisperse structures	• Normal flow • Re < 1 • Slender body theory

Authors	Structure	Flow condition and Remarks[1]
Koponen et al. (1998)	2D random mats, $0.4 < \varepsilon < 0.95$	- Normal flow - Re < 1 - Lattice Boltzmann
Martin et al. (1998)	1D ordered monodisperse cylinders, $0.8 < \varepsilon < 0.99$	- Normal flow 3 < Re < 180 - Not in good agreement with Ergun equation - Finite volume method
Koch and Ladd (1997)	1D ordered and random structures, $\varepsilon > 0.45$	- Normal flow - Re < 180 - Lattice Boltzmann method
Clauge et al. (2000)	3D random structures	- Normal flow - Re < 1 - Correlation is proposed - Lattice Boltzmann method
Papathanasiou et al. (2001)	1D ordered monodisperse and polydisperse arrays, $0.3 < \varepsilon < 0.6$	- Normal flow - Re < 180 - Not in good agreement with Ergun equation - A correlation is proposed for inertial coefficient - Finite element method
Sobera and Kleijn (2006)	1D and 2D ordered and disordered unit cells, $0.1 < \varepsilon < 0.8$	- Normal flow - Re < 1 - A scale analysis method was also proposed - Finite volume method
Rong et al. (2007)	3D random, $0.42 < \varepsilon < 0.72$	- Normal flow - Re < 15 - Inertial effects were significant - Lattice Boltzmann method
Hellstrom and Lundstrom (2006)	1D ordered arrays of cylinders , $0.3 < \varepsilon < 0.6$	- Normal flow - Re < 1200 - Not in good agreement with Ergun equation - Finite volume method
Mattern and Deen (2008)	1D bimodal charged fibers, $\varepsilon > 0.8$	- Normal flow - Re < 1 - Finite volume method
Jagathan et al. (2008)	2D random structures, $0.85 < \varepsilon < 0.94$	- Normal flow - Re < 1 - Digital volume imaging and finite volume method

Authors	Structure	Flow condition and Remarks[1]
Stylianopolous et al. (2008)	3D random structures, $\varepsilon > 0.55$	• Normal flow • Re < 1 • In agreement with experimental results • Finite element method
Nabovati et al. (2008)	3D random structures, $0.08 < \varepsilon < 0.95$	• Normal flow • Re < 1 • A correlation was proposed • Lattice Boltzmann method
Tahir and Vahedi Tafreshi (2009)	2D and 3D random structure, $\varepsilon > 0.8$	• Normal flow • Re < 1 • Fiber orientation was significant • Finite volume method
Hao and Cheng (2009)	2D gas diffusion layers, $\varepsilon > 0.4$	• Parallel and normal flows • Re < 1 • Flow tortuosity is also reported • Lattice Boltzmann method
Vandoormaal and Pharoah (2008)	2D gas diffusion layers, $0.6 < \varepsilon < 0.8$	• Parallel and normal flows • Re < 1 • Correlations are also reported • Lattice Boltzmann method

[1] Reynolds number based on fiber diameter, $\text{Re} = \dfrac{\rho U_D d}{\mu}$

Swarm Theory: Another approach in modeling creeping flow through a random packing of spheres or cylinders is to consider a reference geometry like a sphere or a cylinder surrounded by a shell representing the associated pore space. The shell is then embedded in a porous medium of permeability K, see Figure 6. The Stokes and the Brinkman equations are solved inside the shell and the porous medium, respectively. The permeability is determined in a way that the velocity distribution from both equations matches on the shell boundary. This approach, called the Swarm theory, was originally used by Neale and Nader [52] for packed beds of spheres. The same idea was followed by

Spielman and Goran [5] for 2D and 3D fibrous structures. They proposed two implicit models for calculating the permeability of such structures which are presented in Table 1.

2.1.3 Blending rules (Mixing rules)

An approximate method that has been used by researchers to estimate the permeability of real fibrous media is the blending technique. In this approach, the complex porous microstructure is modeled as a mixture/combination of fibrous structures with known permeability [53]. As such, it is expected that the equivalent permeability, K_{eq}, to be related to the permeability of each component; the concept of blending technique for 2D fibrous mats is shown in Figure 7. It should be noted that there is no concrete rule for estimating the mixtures' permeability. This approach was originally proposed by Happel [28] for predicting the permeability of 3D random materials which was not successful. In more recent studies, blending techniques have been successfully employed to estimate the permeability of fibrous mixtures such as hydrogels [54], fibers with different sizes [41], and fibers with different charges [55, 56].
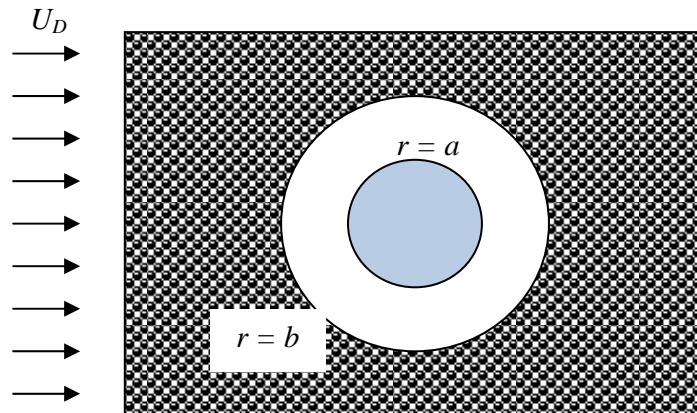
Figure 6: Schematic of the swarm theory approach.

22
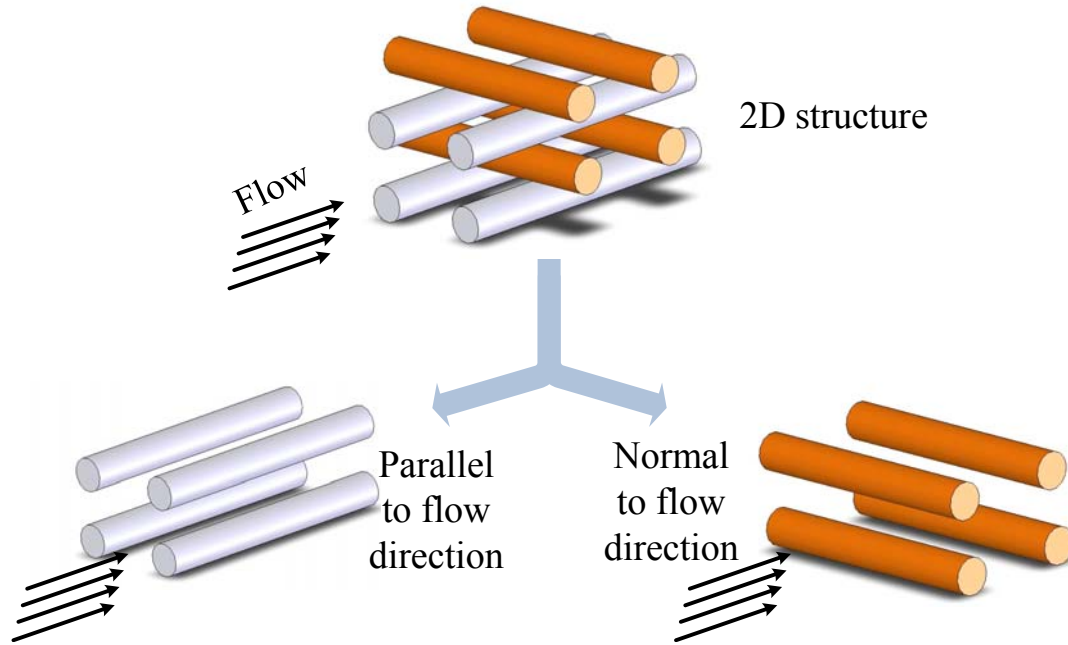
Figure 7: The blending technique concept for 2D structures.

2.1.4 Analogy of hydraulic permeability with other diffusive properties

Several researchers have tried to relate the permeability to different measurable transport properties of the porous medium. One of the properties that has been used for calculating the permeability is the electrical formation factor, *F*, which is defined as [20]:

$$F = \frac{\sigma_1}{\sigma_e} \tag{9}$$

where σ_e is the effective electrical conductivity of a porous medium of an insulating solid containing a conducting fluid of conductivity σ_1.

Johnson et al. [57] proposed the following approximate relation involving the electrical conductivity:

$$K \approx \frac{\Lambda^2}{8F} \qquad (10)$$

where:

$$\frac{\Lambda}{2} = \frac{\int |E(r)|^2 dV}{\int |E(r)|^2 ds} \qquad (11)$$

$E(r)$ is the local electric-field, dV and dS denote integrations over volume and the pore-solid surface, respectively. The parameter Λ is a weighted pore volume-to-surface ratio that provides a measure of the dynamically connected parts of the pore region. Tomadakis and Sotirchos [58] used a random-walk simulation method to calculate the formation factor for randomly distributed overlapping fibers. Using their simulations results and combining Eqs. (10) and (11), Tomadakis and Robertson [11] reported a model for calculating permeability of 1D, 2D, and 3D fibrous structures, see Table 1.

2.1.5   Experimental studies

As a result of the diverse applications of fibrous materials, numerous experimental studies have been conducted for determination of the permeability of fibrous media; see for example [22, 36, 48, 59-71]. Good reviews of experimental works are available in Jackson and James [54], Astrom et al. [15], and Tomadakis and Robertson [11]. Although our motivation for the present study is mostly coming from sustainable energy applications such as fuel cell technology and use of metalfoams as media for heat transfer, a selection of experimental studies on various fibrous materials is summarized in Table 3. The experimental studies are selected such that structure inhomogeneity, channeling, fiber mobility, deflection, compression, fiber bending, fiber

surface slip, non-viscous flow, inertial effects, tube wall friction, capillary effects, surface tension, gas compressibility, fiber shape/size distribution, and fiber aspect ratio effects were not involved in the measurements.

There are few experimental studies available in the literature that reported the permeability of GDLs in creeping flow regime. Williams et al. [72], Ihonen et al. [73], and Mueller et al. [74] measured the through-plane permeability of several GDLs. Most of their measurements were affected by existence of the micro porous layer. Prasanna et al. [75] and Mathias et al. [76] reported the through-plane permeability of several bare GDLs with various PTFE loadings.

Ihonen et al. [73] showed that a reverse relationship exists between the in-plane permeability and compression. Recently, Feser et al. [8] studied the effects of compression and reported in-plane gas permeability as a function of porosity for a carbon cloth, a non-woven carbon fiber GDL, and a carbon paper. In a similar work, Gostick et al. [9] measured permeability of several commercial GDLs under various compressive loads and reported the in-plane permeability as a function of porosity. They also reported the through plane permeability of these GDLs. More details of the experimental studies can be found in Ref. [77].

2.2   Inertial flow regime (moderate Reynolds numbers)

Including the inertial effects in the flow analysis adds to the complexity of the problem. As such, the moderate Reynolds number flows through fibrous structures are mostly studied either numerically or experimentally rather than analytically in the literature.

25

2.2.1 Theoretical studies

Khan et al. [78] employed an integral technique solution to determine pressure drop in tube banks with regular cylinder arrays, analytically. The velocity profiles were calculated from a combination of the potential flow and the boundary layer theories. Their model was developed for high Reynolds number flows, Re > 100, and could capture trends of the experimental data reported by others qualitatively.

Effects of Reynolds number on the pressure drop through unidirectional mono-disperse and bimodal fibers were investigated numerically by Nagelhout et al. [79], Martin et al. [80], Lee and Yang [81], Koch and Lodd [82], Edwards et al. [83], Ghaddar [84], and Papathanasiou et al. [85]. Their results, in general, confirmed the existence of a parabolic relationship between pressure drop and flow rate in the considered geometries. However, comparison of these numerical results with conventional models in the literature such as the Ergun equation was not successful [85].

The studies of moderate Reynolds number flows through 2D and 3D structures are not frequent. Recently, Rong et al. [86] used Lattice Boltzmann method to investigate flow in three dimensional random fiber network with porosities in the range of $0.48 < \varepsilon < 0.72$. Their results were in agreement with Forchheimer equation which is in line with the observations of [86]. Boomsma et al. [43] have also studied flow in high porosity 3D fibrous structures to predict the flow properties of open cell aluminum foams.

Table 3: Summary of the selected experimental studies for flow properties of fibrous media.

Authors	Material Fiber category (flow direction)	Test fluid Re_{max}	Fiber diameter (*mm*)
Carman (1938)	stainless steel wire, $0.681 < \varepsilon < 0.765$ Random 3D (normal)	Glycerol 0.5	0.328
Wiggins et al. (1939)	Glass rods, copper wire, glass wool, and fiber glass, $0.685 < \varepsilon < 0.93$ Random 3D (normal)	Water 8	0.007-0.408
Sullivan (1942)	Drill rod, copper wire, goat wool, Chinese hair, and blond hair Ordered and random 1D (parallel)	Air N.A.	0.008-7.2
Bergelin et al. (1950)	Various arrangements of tubes, $0.42 < \varepsilon < 0.65$ Ordered 1D (normal)	Silicon oil 10	9.52, 19.04
Davies (1952)	Glass wool, kapok, rayon, $\varepsilon > 0.8$ Random 2D (normal and parallel)	Air N.A.	N.A.
Kirsch and Fuchs (1967)	Various arrangements of kapron tubes, $\varepsilon > 0.7$ Ordered 1D (normal)	Water 0.005	0.15, 0.225, 0.4
Kostornov and Schevchuck (1977)	Kapron fibers 2D random (normal)	Water, alcohol 10	N.A.
Jackson and James (1982)	Hyaluronic acid polymer, $\varepsilon > 0.99$ 3D random (normal)	Water 1×10^{-11}	1×10^{-6}
Gutowski et al. (1987)	Fiber mats $0.2 < \varepsilon < 0.5$ 1D random (normal)	Silicon oil N.A..	0.008
Skartsis et al. (1992)	Random carbon fibers and ordered aluminum rods, $0.4 < \varepsilon < 0.7$ 1D ordered and random (normal and parallel)	Water, Silicon oil N.A..	1.19-1.59
Chmielewski and Jayaraman (1992)	Acrylic rods in ordered arrangement, $\varepsilon = 0.7$ 1D ordered (normal)	Polybutene H25 and kerosene 0.3	4.76
Khomami and Moreno (1997)	Acrylic rods, $0.45 < \varepsilon < 0.85$ 1D ordered (normal)	Silicon oil N.A.	7.1, 14.2
Rahli et al. (1997)	Bronze and copper rods, $0.4 < \varepsilon < 0.9$ 3D random (normal)	Water N.A.	0.15

Authors	Material Fiber category (flow direction)	Test fluid Re_{max}	Fiber diameter (*mm*)
Shih and Lee (1998)	Random fiber mat U750, $0.4 < \varepsilon < 0.7$ 2D random (parallel)	Diphenyl-octyl-pthalate N.A.	0.02
Zhong et al. (2006)	Acrylic rods, $0.9 < \varepsilon < 0.975$ 1D ordered (normal)	Glycerol-water mixture 0.17	3.18
Zobel et al. (2007)	Polypropylene fibers, $0.7 < \varepsilon < 0.9$ 2D random (normal)	Air N.A.	0.015
Williams et al. (2004)	Gas diffusion layer 2D random (normal)	Air N.A.	0.007-0.001
Ihonen et al. (2004)	Gas diffusion layer 2D random (normal and parallel)	Air N.A.	0.009
Prasanna et al. (2004)	Gas Diffusion layer, $\varepsilon < 0.78$ 2D random (normal)	Air N.A.	0.009
Feser et al. (2006)	Gas Diffusion layer, $0.7 < \varepsilon < 0.78$ 2D random (parallel)	Air N.A.	0.009
Gostick et al. (2006)	Gas Diffusion layer, $0.65 < \varepsilon < 0.85$ 2D random (normal and parallel)	Air N.A.	0.007-0.001
Hunt and Tien (1988)	Chrome, aluminum, and nickel foams, $0.94 < \varepsilon < 0.97$ 3D random (normal)	Water $Re_K = 100$ [1]	N.A.
Calmidi and Mahajan (2000)	Aluminum foam, $0.9 < \varepsilon < 0.97$ 3D random (normal)	Air $Re_K = 135$	0.25-0.5
Boomsma and Poulikakos (2002)	Compressed aluminum foam, $0.61 < \varepsilon < 0.93$ 3D random (normal)	Air $Re_K = 27$	N.A.
Hwang et al. (2002)	Aluminum foam, $0.7 < \varepsilon < 0.9$ 3D random (normal)	Air $Re_p = 7800$ [2]	N.A.
Bhattacharya et al. (2002)	Aluminum foam, $0.9 < \varepsilon < 0.98$ 3D random (normal)	Air N.A.	0.2-0.55
Boomsma et al. (2003)	Comressed aluminum foam, $0.61 < \varepsilon < 0.93$ 3D random (normal)	Air $Re_K = 140$	N.A.
Kim et al. (2003)	Aluminum foam, $\varepsilon = 0.92$ 3D random (normal)	Air $Re_p = 2900$	0.2-0.4

Authors	Material Fiber category (flow direction)	Test fluid Re_{max}	Fiber diameter (*mm*)
Khayargoli et al. (2004)	Nickel and nickel-chromium, $0.83 < \varepsilon < 0.9$ 3D random (normal)	Air N.A.	N.A.
Tadrist et al. (2004)	Comressed aluminum foam, $0.88 < \varepsilon < 0.89$ 3D random (normal)	Air N.A.	0.69-1
Dukhan (2006)	Comressed aluminum foam, $0.68 < \varepsilon < 0.92$ 3D random (normal)	Air $\text{Re}_p = 1000$	0.25-0.5
Bonnet et al. (2008)	Copper, nickel, and nickel-chromium 3D random (normal)	Air, water $\text{Re}_p = 2000$	N.A.

[1] Re_K: Reynolds number based on $\sqrt{K}$, $\text{Re} = \dfrac{\rho U_D \sqrt{K}}{\mu}$

[2] Re_p: Reynolds number based on pore diameter, $\text{Re} = \dfrac{\rho U_D d_p}{\mu}$

2.2.2 Experimental studies (moderate Reynolds numbers)

Most of the high Reynolds number (Re > 1000) experimental studies on porous media have been done to investigate the flow properties of heat exchangers. As a result, accurate correlations have been presented for the turbulent flow properties of 1D tube banks; see for example [87]. Recently, metalfoams have received an especial attention because of their thermophyscial properties that make them good candidates for compact heat exchangers. In metalfoams, the flow Reynolds numbers based on fiber diameter typically range from 10 to 500. In this range, the pressure drop is related to volume-averaged velocity through the Forchheimer equation, Eq. (2) and both terms have the same order of magnitude in the overall pressure drop.

Bergelin et al. [88] measured the pressure drop across several tube bank arrays for Re < 1000. Kirsch and Fuchs [63] studied similar structures for Re < 10 and found out

that the onset of transition from the Darcy equation to the Forchheimer equation is Re ≈ 5-8. Few other studies have been conducted for moderate Reynolds flow through fibrous materials which are listed in.

Hunt and Tien [89] were among the pioneers to investigate thermophysical properties of metalfoams in 1980s. Since then, several experimental works have reported the permeability and the inertial coefficient of various metalfoams [2, 90-100]; these studies are summarized in Table 3. It should be noted that the minimum Reynolds number in the listed studies generally has been higher than 1; this can affect the accuracy of the reported values for the permeability.

2.3   Flow through channels partially-/fully-filled with porous media

Although the fully-developed and developing flows in channels of various cross-sections filled with porous media have been extensively studied in the literature, see for example [101-103]; however, such studies for micron size channels are not numerous. Hooman and his coworkers [104, 105] have investigated rarefied gas flows in microchannels filled with porous media. But, their theoretical analyses were not verified by experimental data. Few experimental studies have been conducted to study the flow through mini/microchannels filled with micro pin fins. Kosar et al. [106] studied laminar flow across four different arrays of micro pin fins embedded inside microchannels with 100 μm depth. The pin fin diameters in their study were 50 and 100 μm. They compared their results for Reynolds numbers in the range of 5-128 with existing correlations for relatively high Reynolds number flows through macro-scale tube banks and observed a significant deviation. Kosar et al. [106] related this deviation to the difference(s) between

flow in micron and regular-size systems. Vanapalli et al. [107] measured the pressure

drop in microchannels of 250 μm depth containing various pillar arrays in the Reynolds

number range of 50-500. On the contrary, their results for circular pillars were in good

agreement with conventional relationships. Yeom et al. [108] reported low Reynolds

number flow pressure drops through micro-porous channels with various fibers in square

arrangements. The channels were $200 \mu m$ deep and the diameters of the microposts

ranged from 200 μm to less than $10 \mu m$. Similar to [107], Yeom et al. [108] did not

include wall effects into their analysis. Therefore, their results for high permeability

arrays deviated from the values predicted by conventional theories.

Fluid flow in channels or systems partially filled with porous media has a wide

range of engineering applications such as electronic cooling, transpiration cooling, drying

processes, thermal insulation, oil extraction, and geothermal engineering. The two main

challenges involved in modeling this problem are: i) estimating the flow properties of

porous media and ii) finding accurate boundary conditions for the interface region.

Beaver and Joseph [109] were among the pioneers that investigated the interface

boundary condition. They noticed a slip in the experimental values of velocity at the

interface region. Vafai and Kim [110] developed an analytical solution for fluid flow at

the interface between a saturated porous medium and a fluid layer. Kuznetsov [111]

extended the analysis of [110] to higher Reynolds number flows and included the inertial

effects in his analytical solution. Velocity distribution for channels partially filled with

cylinders aligned with the flow direction was reported by Davis and James [112].

Velocity distribution in channels partially filled porous media has been studied

31

experimentally more recently by Tachie et al. [113], Agelinchaab et al. [114], and Arthur et al. [115] for porous media comprised of regular arrays of cylinders.

To capture the interface velocity distribution more accurately, sophisticated boundary conditions has been proposed by Ochoa-Tapia and Whitaker [116] and Sahraoui and Kaviany [38]. However, numerical simulations of Alazmi and Vafai [117] showed that the difference in the predicted velocity distributions using various boundary conditions was not significant.

2.4   Comparison of the existing models with experimental data

The existing models/correlations for permeability of 1D, 2D, 3D, and metalfoams, listed in Table 1, are compared with the experimental data collected from various sources. Based on Figure 8-Figure 12 and the literature review in Sections 2.1-2.3 the following conclusions can be made:

- The existing models for 1D, 2D, and 3D fibrous structures have limited ranges of accuracy and none of them can cover the entire range of porosity.

- Most of the existing models can only capture the trends of experimental data qualitatively.

- The effects of microstructure and geometrical parameters including fiber orientation and enclosing walls on flow properties of fibrous materials are not included in the majority of existing models.

- No analytical model exists for the permeability of gas diffusion layer of fuel cells.

- The existing models are incapable of predicting the experimental data for permeability of fibrous materials with complex microstructure such as metalfoams.

- Effects of GDL compression on the through-plane permeability have not been investigated.

- Experimental data for permeability of metalfoams are usually based on the measurements in high Reynolds number flow, Re > 1; thus, a lack of such experiments exists in the creeping flow regime.

- Accuracy of conventional theories developed for macro-scale confined porous media is not verified for microsystems. Moreover, the wall effects are not studied in micro-porous channels.

- Effects of geometrical and structural properties on the pressure drop inside channels partially filled with porous media are not investigated.

- Microscopic velocity distribution, which is required for heat and mass transfer analyses in fibrous media, is not available even for ordered arrays of cylinder.

In general, one can say that the exiting studies have provided useful insights, but remained limited to specific ranges of porosity, structure, and size scale. This clearly indicates the need for a fundamental study and mechanistic models that can accurately predict the mechanical properties such as permeability and tortuosity as a function of the microstructural properties.
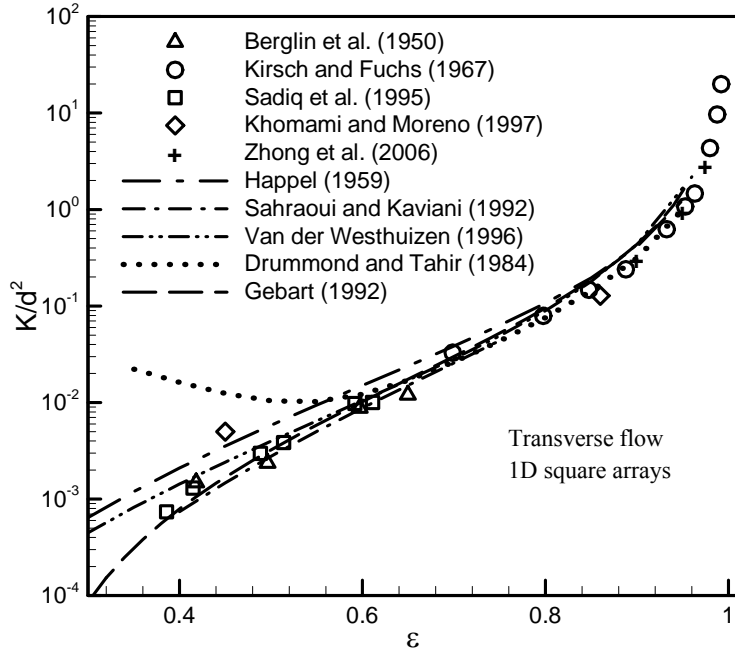
Figure 8: Comparison of the existing models for transverse (normal) flow permeability of square arrangements with experimental data.
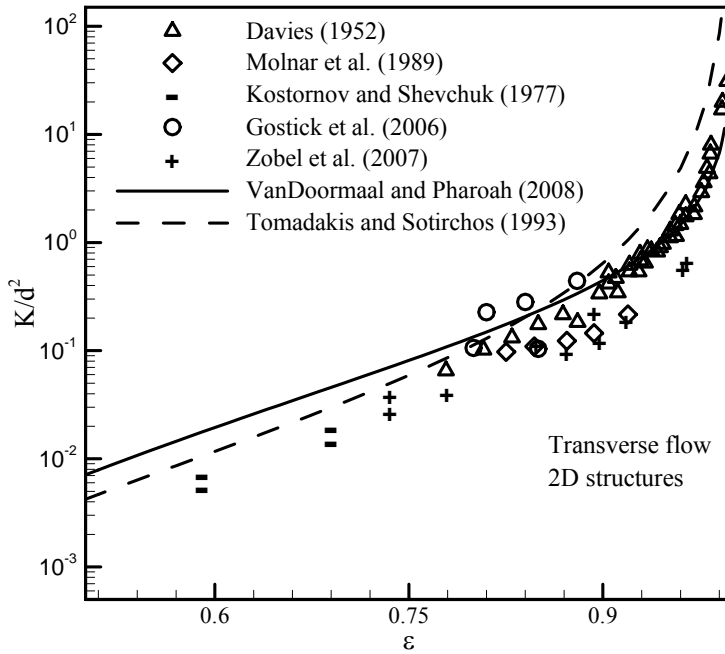
Figure 9: Comparison of the existing models for through-plane flow through two directional (2D) structures with experimental data.

34
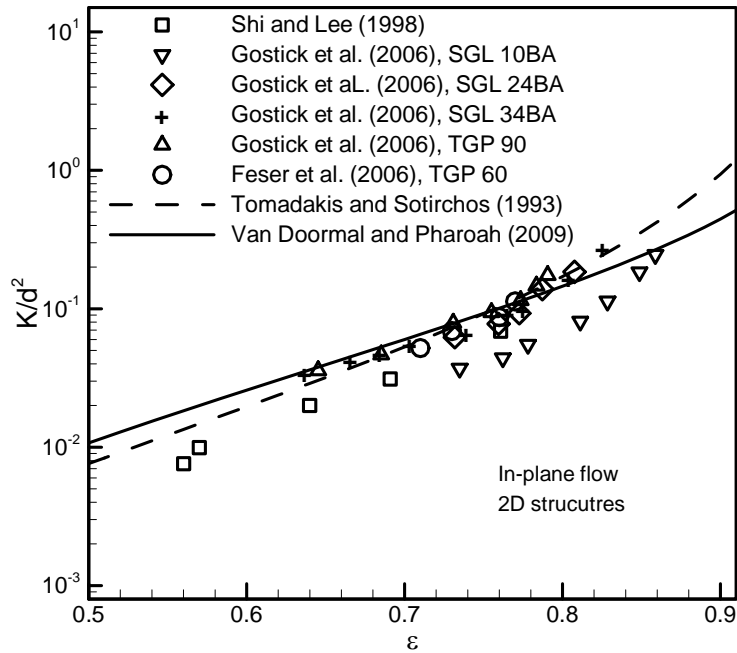
Figure 10: Comparison of the existing models for in-plane flow through two directional (2D) structures with experimental data.
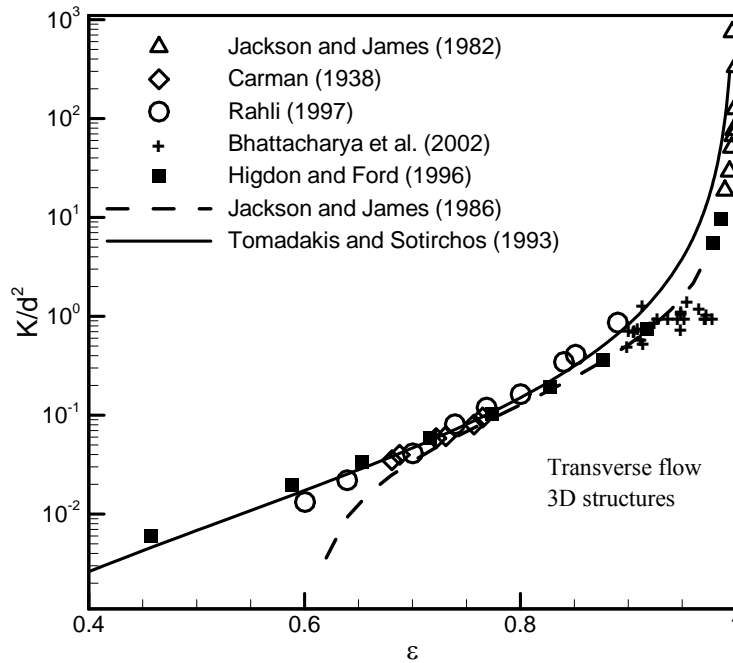
Figure 11: Comparison of the existing models for three directional (3D) structures with experimental data.
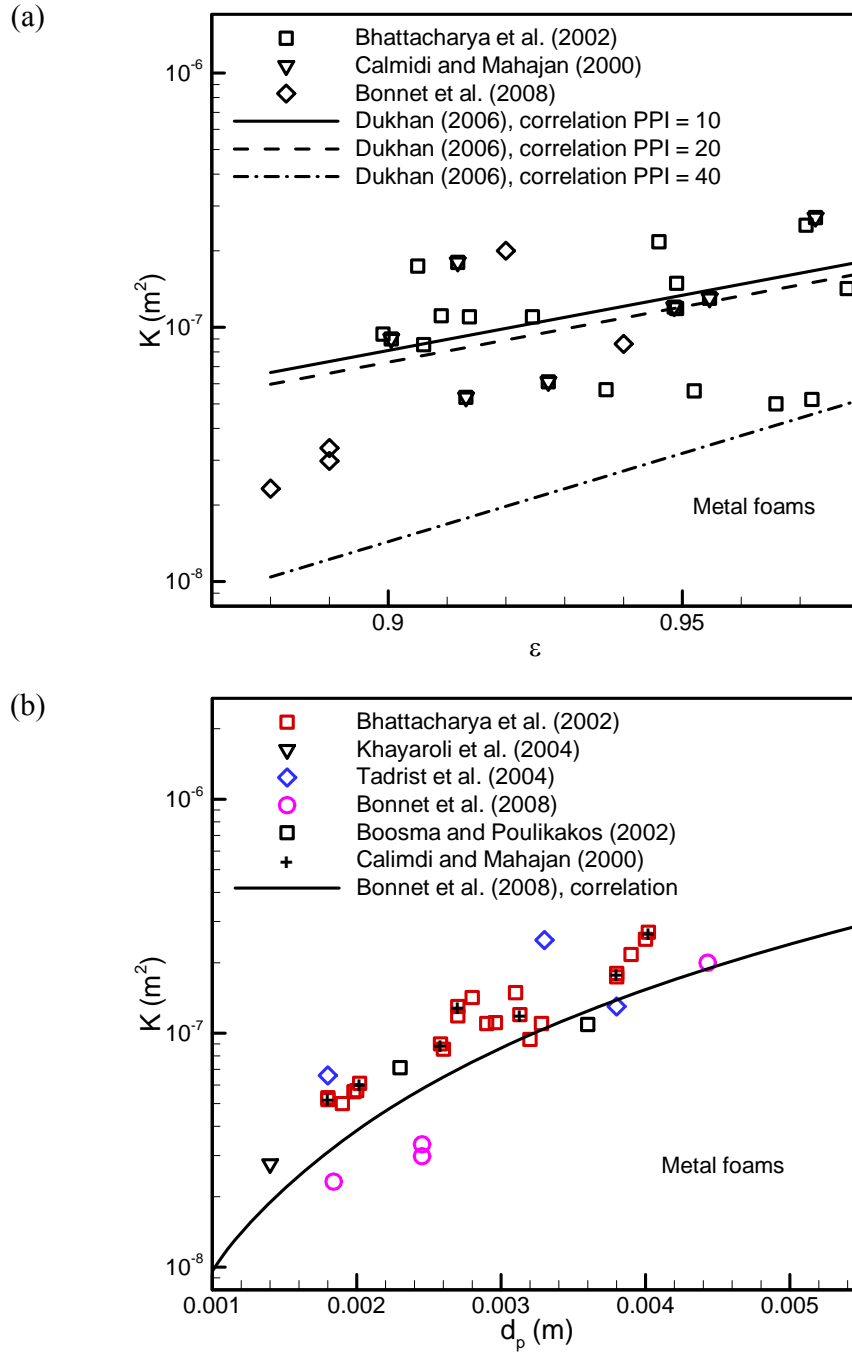
Figure 12: Comparison of the existing models for metalfoams a) Dukhan [98] and b) Bonnet at al. [97] with experimental data.

2.5   Modeling road map

Our critical review of the pertinent literature indicates the need for model(s) that can predict the permeability and inertial coefficient of fibrous porous materials. The main objectives of the current work are to:

- Develop comprehensive analytical model(s) that can predict the flow properties of fibrous materials.

- Investigate effects of the major relevant geometrical parameters such as porosity, pore diameter, fiber diameter, and fiber orientation on the flow properties of fibrous materials.

- Study the boundary effects on the macroscopic flow-field and the resulting pressure drop in confined porous media.

- Design and conduct an experimental program, using various fluids, to verify our theoretical investigation for permeability, inertial coefficient, and wall (boundary) effects.

The focus of the proposed study will be on developing and verifying general model(s) that predict the flow properties of fibrous porous media. Following other analytical studies, a basic cell approach will be used. Based on the microstructure and flow characteristics, various exact and approximate analytical techniques described in previous sections will be employed to predict pressure drop and permeability. The modeling road map in the present study is shown in Figure 13.

37

The developed models and the analytical solutions will be verified through comparison with numerical simulations and experimental measurements. Due to the diversity of the investigated problems, three test rigs have been designed to conduct experiments with different fluids, fibrous material types and sizes, and materials scales.
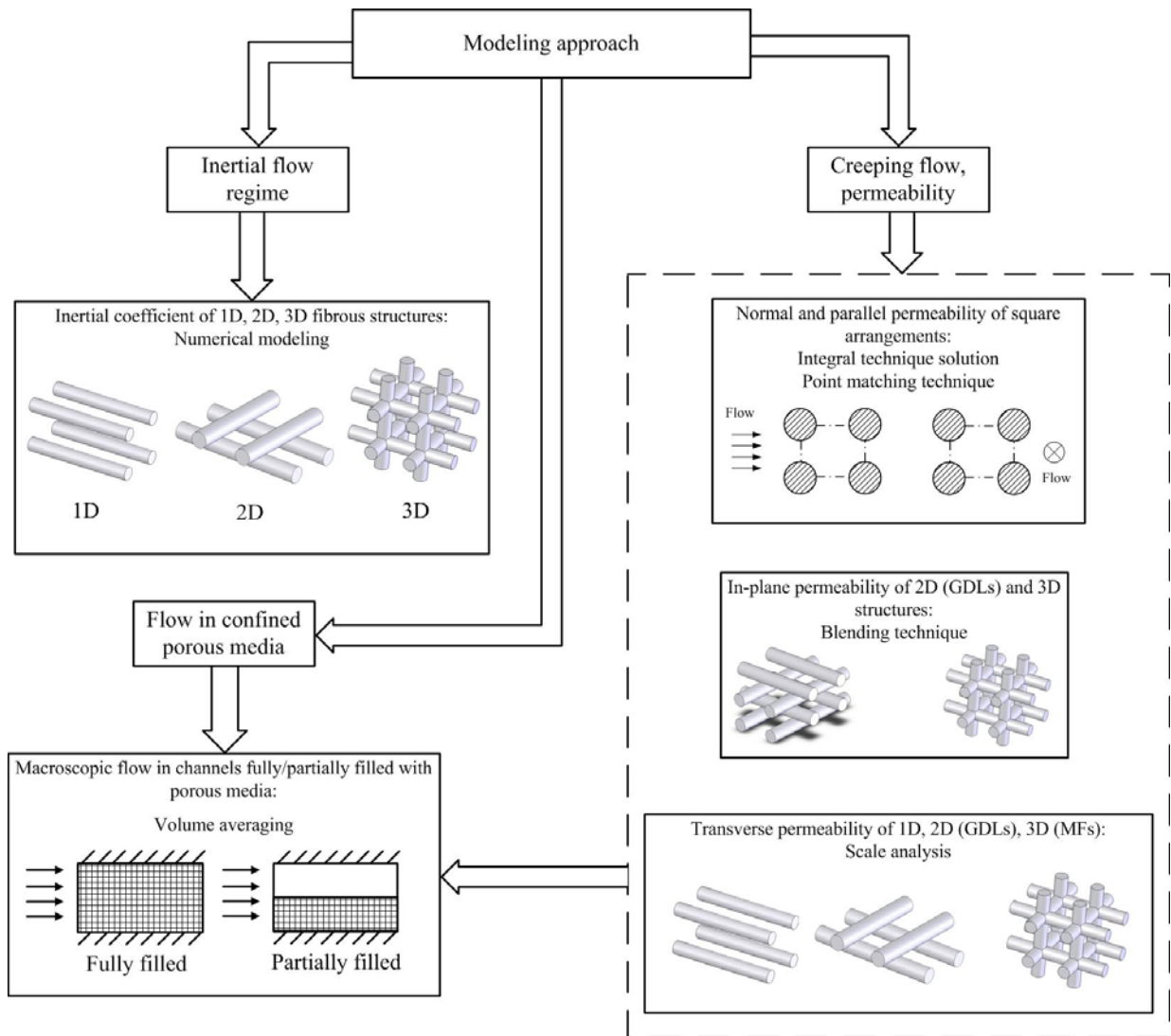
Figure 13: The modeling road map of the present dissertation.

3: FLOW PROPERTIES OF FIBROUS STRUCTURES (MICROSCOPIC ANALYSES)

The modeling road map, shown in Figure 13, has been followed. This chapter discusses the flow properties of fibrous porous media that can be evaluated through microscopic analysis of the media.

The simplest representations of fibrous porous media are regular ordered arrays of cylinders. First, compact models will be developed to predict the permeability of such structures in different directions. The analysis, then, will be extended to predict the permeability of more complex microstructures such as 2D and 3D fibrous matrices using various techniques such mixing rules and scale analysis. To cover a wider range of Reynolds numbers, numerical simulations are carried out to calculate the inertial coefficient in various ordered structures.

3.1 Permeability of 1D touching fibers

Since flow cannot pass perpendicular to touching fibers (see figures in Table 4), the normal permeability of these geometries is zero. Fluid passing parallel to the axis of unidirectional fibers experiences a channel-like flow; thus, the media is treated as a combination of parallel constant cross-sectional conduits. Therefore, the permeability can be related to the pressure drop in these channel-like conduits. In this approach, the cross sectional area and the perimeter of the channel are required. Pressure drop can be calculated using Darcy-Weisbach relation [118]:

$$\frac{dP}{dz} \approx \frac{\Delta P}{L} = f \frac{\rho U_D^2}{2\varepsilon^2 D_h} \tag{12}$$
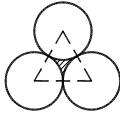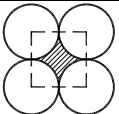
where D_h is the hydraulic diameter, L is the channel depth, f is the Fanning friction factor, and ε and U_D represent the porosity and the volume-averaged superficial velocity, respectively. Using Eq. (12) the permeability becomes:

$$K_{D-W} = f \frac{2\varepsilon^2 \mu D_h}{f \rho U_D} \tag{13}$$

Bahrami et al. [119] proposed a general model that predicts the pressure drop for arbitrary cross-sectional channels. In the model of [119], pressure drop is related to geometrical parameters of the cross section:

$$\frac{\Delta P}{L} = \frac{16\pi^2 \mu U_D}{A\varepsilon} I_p^*, \quad I_p^* = \frac{I_p}{A^2} \tag{14}$$

Table 4: Parallel permeability of touching fibers.

Porosity (ε)	Unit Cell	K^*, Eq. (15)	K^*, Data [60]	Relative Difference (%)
0.094*		0.000088	0.000083	5.6
0.215†		0.00147	0.00121	17.6

$$^* \varepsilon = \frac{\pi d^2}{2\sqrt{3}S^2}, S = d$$

$$^\dagger \varepsilon = \frac{\pi d^2}{4S^2}, S = d$$

where I_p, A, ε are the polar moment of inertia, the area of the passage cross-section, and the porosity, respectively. Using the Darcy's relationship and the model of [119], the non-dimensional permeability of periodic touching fibrous media can be found as:

$$K^* = \frac{K}{d^2} = \frac{A\varepsilon}{16\pi^2 I_p^*} \tag{15}$$

This relationship can be easily applied to any touching fibrous arrangements including; triangular, rectangular, hexagonal, and checker boarding.

In Table 4, the values calculated form Eq. (15) are compared with the experimental data reported by Sullivan [60] for air flowing through staggered and square arrangements of copper wires, respectively. The difference between the predicted values by the proposed model and the experimental data is reasonable within the context of porous media. Equation (15) is also applicable to any foam like materials.

3.2   Determination of the normal permeability of square fiber arrangements (integral technique)

A powerful method for analyzing fluid mechanic problems without knowing the exact velocity distribution, is the integral technique solution. In this approach, a general shape of the velocity profile that satisfies conservation of mass and momentum on the boundaries is assumed. Then, using the assumed velocity distribution the flow equation is integrated over the entire region and the resulting pressure drop is determined.
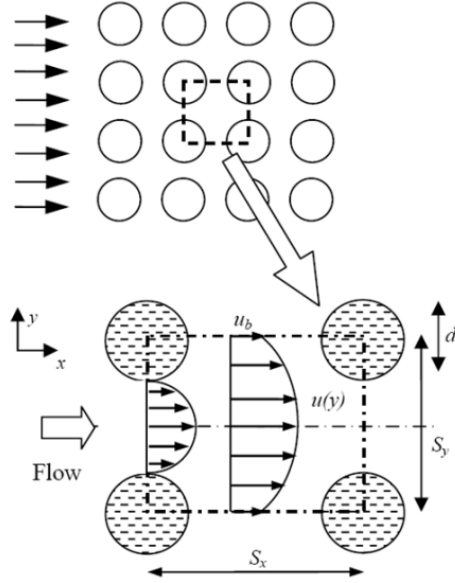
Figure 14: Rectangular arrangement of cylinders and the considered unit cell.

For the square arrangement of fibers shown in Figure 14, the unit cell (the smallest region which has identical flow properties to the whole media) is selected as the space between parallel cylinders. The porosity for this arrangement is:

$$\varepsilon = 1 - \frac{\pi d^2}{4S^2} \tag{16}$$

The permeability is related to the total pressure drop through the unit cell; see Eq. (1). Employing lubrication theory and neglecting inertial terms, the x-momentum equation reduces to Stokes equation:

$$\frac{\partial^2 u}{\partial y^2} = \frac{1}{\mu}\frac{dP}{dx} \tag{17}$$

Determination of the exact velocity profile requires detail knowledge of the geometry of the medium which is not feasible in the case of porous media. Moreover, even with specified geometry and boundary conditions, finding exact analytical solution

42

is not guaranteed and is a difficult task for most cases. To overcome this problem, an integral method is employed in this study. The integral method provides a powerful technique for obtaining accurate but approximate solutions to rather complex problems with remarkable ease. The basic idea is that we assume a general shape of the velocity profile. It must be noted that we are not interested in the precise shape of velocity profile but rather need to know the pressure drop over the basic cell to calculate permeability. This can be accomplished by satisfying conservation of mass and momentum in a lumped fashion across the unit cell. As a result, an approximate parabolic velocity profile is considered which satisfies the boundary conditions within the unit cell. The border velocity is zero on the edge of the cylinders (no-slip condition) and reaches its maximum value at the half distance between cylinders in the x-direction, see Figure 14. It is also assumed that the maximum border velocity is a function of the porosity [71], i.e., as the porosity increases the maximum border velocity increases accordingly. For lower porosities, the border velocity is very small and for highly porous limits, it approaches to the Darcy velocity. In this study, the border velocity increases linearly from the edge of the fibers ($u_b = 0$) to its peak at the center of the unit cell:

$$
\begin{aligned}
u_b &= U_D \, g(\varepsilon) \frac{2x}{S-d}, \quad \frac{d}{2} \leq x \leq \frac{S}{2} \\
g(\varepsilon) &= 1.274\varepsilon - 0.274
\end{aligned}
\tag{18}
$$

Moreover, the maximum border velocity is related to porosity through $g(\varepsilon)$ where $g(0.215) = 0$ for touching fibers and $g(1) = 1$ for high porosity limits. Therefore, the following velocity distribution is considered:

43

$$u = \frac{1}{2\mu}\frac{dP}{dx}\begin{cases} \left(\left[\frac{S}{2}-\sqrt{\frac{d^2}{4}-x^2}\right]^2 - y^2\right), & 0 \le x \le \frac{d}{2} \\ \left(\frac{S^2}{4}-y^2\right)+g(\varepsilon)\frac{2x}{S-d}U_D, & \frac{d}{2} \le x \le \frac{S}{2} \end{cases} \tag{19}$$

The total pressure drop of the unit cell is calculated employing an integral technique solution. In this approach, using continuity equation and the definition of volumetric flow rate, one can calculate pressure gradient as:

$$\frac{dp}{dx} = \frac{3\mu Q}{\left(\frac{S}{2}-\sqrt{\frac{d^2}{4}-x^2}\right)^3}, \quad 0 \le x \le \frac{d}{2} \tag{20}$$

$$\frac{dP}{dx} = \frac{12\mu Q}{S^3}(S-d)\left[1-g(\varepsilon)\frac{2x}{S-d}\right], \quad \frac{d}{2} \le x \le \frac{S}{2} \tag{21}$$

The pressure drop in the basic cell is calculated as:

$$\Delta P_{unit\,cell} = 6\mu Q\left\{\frac{2d}{(S^2-d^2)S} + \frac{3d^2 S\left[\tan^{-1}\left(\frac{d}{\sqrt{S^2-d^2}}\right)+\frac{\pi}{2}\right]}{\left(S^2-d^2\right)^{\frac{5}{2}}}\right\} \tag{22}$$

$$+ \frac{12\mu Q}{S^3}(S-d)\left[\frac{2-g(\varepsilon)}{2}\right]$$

Using the Darcy equation and introducing solid fraction as $\varphi = 1-\varepsilon$, the permeability of square arrangement becomes:

$$K^* = \left\{ \frac{12\left(\sqrt{\varphi'}-1\right)}{\varphi'\sqrt{\varphi'}}\left[\frac{2-g(\varepsilon)}{2}\right] + \frac{18+12(\varphi'-1)}{\sqrt{\varphi'}(1-\varphi')^2} + \frac{18\sqrt{\varphi'}\left[\tan^{-1}\left(\frac{1}{\sqrt{\varphi'-1}}\right)+\frac{\pi}{2}\right]}{(\varphi'-1)^{\frac{5}{2}}} \right\}^{-1} \quad (23)$$

where $K^* = K/d^2$, $g(\varepsilon) = 1.274\varepsilon - 0.274$, and $\varphi' = \pi/4\varphi$. In Figure 15, Eq. (23) is compared with experimental data collected from several sources [61, 63, 68, 71, 120]. The $\pm 15\%$ bounds of the model are also shown in the plot, to better demonstrate the agreement between the data and the model. The experiments were conducted using different fluids including: air, water, oil, and glycerol with a variety of porous materials such as metallic rods, glass wool, and carbon. It can be seen that the proposed model, i.e., Eq. (23), accurately predicts the trend of experimental data for square arrangement of fibers over the entire range of porosity [121].

To further investigate the accuracy of the assumed velocity distribution, creeping flow through the unit cell shown in Figure 14 was solved numerically using Fluent software [122]. Structured numerical grids with aspect ratios in the range of 1-5 were generated using Gambit [122]. SIMPLE algorithm was employed for pressure-velocity coupling [123].

Although fully-developed solution for normal flow can be found by simulating a single basic cell and applying periodic boundary condition to determine the developing length for flow in the medium, a set of 7-10 unit cells in series are considered and velocity profiles are compared at the entrance to each unit cell; details of the numerical results are provided in Appendix C. The inlet velocity of the media was assumed to be uniform. Constant pressure boundary condition was applied on the computational domain outlet.
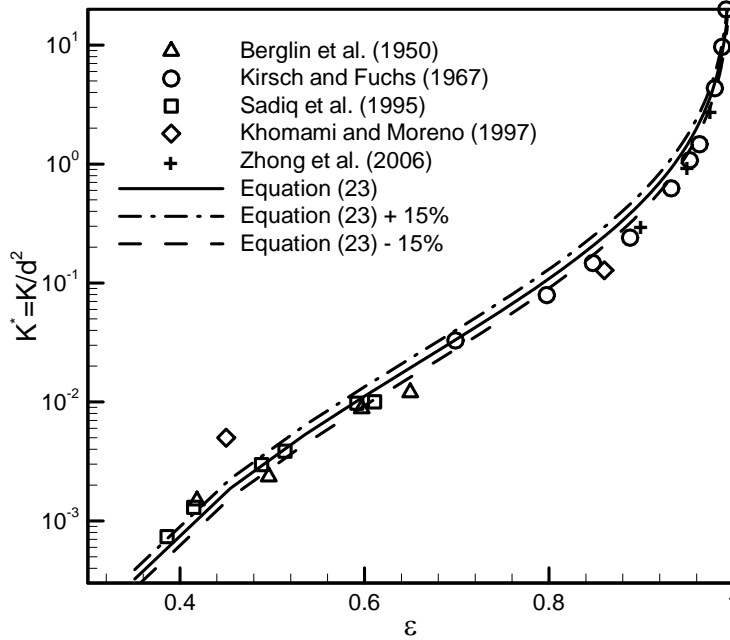
Figure 15: Comparison of the present model for permeability of square arrays of fibers with experimental data.

The symmetry boundary condition was applied on the side borders of the considered unit cells; this means that the normal velocity and the gradient of the parallel component of velocity on the side borders are zero; see Figure 16a.

In Figure 16b, the numerically calculated velocity profiles are compared with the experimental data of Zhong et al. [71] for the normal flow through the fibrous media with $\varepsilon = 0.9$ in several locations. From Figure 17, it is clear that the parabolic velocity assumption is not realistic. After considerable investigations, the following distribution is in a better agreement with the numerical results:

$$u = U_{\max} \delta^2 e^{-\frac{\zeta^2}{2\sigma}} \left(1 - \zeta^2\right), \quad \zeta = \frac{y}{\delta(x)}, \quad \delta = \frac{S}{2} - \sqrt{\frac{d^2}{4} - x^2} \tag{24}$$

where σ is a constant, and δ is half of the distance between surface of adjacent fibers. To improve the accuracy of our previous model, a modifying function is defined such that

46

compensates for the difference between the numerical values of pressure drop and those obtained from parabolic velocity assumption on the cylinders:

$$\Delta P = \Delta P_{parabolic} \times f(\varepsilon) \qquad (25)$$

(a)

(b)
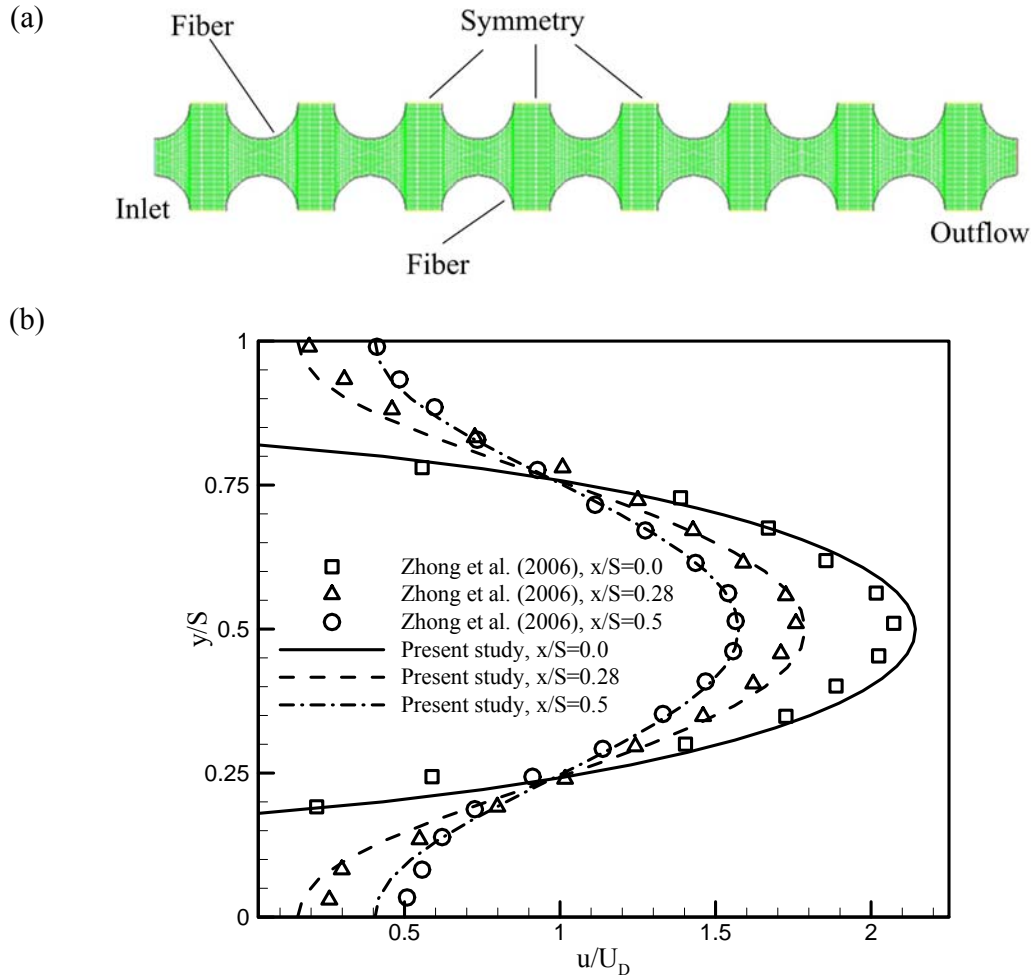
Figure 16: a) A typical numerical grid and the boundary conditions used in the analysis for $\varepsilon = 0.65$, b) comparison of the present numerical and the experimental data for the velocity profiles in normal flow and $\varepsilon = 0.9$.
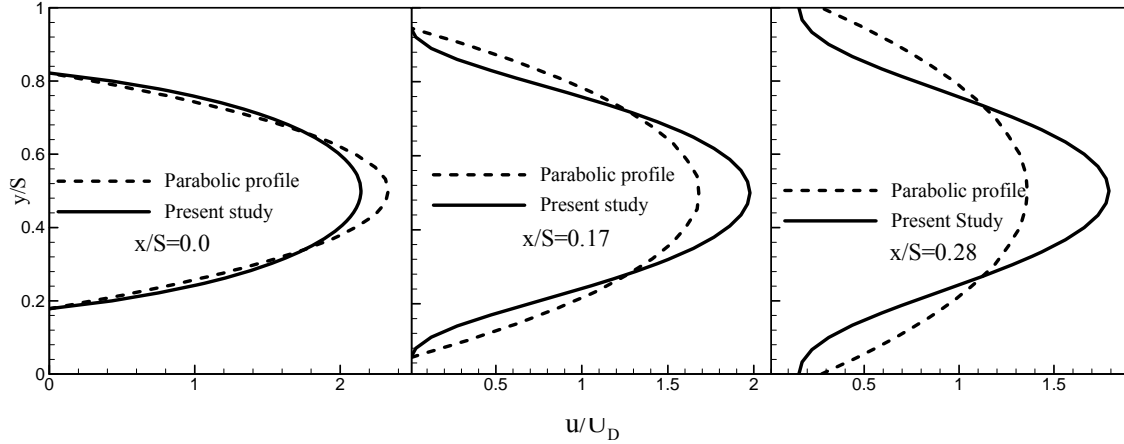
Figure 17: Comparison of the present numerical and parabolic velocity profiles in normal flow, $\varepsilon = 0.9$.

Several functions were tested and the following correlation was found accurate for predicting the correction function:

$$f(\varepsilon) = (1.343 - 1.341\varepsilon)^{-1/2.58} \tag{26}$$

Therefore, the normal permeability of square arrangement becomes:

$$K^* = \left\{ \frac{18 + 12(\varphi' - 1)}{\sqrt{\varphi'}(1 - \varphi')^2} + \frac{54\pi\sqrt{\varphi'}}{4(\varphi' - 1)^{2.5}} \right\}^{-1} \times \left(1.343 - 1.341\left(1 - \frac{\pi}{4\varphi'}\right) \right)^{1/2.58},$$

$$\varphi' = \frac{\pi}{4(1 - \varepsilon)} \tag{27}$$

This equation can predict the numerical results within 5% accuracy over the entire range of porosity.

3.3   Parallel permeability of ordered arrangements

In the following sub-sections, parallel flow through various ordered arrangements, shown in Figure 18, will be investigated [124].

Using geometric symmetry, only the selected regions of the unit cells are considered in the analysis. The solid volume fraction (φ) and porosity (ε) of square, staggered, and hexagonal arrays are:

$$\varphi = 1 - \varepsilon = \begin{cases} \dfrac{\pi d^2}{4S^2} & \text{Square} \\[3mm] \dfrac{\pi d^2}{2\sqrt{3}S^2} & \text{Staggered} \\[3mm] \dfrac{\pi d^2}{3\sqrt{3}S^2} & \text{Hexagonal} \end{cases} \qquad (28)$$

Therefore, the minimum possible values of ε for square, staggered, and hexagonal arrangements with no overlapping are 0.215, 0.094, and 0.395, respectively. These values indicate the touching limit of fibers.

The conservation of linear momentum, Poisson's equation, in the cylindrical coordinate system reads:

$$\frac{\partial^2 w}{\partial r^2} + \frac{\partial w}{r \partial r} + \frac{\partial^2 w}{r^2 \partial \theta^2} = \frac{1}{\mu}\left(\frac{dP}{dz}\right) \qquad (29)$$

where w is the velocity component in the z-direction. Following Sparrow and Loeffler [30], the general solution of the Poisson's equation in the cylindrical coordinate is considered:

$$w = A + B\ln r + \frac{r^2}{4\mu}\left(\frac{dP}{dz}\right) + \sum_{k=1}^{\infty}\left(C_k r^k + D_k r^{-k}\right)\left(E_k \cos k\theta + F_k \sin k\theta\right) \qquad (30)$$

For square arrangement, symmetry lines are located at $\theta = 0$ and $\theta = \pi/4$. The first condition results in $F_k = 0$ and the second condition holds when $k = 4, 8, 12, \ldots$. The no-slip boundary condition on the solid walls leads to:

$$D_k = C_k r_0^{2k} \quad and \quad A = -B \ln r_0 - \frac{r_0^2}{4\mu}\left(\frac{dP}{dz}\right) \tag{31}$$
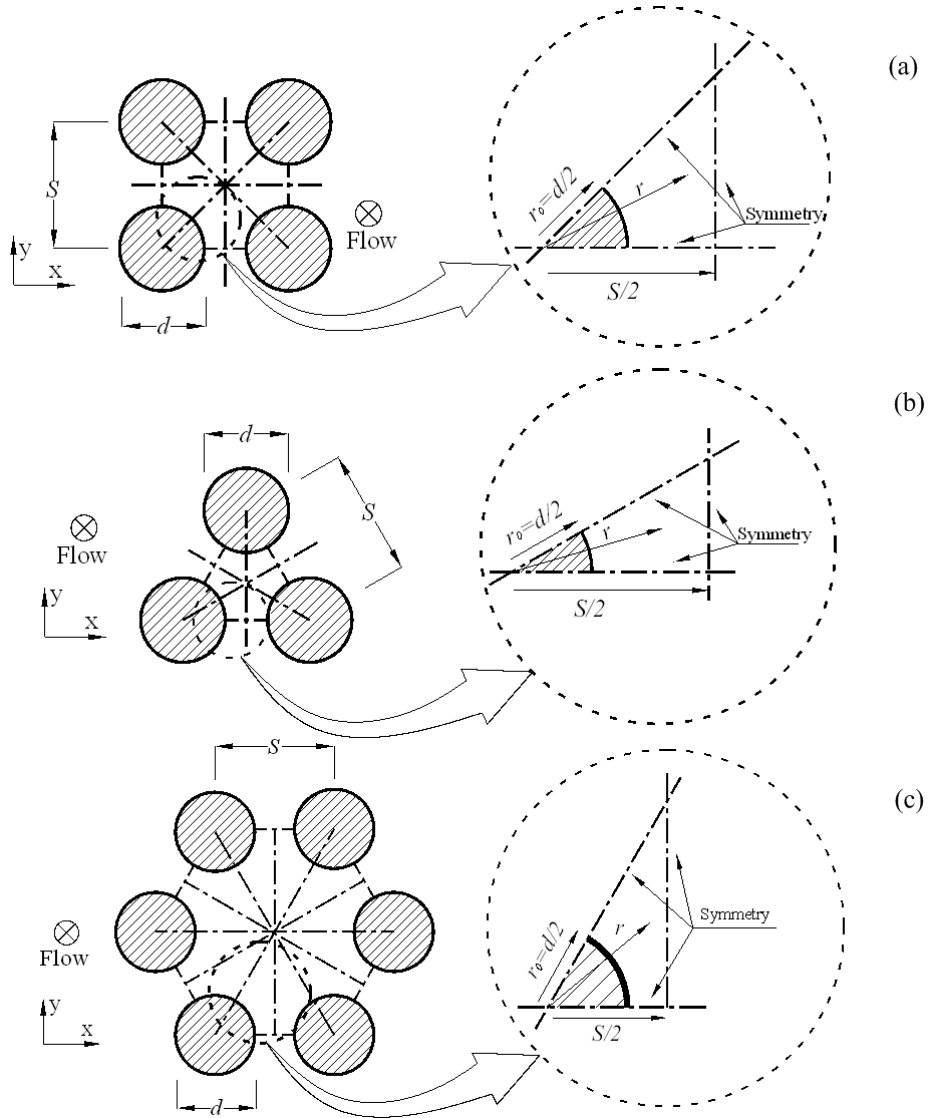
Figure 18: Unit cell for a) square, b) staggered, and c) hexagonal arrangements.

50

Total frictional force exerted on the fluid by solid rods must be balanced by the net pressure force acting over the entire cross-section of the basic cell:

$$\int_0^{\pi/4} \mu \left(\frac{\partial w}{\partial r} \right)_{r=r_0} r_0 \, d\theta = \int_0^{\pi/4} \int_{r_0}^{S/2\cos\theta} \left(-\frac{dP}{dz} \right) r \, dr \, d\theta \tag{32}$$

Solving for Eq. (32), the constant B can be found:

$$B = -\frac{S^2}{2\pi\mu} \left(\frac{dP}{dz} \right) \tag{33}$$

Consequently, the velocity distribution becomes:

$$w^* = \left[\frac{2S^2}{\pi d^2} \ln\eta - \frac{\eta^2 - 1}{4} + \sum_{k=1}^{\infty} \frac{G_k \, d^{4k-2}}{2^{4k} S^{4k-2}} \left(\eta^{4k} - \eta^{-4k} \right) \cos 4k\theta \right],$$

$$w^* = \frac{w}{-\dfrac{d^2}{4\mu} \left(\dfrac{dP}{dz} \right)} \quad , \quad \eta = \frac{r}{d/2} \tag{34}$$

The last constant, G_k, is found by applying the symmetry condition on the unit cell border where $r = S/(2\cos\theta)$. Therefore, one can write:

$$\frac{2}{\pi} (\cos\theta)^2 - \frac{1}{2} +$$

$$\sum_{k=1}^{\infty} \frac{g_k}{\cos\theta^{4k-1}} \left[\cos(4k-1)\theta + \left(\frac{d\cos\theta}{S} \right)^{8k} \cos(4k+1)\theta \right] = 0 \tag{35}$$

where:

$$g_k = G_k \, 4k \left(\frac{S}{2} \right)^{4k-2} \tag{36}$$

51

Sparrow and Loeffler [30] applied Eq. (35) at a finite number of points along the boundary and solved the resulting set of linear equations to determine the unknown coefficients, i.e., g_k. The same approach is followed here and the calculated coefficients for several porosities are listed in Table 5. The listed values are in agreement with the values reported by Sparrow and Loeffler [30].

The triangular unit cell section for the staggered fiber arrangements is shown in Figure 18b. The symmetry boundaries are located at $\theta = 0$ and $\theta = \pi/6$. The governing equation and its general solution are still Eqs. (29) and (30). Following the same procedure described above and applying symmetry boundary conditions, one can find:

$$w^* = \left[\frac{\sqrt{3}S^2}{\pi d^2} \ln \eta - \frac{\eta^2 - 1}{4} + \sum_{k=1}^{\infty} \frac{g_k}{6k} \left(\frac{d}{S} \right)^{6k-2} \left(\eta^{6k} - \eta^{-6k} \right) \cos 6k\theta \right] \tag{37}$$

The unknown coefficients are evaluated with the same approach used for square arrangements and the results as listed in Table 5.

Adopting the same approach and considering the location of the symmetry lines for hexagonal arrays at $\theta = 0$ and $\theta = \pi/3$, the velocity distribution can be found as:

$$w^* = \left[\frac{3\sqrt{3}S^2}{2\pi d^2} \ln \eta - \frac{\eta^2 - 1}{4} + \sum_{k=1}^{\infty} \frac{g_k}{3k} \left(\frac{d}{S} \right)^{3k-2} \left(\eta^{3k} - \eta^{-3k} \right) \cos 3k\theta \right] \tag{38}$$

The unknown coefficients are listed in Table 5. From the listed coefficients in Table 5 and the form of the series solutions in Eqs. (34), (37), and (38), it is expected that truncating the series from the second term, does not affect the velocity distributions significantly. Our analysis also showed that substituting g_1 with an average value has a

negligible impact on the predicted results (less than 4 percent). Therefore, g_1 is replaced by -0.107, -0.0437, and -0.246 for square, staggered, and hexagonal arrangements, respectively. Hence, the velocity distributions become [124]:

Table 5: Calculated coefficients in velocity distribution.

S/d	ε	g_1	g_2	g_3	g_4	g_5
Square arrangement						
4.0	0.95	-0.1253	-0.0106	-0.0006	0	0
2.0	0.80	-0.1250	-0.0105	-0.0006	0	0
1.5	0.65	-0.1225	-0.0091	-0.0002	0	0
1.2	0.45	-0.1104	-0.0024	-0.0015	0.0003	0
1.1	0.35	-0.0987	0.0036	0.0029	0.0005	0
1.05	0.29	-0.0904	0.0073	0.0032	0.0002	0
Staggered arrangement						
S/d	ε	g_1	g_2	g_3	g_4	g_5
4.0	0.94	-0.0505	-0.0008	0.0000	0	0
2.0	0.77	-0. 0505	-0.0008	0.0000	0	0
1.5	0.60	-0. 0502	-0.0007	0.0001	0	0
1.2	0.37	-0. 0469	0.0007	0.0002	0.0000	0
1.1	0.25	-0.0416	0.0028	0.0004	0.0000	0
1.05	0.18	-0.0368	0.0043	0.0003	-0.0001	0.0000
Hexagonal arrangement						
S/d	ε	g_1	g_2	g_3	g_4	g_5
4.0	0.96	-0.2850	-0.0365	-0.0048	-0.0006	-0.0001
2.0	0.85	-0.2827	-0.0350	-0.0043	-0.0005	0.0000
1.5	0.73	-0.2728	-0.0286	-0.0019	0.0002	0.0001
1.2	0.58	-0.2433	-0.0096	0.0053	0.0021	0.0006
1.1	0.50	-0.2216	0.0038	0.0093	0.0029	0.0004
1.05	0.45	-0.2076	0.0116	0.0103	0.0027	-0.0003

$$
w^* =
\begin{cases}
\dfrac{2\,S^2}{\pi\,d^2}\ln\eta - \dfrac{\eta^2-1}{4} - \dfrac{0.0287\,d^2}{S^2}\left(\eta^4 - \eta^{-4}\right)\cos 4\theta & \text{Square} \\[2ex]
\dfrac{\sqrt{3}\,S^2}{\pi\,d^2}\ln\eta - \dfrac{\eta^2-1}{4} - \dfrac{0.007\,d^4}{S^4}\left(\eta^6 - \eta^{-6}\right)\cos 6\theta & \text{Staggered} \\[2ex]
\dfrac{3\sqrt{3}\,S^2}{2\pi\,d^2}\ln\eta - \dfrac{\eta^2-1}{4} - \dfrac{0.082\,d}{S}\left(\eta^3 - \eta^{-3}\right)\cos 3\theta & \text{Hexagonal}
\end{cases}
\tag{39}
$$

3.3.1 Numerical simulations

Due to the lack of experimental and numerical data for parallel flow through ordered arrangements of fibers [15], a numerical study is performed using Fluent software [122] to verify the velocity distributions reported in Eq. (39). Structured grids are generated using Gambit [122], the preprocessor in the Fluent [122] package; numerical grid aspect ratios are kept in the range of 1-5. Fluent [122] is a finite volume based code and a second order upwind scheme is selected to discretize the governing equations. SIMPLE algorithm is employed for pressure-velocity coupling.

The inlet velocity to the media is assumed to be uniform; this assumption allows one to study the developing length. To ensure that the fully-developed condition is achieved, as shown in Figure 19, very long cylinders are considered, i.e., $L/d > 40$; the fully-developed section pressure drops are used for calculating the permeability. Constant pressure boundary condition is applied on the computational domain outlet. The symmetry boundary condition is applied on the side borders of the unit cells. Grid independence is tested for different cases and the size of computational grids used for each geometry is selected such that the maximum difference in the predicted values for pressure gradient is less than 2%. The convergence criterion, i.e., the maximum relative error in the value of dependent variables between two successive iterations, is set at 10^{-6}.
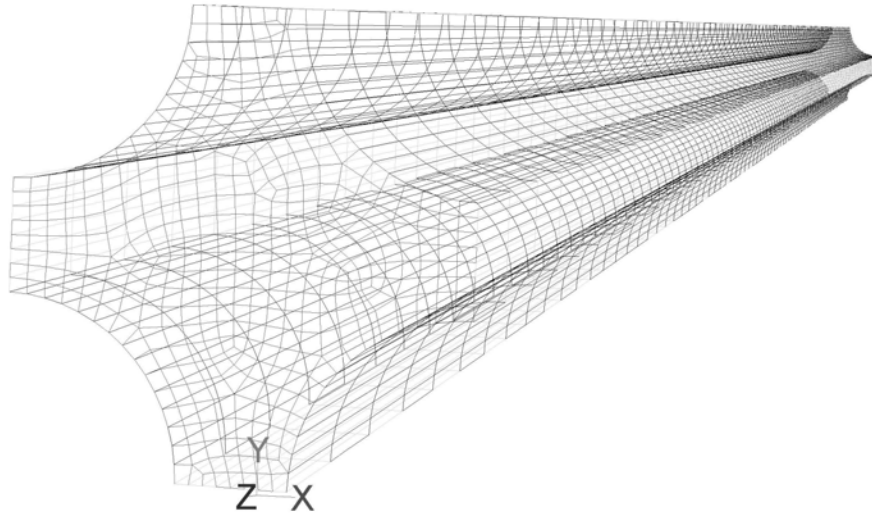
Figure 19: A typical numerical grid used in the numerical analysis a square arrangement with $\varepsilon = 0.9$.

To verify the proposed velocity distribution for the square arrangements, numerical and analytical velocity profiles are plotted in Figure 20 and Figure 21 for square and staggered arrangements. The velocity magnitudes are nondimensionalized using the volume averaged velocity, U_D. These figures indicate that Eq. (39) accurately predicts the velocity distribution in the considered geometries.

3.3.1 Parallel permeability

Velocity distributions are developed analytically for parallel flow through square, staggered, and hexagonal arrays of cylinders in previous sections. Moreover, the flow-fields are solved numerically to verify the theoretical results. The volumetric flow rate that passes through the medium is found by integrating Eq. (39) over the pore area. Substituting for dP/dz from Darcy's equation and using the solid volume fraction definitions for square arrangement of fibers, the non-dimensional permeability is simplified as:
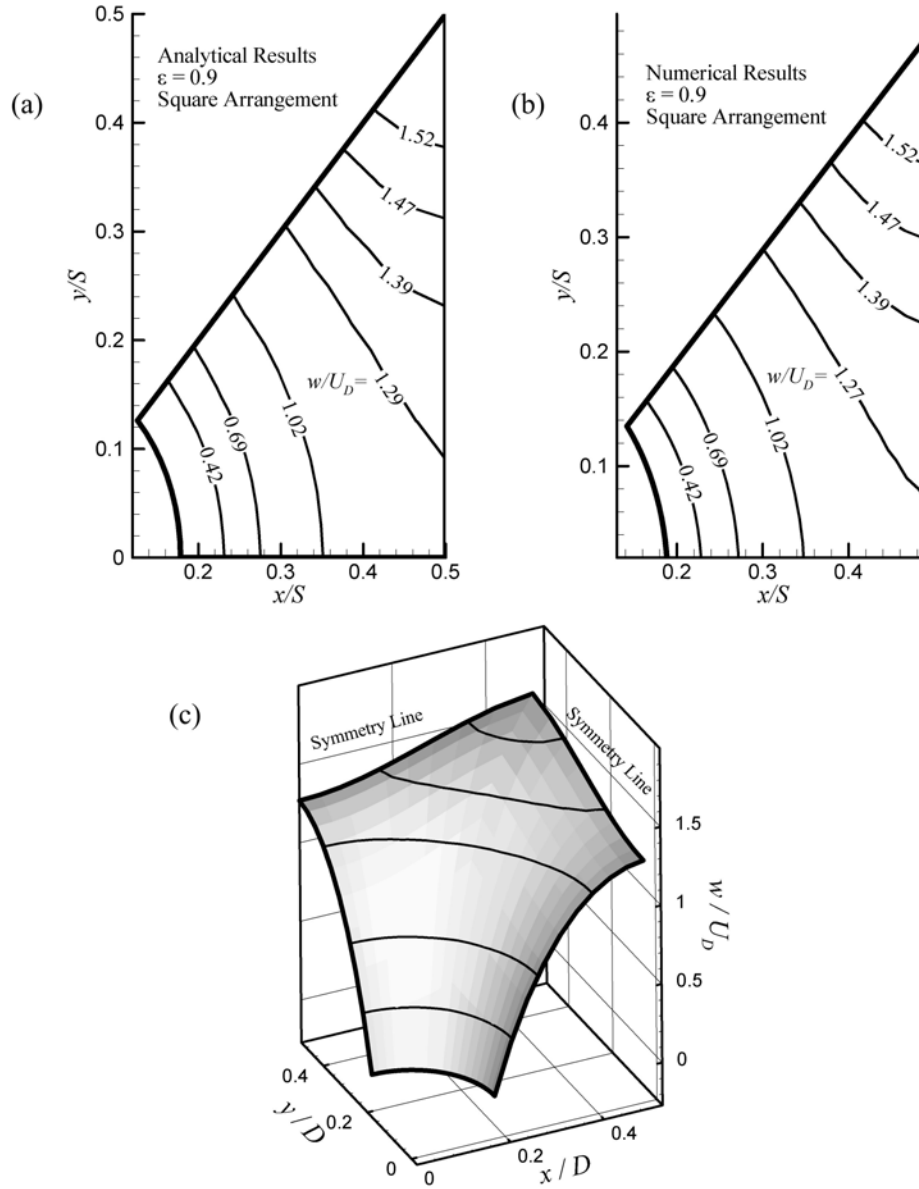
Figure 20: a) analytical velocity contours, Eq. (39), b) numerical velocity contours, and c) analytical velocity distribution for a square arrangement with $\varepsilon = 0.9$.
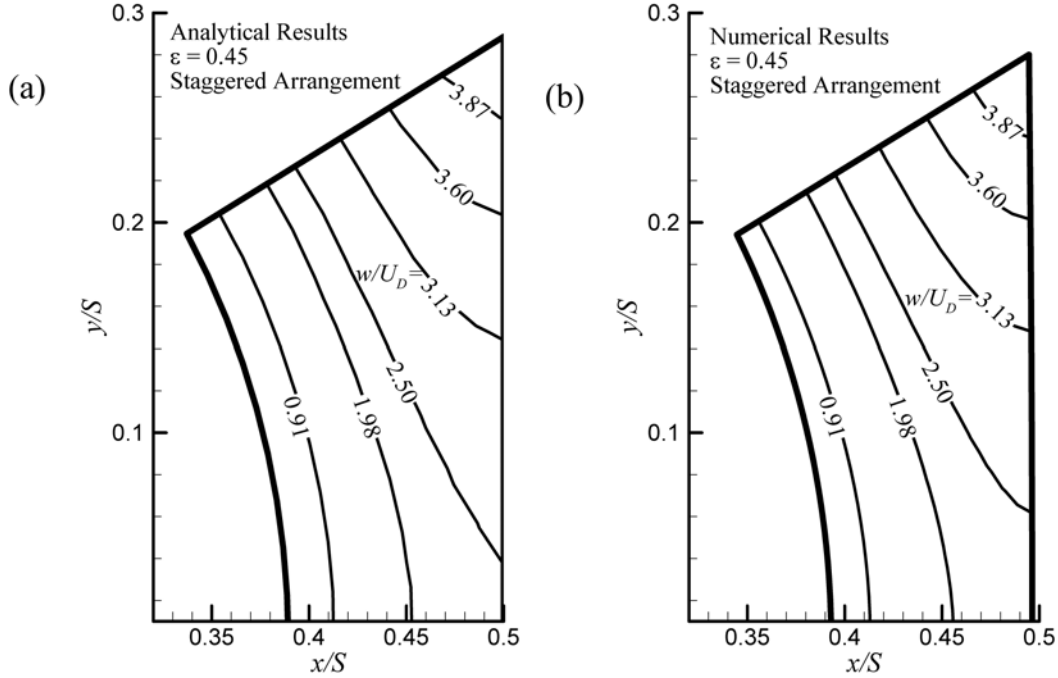
Figure 21: Present velocity distributions for staggered arrangement of cylinders with $\varepsilon = 0.45$ a) analytical, Eq. (39), and b) numerical.

$$K^* = \frac{K}{d^2} = \begin{cases} \dfrac{1}{16\varphi}\left[-1.479 - \ln\varphi + 2\varphi - \dfrac{\varphi^2}{2} - 0.0186\varphi^4\right] & \text{Square} \\[3mm] \dfrac{1}{16\varphi}\left[-1.498 - \ln\varphi + 2\varphi - \dfrac{\varphi^2}{2} - 0.0018\varphi^6\right] & \text{Staggered} \\[3mm] \dfrac{1}{16\varphi}\left[-1.354 - \ln\varphi + 2\varphi - \dfrac{\varphi^2}{2} - 0.258\varphi^3\right] & \text{Hexagonal} \end{cases} \tag{40}$$

To verify the proposed model, the parallel permeability of square arrays, Eq. (40), the results of numerical simulations, experimental data of Sullivan [60] and Skartsis et al. [36] and the numerical results reported by Sangani and Yao [39] are plotted in Figure 22. Moreover, the present solution is compared with the analytical models of Happel [28], Drummond and Tahir [32], and Tamayol and Bahrami [121] in Figure 22.

57

Figure 22 shows that the present model is in agreement with the experimental and the numerical data over the entire range of porosity. The maximum difference of the present model with numerical and experimental data is less than 8%.

In Figure 23, the present model for staggered fiber arrangement is compared with the numerical results, an experimental data reported by Sullivan [60], and the models of Happel [28] and Drummond and Tahir [32]. In addition, the permeability of touching fibers is calculated from the solution of Shit [125] for touching fibers and is included in Figure 23. This figure shows that the present model is accurate over the entire range of porosity (less than 8% deviations); especially, in lower porosities where the other models fail.
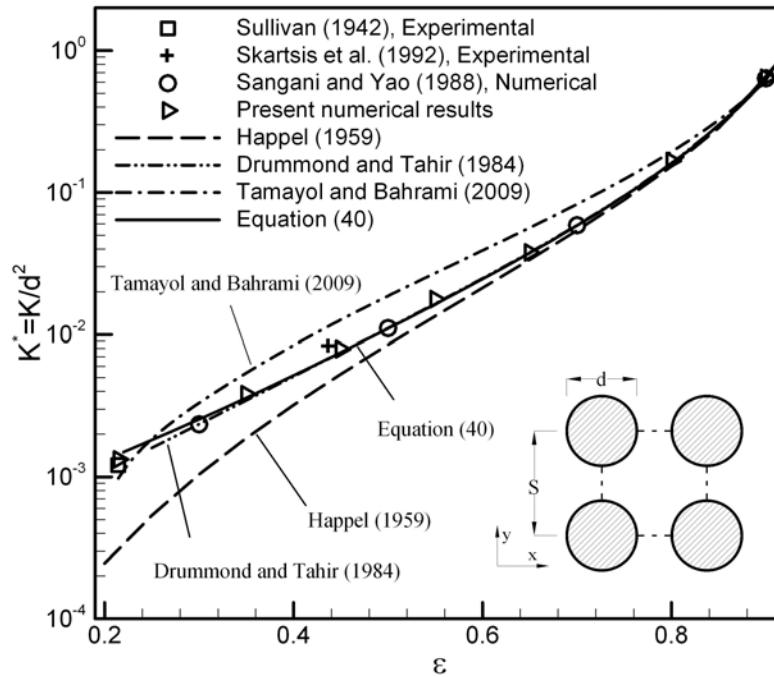
Figure 22: Comparison of the proposed model for parallel permeability of square arrangements of cylinders, experimental and numerical data, and other existing models.
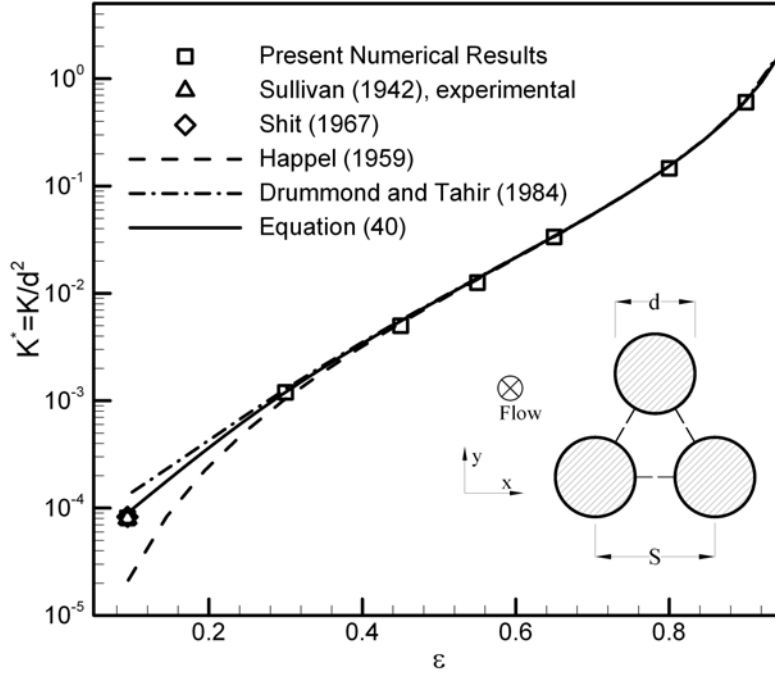
Figure 23: Comparison of the proposed model, an experimental data point (touching limit), and other existing models, staggered arrangement.

The present analytical solution, present numerical results, the models of Happel [28] and Drummond and Tahir [32] for hexagonal arrangement are compared in Figure 24. The proposed relationship for permeability of hexagonal arrays captures the numerical results within maximum difference of 9%.

The relationships for dimensionless permeability of various arrangements, given in Eq. (40), are very similar to each other and the differences are in the constants and the higher order terms. The higher order terms become negligible for highly porous structures, i.e., $\varepsilon \rightarrow 1$. Therefore, it is expectable that the three equations lead to almost identical values in this limit. As shown in Figure 25, for $\varepsilon > 0.85$ the difference between the models is less than 5%; therefore, the permeability can be considered to be independent of microstructure. For lower porosities, on the other hand, the effect of higher order terms is considerable and the staggered array has the lowest permeability

while the hexagonal arrangement is the most permeable microstructure. This is in-line with our previous observations for fully-developed flow through channels with regular polygonal cross sections [126].
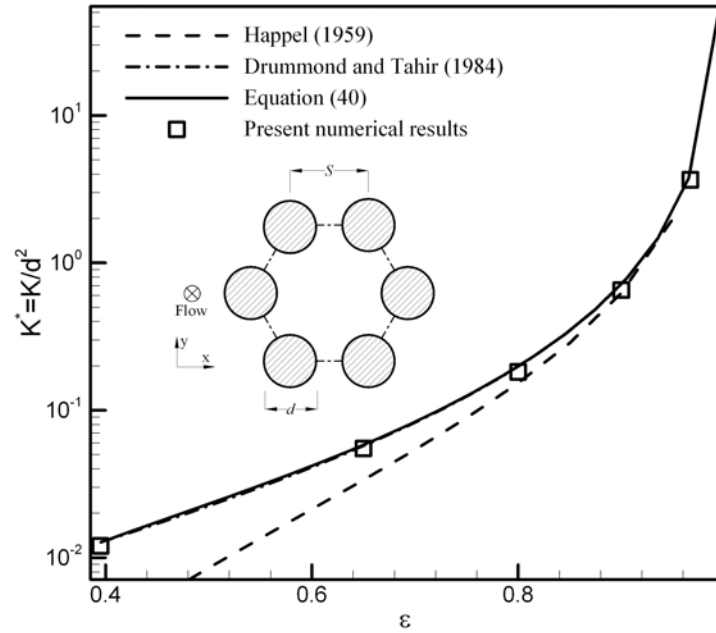
Figure 24: Comparison of the proposed model with other existing models, hexagonal arrangement.
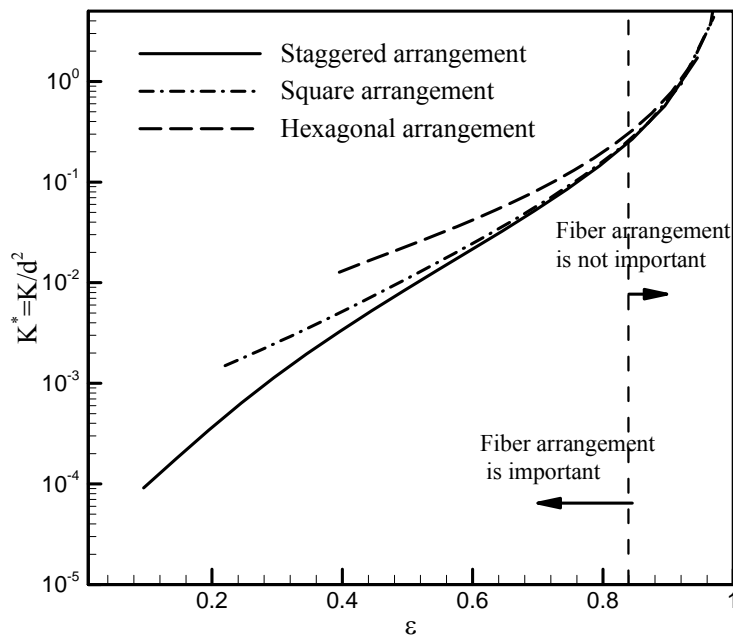
Figure 25: Effect of cell arrangement on the parallel permeability of ordered arrays of fibers.

3.4 Blending methods for permeability of complex fibrous media

As discussed in Section 2.1.3, blending methods have been successfully used for modeling the permeability of mixtures formed by various fibers with different transport properties. In this Section, blending methods are used to predict the in-plane permeability of 2D and 3D structures.

3.4.1 In-plane permeability of GDLs (2D materials)

There are different types of GDLs including carbon paper type, carbon fiber cloth, and wet-/dry-laid papers [51]. The carbon paper type is the focus of the present study. An SEM image of Toray carbon paper is shown in Figure 26. Gas permeability of such fibrous structures depends on several factors including: porosity, fibers size and distribution. In carbon papers, the axes of fibers are located on parallel planes with random distribution and orientation, see Figure 26. Therefore, the geometry shown in Figure 27 can be assumed as an idealized representation of the GDLs. The porosity of the ordered structure is related to the distance between the centers of adjacent fibers, S, and the fibers diameter d:
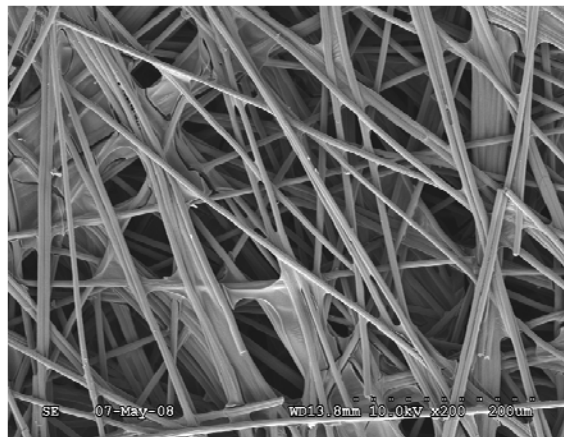
Figure 26: SEM image of Toray 90 carbon paper used as GDL in PEMFCs.
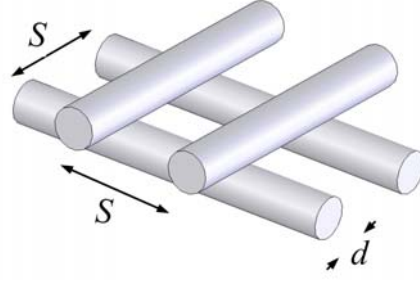
Figure 27: Proposed periodic geometry used for modeling GDLs (2D structures).

$$\varepsilon = 1 - \frac{\pi d^2 / 4}{S d} = 1 - \frac{\pi d}{4 S} \tag{41}$$

Following Jackson and James [54], carbon paper is modeled as a mixture of fibers parallel and normal to flow direction with solid volume fractions of φ_{par} and φ_{norm}, respectively; for the geometry shown in Figure 27, $\varphi_{par} = \varphi_{norm} = \varphi_{tot} / 2$. It is expected that the equivalent permeability, $K_{eq}(\varphi)$, is related to the permeability of each component; the concept of blending technique is shown in Figure 28.

It should be noted that there are no concrete rules for estimating the mixtures permeability. Blending techniques have been successfully employed to estimate the permeability of fibrous mixtures such as hydrogels [54], fibers with different sizes [41], and fibers with different charges [55, 56]. However, to our best knowledge, the application of blending techniques to planar structures such as GDL is novel.

Several blending rules, originally developed for different applications, are rewritten for a mixture of carbon fibers with different orientations and are listed in Table 6. The volume-weighted resistivity scheme assumes that the two fiber categories act similar to flow resistors in series, while the volume weighted permeability model

considers each fiber category as parallel flow resistors [24]. The geometric mean scheme is a purely mathematical blend. To estimate the mixture permeability from using the equations listed in Table 6, one needs to know the permeability of the fibers in both normal and parallel directions.
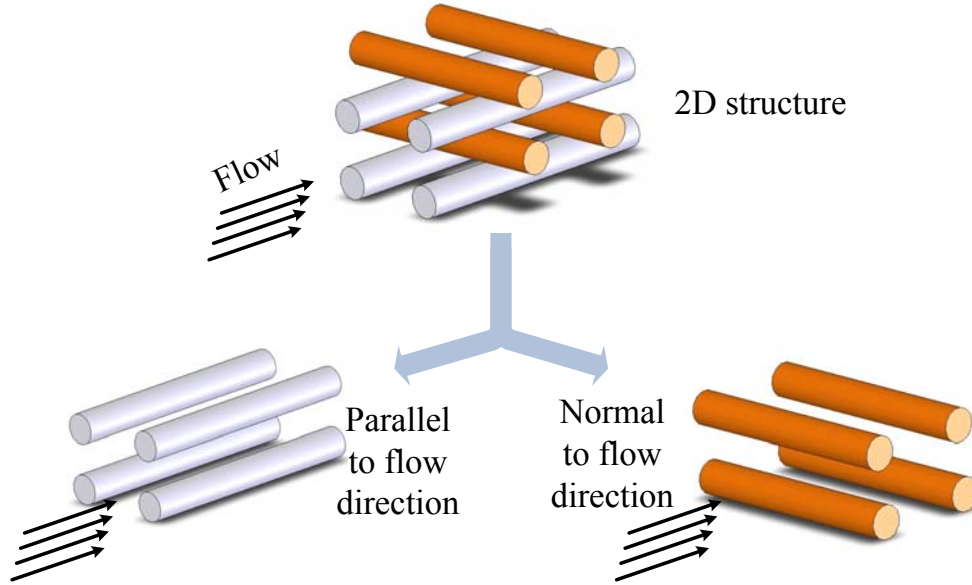
Figure 28: The blending technique concept for GDLs (2D structures).

Table 6: A summary of various blending methods investigated for estimation of in-plane permeability.

Blending model	Relationship
Volume-weighted resistivity	$\dfrac{1}{K_{eq}(\varphi)} = \dfrac{\varphi_{par}}{\varphi}\dfrac{1}{K_{par}(\varphi)} + \dfrac{\varphi_{norm}}{\varphi}\dfrac{1}{K_{norm}(\varphi)}$ [1]
Unweighted resistivity	$\dfrac{1}{K_{eq}(\varphi)} = \dfrac{1}{K_{par}(\varphi_{par})} + \dfrac{1}{K_{norm}(\varphi_{norm})}$
Volume weighted permeability	$K_{eq}(\varphi) = \dfrac{\varphi_{par}}{\varphi} K_{par}(\varphi) + \dfrac{\varphi_{norm}}{\varphi} K_{norm}(\varphi)$
Geometric mean	$K_{eq}(\varphi) = \left(K_{par}(\varphi)\right)^{\frac{\varphi_{par}}{\varphi}} \left(K_{norm}(\varphi)\right)^{\frac{\varphi_{norm}}{\varphi}}$

[1] $\varphi = \varphi_{tot}$

The blending models listed in Table 6 combined with normal and parallel permeability presented by Eqs. (23) and (40) are used to calculate the permeability of the geometry shown in Figure 27. In the considered geometry, 50% of fibers are parallel and 50% of fibers are normal to flow direction, i.e., $\varphi_{par} = \varphi_{norm} = \varphi_{tot}/2$. The calculated results from different blending rules are plotted in Figure 29. It can be seen that the blending rules fall between normal and parallel permeability of square arrays of cylinders and at high porosities, $\varepsilon > 0.7$, there is a small difference between different models.

Our analysis showed that the volume-weighted permeability scheme is in better agreement with experimental data in lower porosities, $\varepsilon < 0.7$. This blending model is presented in the following easy-to-use form which is a curve fit of the model:

$$K(\varepsilon, d) = \exp\left(\frac{-12.95 + 13.9\,\varepsilon}{1 + 1.57\,\varepsilon - 2.22\,\varepsilon^2}\right) d^2 \tag{42}$$
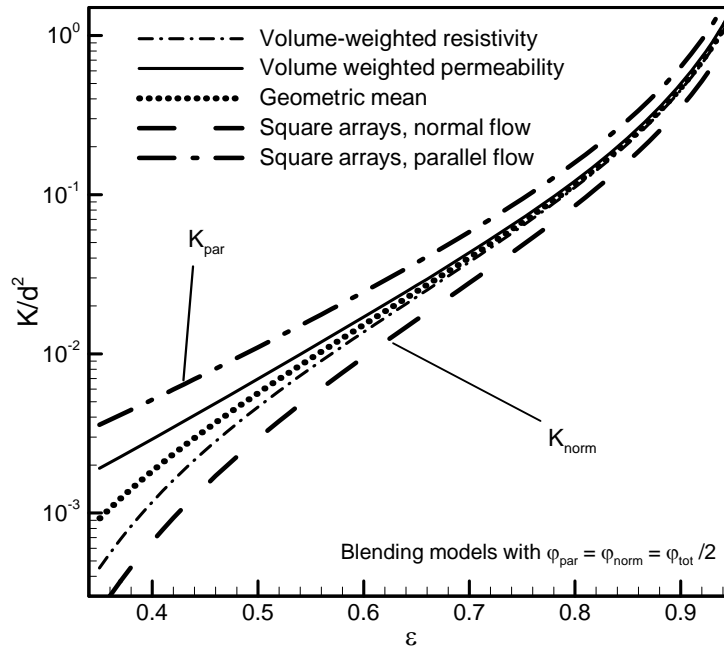
Figure 29: Comparison of different blending models with the bounds for $\varphi_{par} = \varphi_{norm} = \varphi_{tot}/2$.

This relationship is only a function of porosity and fiber diameter. The proposed blending model, Eq. (42), is compared with the experimental results of Gostick et al. [9] and Feser et al. [8] for a variety of carbon paper GDLs in Figure 30. In addition, to cover a wider range for the porosity of experimental data, the experimental results reported by Shi and Lee [70] for composite fabrication application are included. Figure 30 shows that the volume weighted permeability method predicts the trends of experimental data over a wide range of porosity.

Most of the collected experimental data fall between the normal and parallel permeability of the square arrangement of fibers. Therefore, normal and parallel permeability of unidirectional fibers can provide upper and lower bounds for the in-plane gas permeability of fibrous porous media such as GDLs, respectively. In other words, the
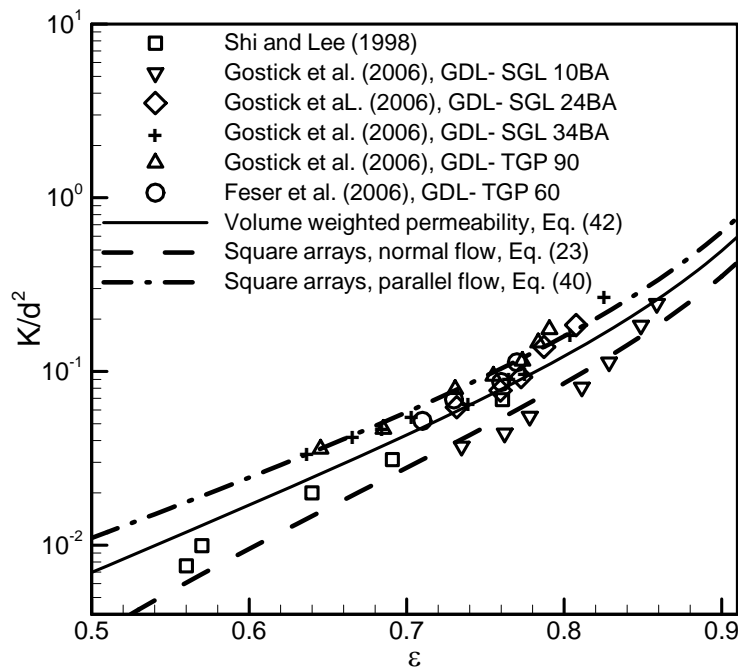
Figure 30: Comparison of the proposed blending model and experimental data.

65

permeability of fibers with mixed orientations is bounded by the two limiting cases when all of the fibers are oriented either parallel or normal to flow direction. This is in line with observations of Tomadakis and Robertson [11] and Tamayol and Bahrami [121].

In Figure 31, the present model, Eq. (42), and the collected experimental data are compared against the correlations reported by Tomadakis and Sotirchos [58] and Van Doormaal and Pharoah [51]. The model of Tomadakis and Sotirchos (TS) [58] was based on the analogy between electrical and flow conductions. This model was originally developed for permeability of randomly distributed overlapping fibers in composite reinforcements [58]. It can be seen that both Eq. (42) and the model of [51] predict the trends of experimental data over the low to medium range of porosity. However, TS model [58] overpredicts the data in high porosities, ε < 0.8, while Eq. (42) is in agreement with the experimental data over the entire range of porosity.
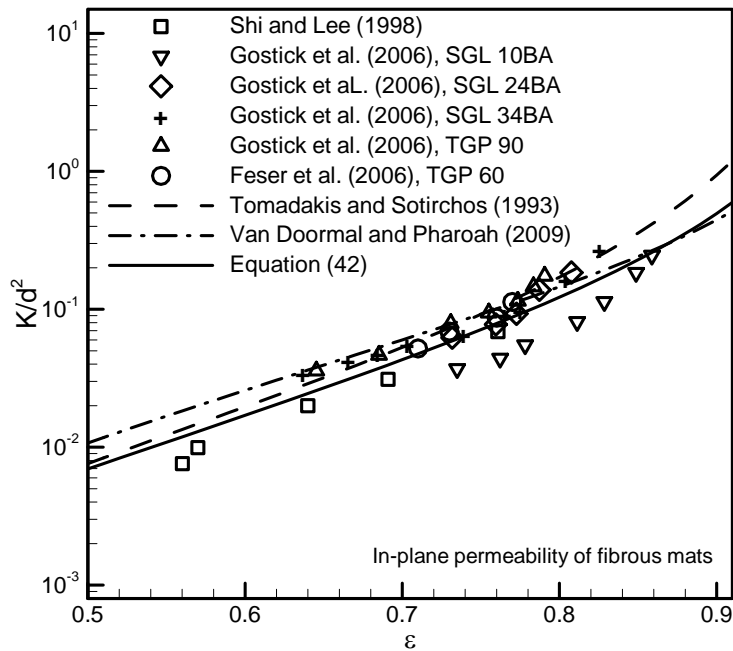
Figure 31: Comparison of present model with other existing correlations for the in-plane permeability of fiber mats.

66

3.4.2 In-plane permeability of 3D fibrous materials

To further investigate the application of blending techniques for estimating permeability of fibrous media with complex but non-planar microstructure, a similar analysis has been conducted for three-directional [11] fibrous structures with random distribution and orientation of fibers in the space. Following Jackson and James [54], the complex geometry is modeled with the simple cubic (SC) arrangement shown in Figure 32. In the SC structure, 1/3 of fibers are parallel and 2/3 of fibers are normal to flow direction, i.e., $\varphi_{par} = \varphi_{tot}/3$, $\varphi_{norm} = 2\varphi_{tot}/3$; see Figure 33. The volume-weighted resistivity scheme is in a reasonable agreement with experimental data and can be written in the following compact form:

$$K(\varepsilon, d) = \exp\left(\frac{-43.25 + 46.6\varepsilon}{1 + 10.56\varepsilon - 10.5\varepsilon^2}\right) d^2 \tag{43}$$

In Figure 34, the proposed relationship, Eq. (43) is compared with experimental data of 3D structures and the models of Tomadakis and Sotirchos [58] and Jackson and James [54]. It can be observed that Eq. (43) accurately captures the trends of experimental and numerical data.
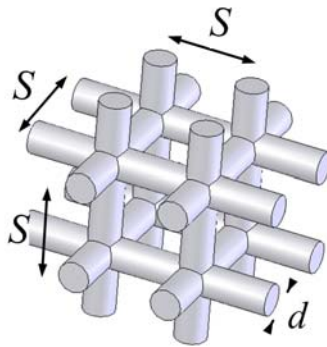
Figure 32: Proposed Simple cubic arrangement for modeling 3D (non-planar) fibrous structures.

67
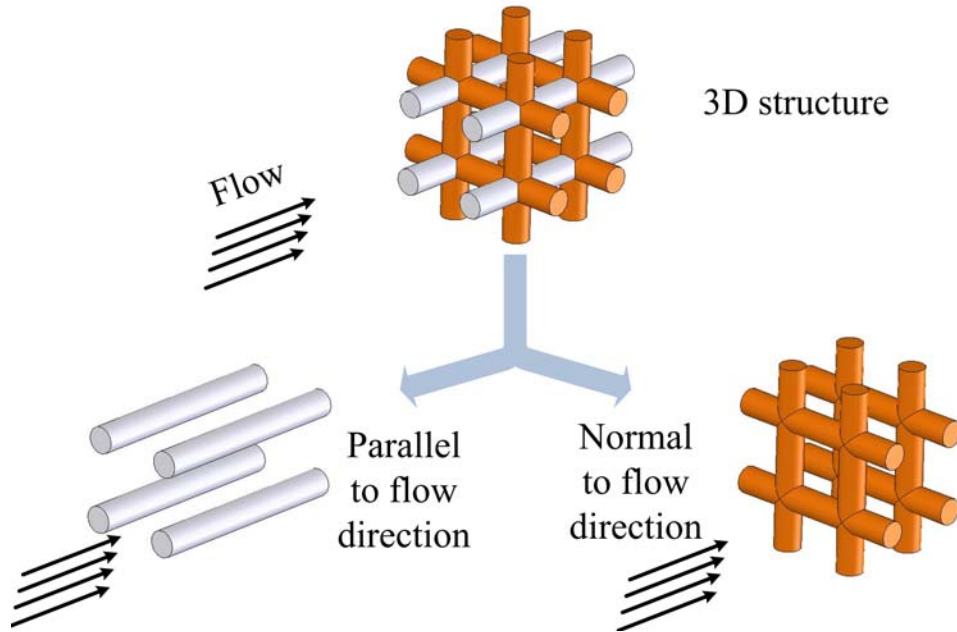
Figure 33: The blending technique concept for 3D fibrous structures.
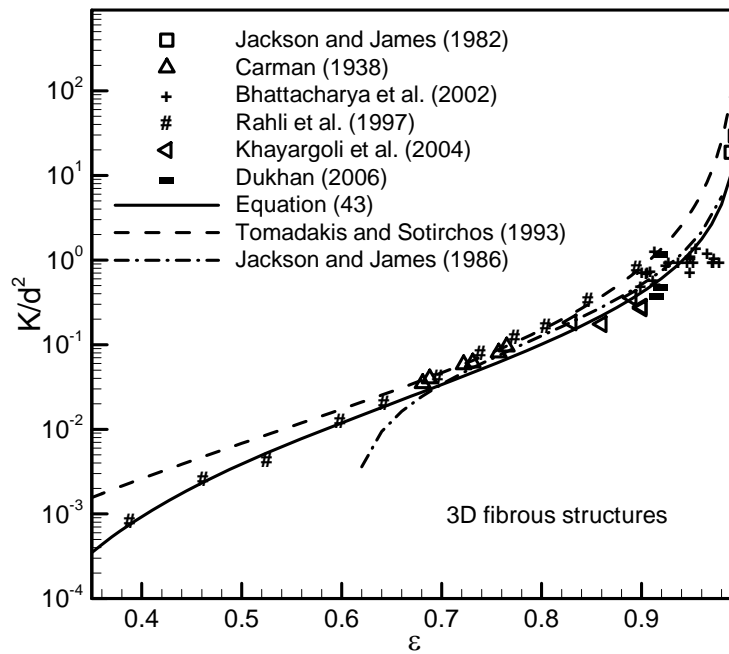
Figure 34: Comparison of present model with other existing correlation for 3D structures.

3.5 Transverse permeability of fibrous media: An scale analysis approach

In this section transverse permeability of various 1D, 2D, or 3D fibrous structures is evaluated using a scale analysis approach. The simplest representation of 1D structures or generally fibrous media is the ordered arrangements of unidirectionally aligned cylinders. In the present study, several ordered structures including square, staggered, and hexagonal arrays of fibers are considered where flow is normal to the fibers axes, see Figure 35.

To study woven or textile structures with non-overlapping fibers, the geometry shown in Figure 36 is considered where fluid flow is normal to the fibers planes. In 3D structures such as metalfoams, fibers can have any arbitrary orientation in space, see Figure 37a. Following Jackson and James [54], the microstructure of 3D fibrous materials is modeled by a simple cubic (SC) arrangement. Figure 37b shows a SC structure used to model 3D media in the present study and the transverse flow direction.
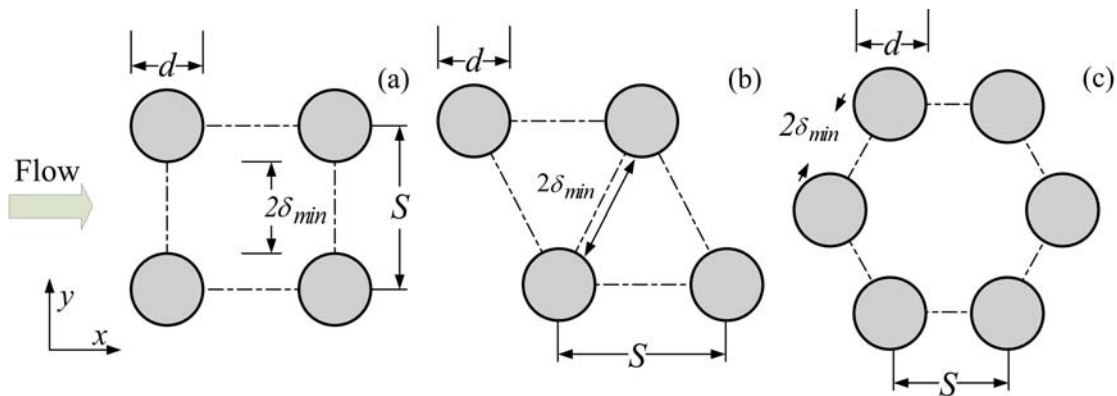
Figure 35: Considered unit cells for ordered 1D structures: a) square, b) staggered, and c) hexagonal arrays of cylinders.
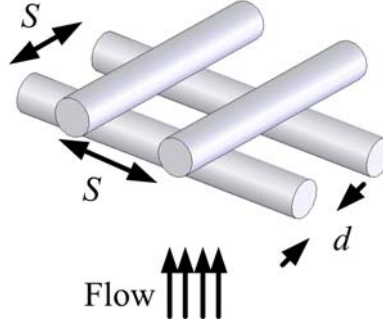
Figure 36: The 2D unit cell considered in the present study.

Permeability should be calculated through pore-level analysis of flow in the solid matrix. In the creeping regime, the pore-scale velocity, $\vec{V}$, is governed by the continuity and Stokes equations:

$$\nabla \cdot \vec{V} = 0 \tag{44}$$

$$\mu \nabla^2 \vec{V} = -\nabla P \tag{45}$$

A scale analysis is followed for determining the resulting pressure drop. In this approach, the scale or the range of variation of the parameters involved is substituted in the governing equations, i.e., derivatives are approximated with differences [127]. Following Clauge et al. [42] and Sobera and Kleijn [37], half of the minimum opening between two adjacent cylinders, δ_{min}, is selected as the characteristic length scale over which rapid changes of velocity occurs, see Figure 35. Therefore, Eq. (45) scales as:

$$-\frac{\Delta P}{\ell} \sim \frac{\mu}{\delta_{min}^2} |\vec{V}| \tag{46}$$

70
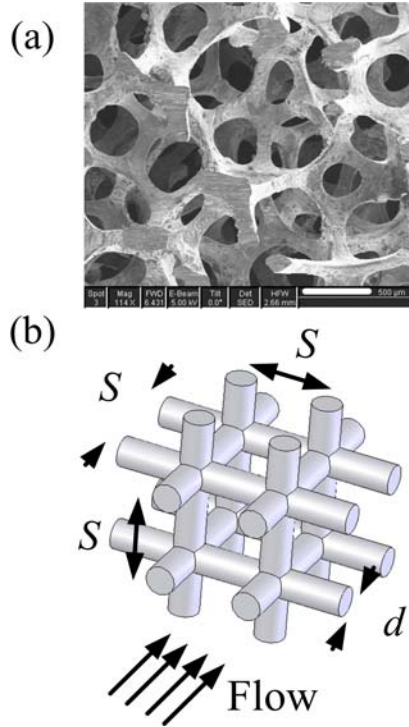
Figure 37: 3D structures; a) metalfoam, a real structure (scale bar is equal to 500 μm); b) simple cubic arrangement, modeled unit cell used in the present analysis.

where ℓ is the characteristic length scale in the flow direction, see [37] for more details. In case of non-touching cylinders with their axes perpendicular to the flow direction the maximum velocity occurs in the section with minimum frontal area. Sobera and Klein [37] proposed to use the average velocity in the section with minimum frontal area as the characteristic velocity scale, i.e., $\left|\vec{V}\right| \sim U_D / \beta$; where β was the ratio of the minimum to the total frontal areas in the unit cell. However, this assumption was only accurate for highly porous structures, $\varepsilon > 0.8$, and overpredicted the pressure drop in low porosities [37]. Carman [22] argued that a fluid particle should travel in a tortuous path of length L_e to pass through a sample of size L. Therefore, it is expected that the resulting

velocity scale for a constant pressure drop be inversely related to L_e / L; this ratio is called the tortuosity factor, τ. Thus, the scale of the pore-level velocity magnitude becomes:

$$\left| \vec{V} \right| \sim \frac{U_D}{\tau \beta} \qquad (47)$$

Substituting from Eq. (47) for velocity scale and using $\delta_{\min}$ as the length scale, permeability can be calculated as:

$$K = C \beta \delta_{\min}^2 \tau \qquad (48)$$

where C is a constant that should be determined through comparison with data. Therefore one needs to know the ratio between the minimum to total frontal area, β, and the tortuosity factor, τ, to be able to calculate the permeability.

3.5.1   Tortuosity factor

The tortuosity factor is defined as the ratio of the average distance, L_e, that a particle should travel in a sample of size L. Due to its importance in mass, thermal and electrical diffusion, several theoretical and empirical relationship have been proposed for calculating the tortuosity in the literature; good reviews can be found elsewhere [128, 129]. Any relationship proposed for tortuosity should satisfy three conditions [128, 129]: $\tau > 1$; $\lim_{\varepsilon \to 1} \tau = 1$; $\lim_{\varepsilon \to 0} \tau \to \infty$. One of the most popular empirical relationships for determination of tortuosity, that satisfies all these conditions, is the Archie's law [130]:

$$\tau = \left(\frac{1}{\varepsilon}\right)^{\alpha} = \left(\frac{1}{1-\varphi}\right)^{\alpha} \qquad\qquad (49)$$

where α is a constant and ε is the porosity. α is a 'tuning' parameter that is found through comparison of the Archie's empirical correlation, i.e., Eq. (49), with experimental data. Boudreau [125], through comparison with data, showed that $\alpha = 0.5$ provides a reasonable estimate for tortuosity in packed beds. The axes of fibers in 1D and 2D micro-structures are perpendicular to the transverse flow direction which is similar to the flow through packed beds of spherical particles. As a result, $\alpha = 0.5$ provides a good estimate for the tortuosity of 1D and 2D structures as well. However; in 3D structures, some of the fibers (roughly 1/3, consider an equally-spaced equally-sized cubic unit cell) are parallel to the flow direction and do not affect the tortuosity of the medium. The study of Tomadakis and Sotirchos [58] also showed that 3D fibrous structures are less tortuous in comparison with 1D and 2D matrices. Consequently, an α smaller than 0.5 should be used for 3D microstructures. The deviation of Archie's law with $\alpha = 0.3$ from the tortuosity values predicted by the model of Tomadakis and Sotirchos [58] is less than 20%. In the present study, our model for permeability of 3D structures ($\alpha = 0.3$) captures the trends of the present experimental results and the data collected from various sources.

3.5.2 Experimental study

Experimental data for creeping flow through fibrous structures that we are interested in is not abundant in the open literature. As such, several samples of tube banks with 1D square and staggered fiber arrangements and metalfoams with 3D microstructures shown in Figure 38 are tested using glycerol. To fabricate the tube bank

73

sample, Polymethyl methacrylate (PMMA) sheets of 3 *mm* thickness were cut and drilled using a laser cutter with the accuracy of 0.05 *mm*. Glass capillary tubes with diameter of 1.5 *mm* were inserted and fixed using an adhesive tape to form tube banks, as shown in Figure 38. The length of the tube banks were selected such that a minimum of 15 rows of cylinders existed in the flow direction for each sample. Aluminum 6101 metalfoam samples were purchased from ERG Duocel (Oakland, CA) with a number of pores per inch (PPI) in the range of 10 to 40. The porosity of the samples was also calculated independently by weighting the samples and measuring their volumes. In this case, the density of the fibers was reported by manufacturer as 2690 *kg/m³* and the solid volume fraction was calculated as $\varphi = \text{mass} / (2690 \times \text{volume})$. The fiber diameters were estimated using SEM images and also compared with the data reported by others [131] for similar materials. The properties of the samples are summarized in Table 7.

A custom-made gravity driven test bed, illustrated in Figure 38, was built that included an elevated reservoir, an entry section, sample holder section, and an exit section with a ball valve. The reservoir cross-section of 300×300 *mm²* was large enough to ensure that the variation of the pressure head was negligible during the experiment. The pressure drop across the samples was measured using a differential pressure transducer, PX-154 (BEC Controls) with 1% accuracy. To minimize entrance and exit effects on the pressure drop measurements, pressure taps were located few rows apart (at least three rows) from the first and the last tube rows in the tube bank samples and 1 *cm* apart from the sample edge for metalfoams. Glycerol was used as the testing fluid and the bulk flow was calculated by weighting the collected test fluid over a period of time.

The Reynolds number was defined based on fibers diameter, i.e., $\mathrm{Re} = \rho\, U_D\, d\, /\, \mu$, and was kept below 0.001 to ensure creeping flow regime in the tested media. As such, the permeability of the samples was calculated using the Darcy equation, Eq. (1).

Assuming Darcy's law in a porous structure implies a linear relationship between the pressure drop and the fluid velocity in the media. This linear relationship can be observed in Figure 39 for tube banks with square and staggered fiber arrangements and metalfoam samples.

Table 7: The properties of the tested samples.

Sample type	ε	$d\,(mm)$	$L(mm)$	Orientation	Measured permeability, $K\,,(m^2)$
Tube bank (square)	0.8	1.5	59	1D	1.38×10^{-7}
Tube bank (square)	0.85	1.5	68	1D	3.74×10^{-7}
Tube bank (square)	0.9	1.5	80	1D	5.44×10^{-7}
Tube bank (staggered)	0.7	1.5	74	1D	1.00×10^{-7}
Tube bank (staggered)	0.9	1.5	72	1D	7.75×10^{-7}
Metalfoam (PPI=10)	0.93	0.4	137	3D	2.53×10^{-7}
Metalfoam (PPI=20)	0.93	0.3	135	3D	1.45×10^{-7}
Metalfoam (PPI=40)	0.94	0.2	120	3D	0.81×10^{-7}

3.5.3 Results and discussion

Equation (48) relates the permeability of fibrous media to the minimum opening between adjacent fibers, $\delta_{\min}$, the ratio between minimum to total frontal area, β, and tortuosity factor, τ, that can be calculated from Eq. (49). In the following subsections, using geometrical properties of the considered microstructures, compact models will be developed that relate the permeability to the solid volume fraction.

3.5.3.1 Unidirectionally Aligned Arrangements

For the three different ordered 1D unit cells shown in Figure 35, it can be seen that $\beta = (S-d)/S$ and $\delta_{\min} = (S-d)/2$. Therefore, Eq. (48) can be rewritten as:

$$K = C\frac{(S-d)^3}{S\sqrt{1-\varphi}} \tag{50}$$

Combining Eqs. (28) and (50), the dimensionless permeability of the ordered structures becomes:

$$\frac{K}{d^2} = \begin{cases} \dfrac{0.16\left[\dfrac{\pi}{4\varphi} - 3\sqrt{\dfrac{\pi}{4\varphi}} + 3 - \sqrt{\dfrac{4\varphi}{\pi}}\right]}{\sqrt{1-\varphi}} & \text{Square} \\[4ex] \dfrac{0.16\left[\dfrac{\pi}{2\sqrt{3}\varphi} - 3\sqrt{\dfrac{\pi}{2\sqrt{3}\varphi}} + 3 - \sqrt{\dfrac{2\sqrt{3}\varphi}{\pi}}\right]}{\sqrt{1-\varphi}} & \text{Staggered} \\[4ex] \dfrac{0.16\left[\dfrac{\pi}{3\sqrt{3}\varphi} - 3\sqrt{\dfrac{\pi}{3\sqrt{3}\varphi}} + 3 - \sqrt{\dfrac{3\sqrt{3}\varphi}{\pi}}\right]}{\sqrt{1-\varphi}} & \text{Hexagonal} \end{cases} \tag{51}$$
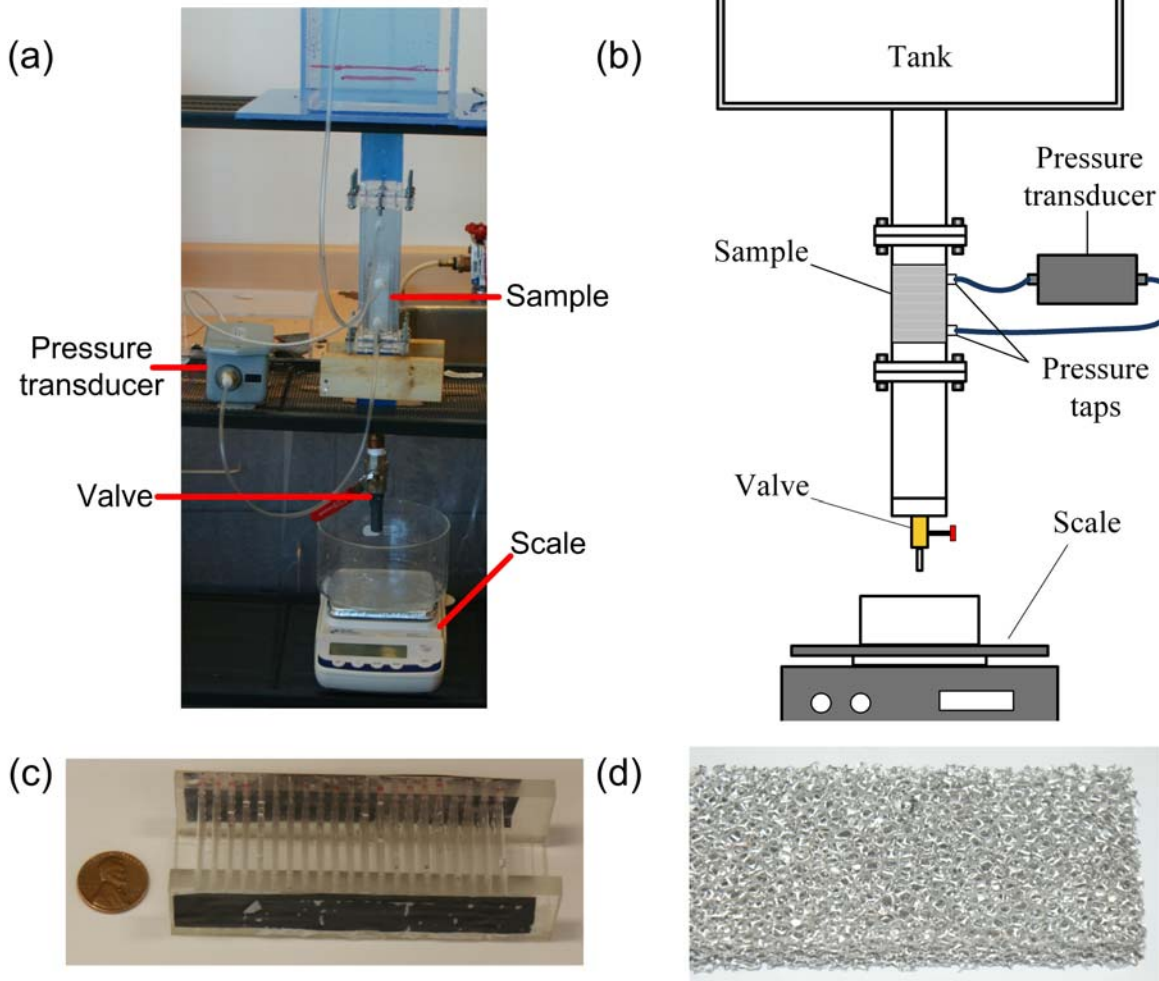
Figure 38: The gravity driven test bed and the tested samples: a) actual test setup, b) schematic, c) a sample of tube banks, and d) a sample of aluminum foam.

The constant values in Eq. (51) are evaluated through comparison of the proposed model with the experimental and numerical data found in the literature. In Figure 40, Eq. (51) is compared with the present experimental results and the data collected by others. As one can see, the model is in agreement with experimental data over the entire range of porosity. These experiments were conducted using different fluids including: air, water, oil, and glycerol with a variety of porous materials.
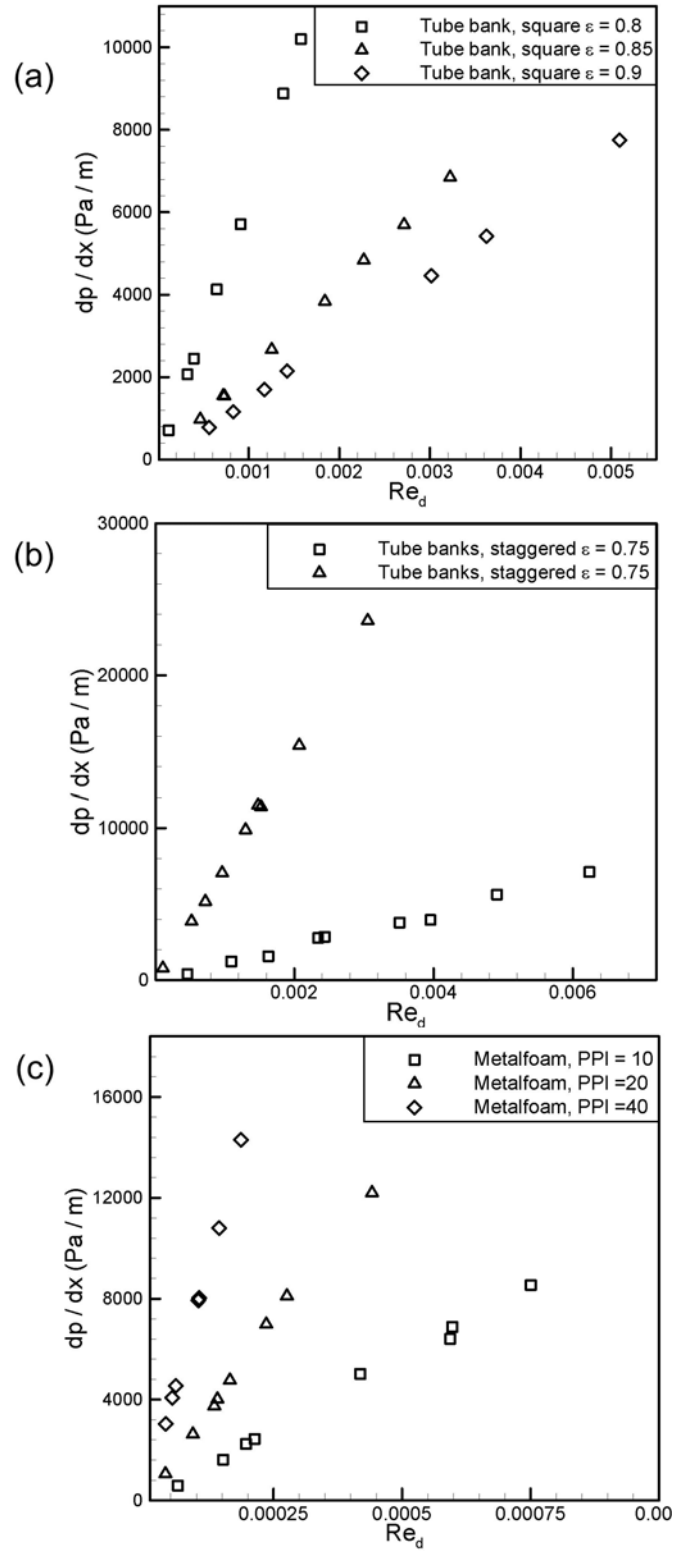
Figure 39: measured pressure gradients for samples of a) tube bank with square fiber arrangement, b) tube bank with staggered fiber arrays, and c) metalfoams.

In Figure 41, the predicted results of Eq. (51) for staggered arrangement of fibers are compared with present experimental data and numerical results of Higdon and Ford [40]. It can be seen that the proposed model can accurately predict the numerical results in the entire range of porosity. The average relative differences between the numerical and experimental data with the values predicted by various models for 1D structures are reported in Table 8.
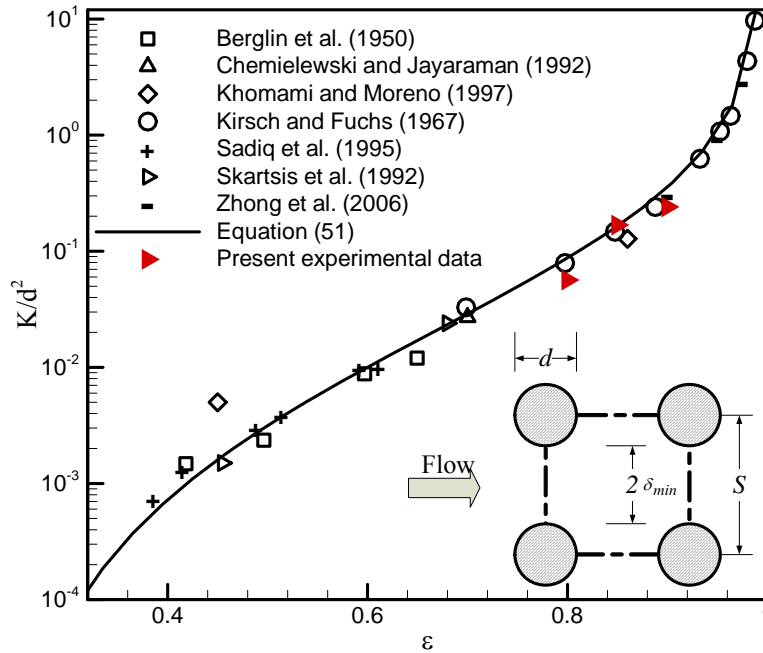
Figure 40 : Comparison of the proposed model for square arrangements with experimental data measured in the present study or reported by others.
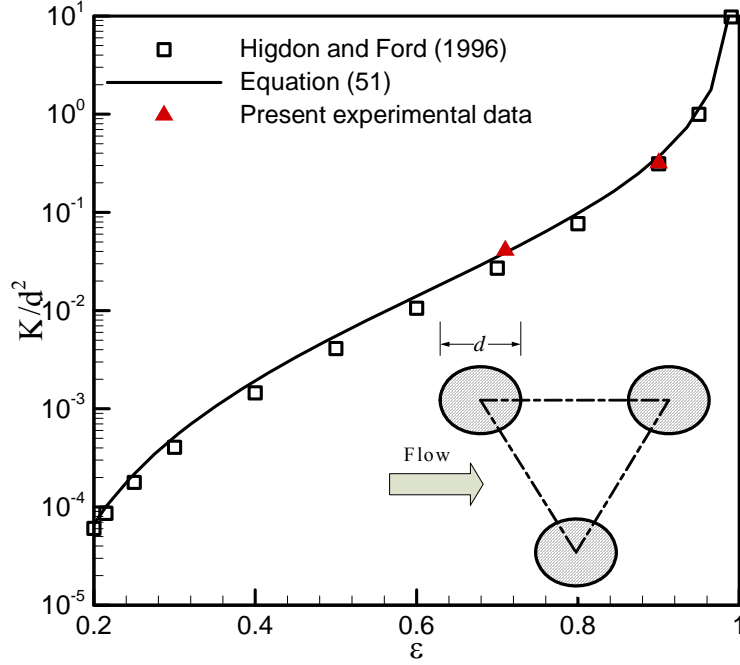
Figure 41: Comparison of the proposed model and current experimental data with numerical results of Higdon and Ford [40] for staggered arrangements.

3.5.3.2 Two-directional structures

The ratio of the minimum frontal to the total unit cell areas for the 2D structure, shown in Figure 36, is not exactly known. Therefore, using the Forchheimer law that estimates the average pore-scale velocity as U_D / ε [1], the magnitude of the pore-level velocity scale is estimated as:

$$\left| \vec{V} \right| \approx \frac{U_D}{\tau \, \varepsilon} \tag{52}$$

The length scale, where the rapid changes of the velocity occurs, is assumed as $\delta_{\min} = (S - d)/2$. Therefore, the permeability reads:

Table 8: The average relative difference between the permeability values predicted by different models with the numerical and experimental data for 1D square, 1D staggered, and 3D simple cubic structures over the entire range of porosity.[1]

1D square arrays (compared to experimental data)			
Author(s)	Relative difference (%)	Author(s)	Relative difference (%)
Equation (23)	24.9	Happel (1959)	47.5
Gebart (1992)	26.8	Drummond and Tahir (1984)	245.2
Van der Westhuizen (1996)	45.8	Equation (51)	15.8
Sahraoui and Kaviany (1994)	25.6		
1D staggered arrays (compared to present experimental data and numerical results of Higdon and Ford [40])			
Author(s)	Relative difference (%)	Author(s)	Relative difference (%)
Gebart (1992)	11.6	Equation (51)	26.6
Happel (1959)	38.8		
3D simple cubic structure (Compared to numerical results of Higdon and Ford [40])			
Author(s)	Relative difference (%)	Author(s)	Relative difference (%)
Tomadakis and Robertson (2005)	24.9	Equation (55)	19.3
Jackson and James (1986)	247.3		

[1] Relative difference = $|\text{model} - \text{data}|/\text{model}$

$$K = C(S - d)^2 \varepsilon\tau \tag{53}$$

Substituting for geometrical parameters from Eq. (41) and the tortuosity from Archie's law, the dimensionless permeability becomes:

$$\frac{K}{d^2} = 0.008 \sqrt{(1-\varphi)}\left[\left(\frac{\pi}{4\varphi}\right)^2 - 2\frac{\pi}{4\varphi} + 1\right] \tag{54}$$

The constant value in Eq. (54), i.e., 0.008, is found through comparison with experimental data collected from different sources, see Figure 42. It can be seen that Eq. (54) captures the trend of the experimental data collected from different sources over a wide range of porosity. The experiments were conducted on glass rods, glass wool, cotton wool, kapok with application in filtration [62], alloy fibers [64], fiber reinforcing mats with application in molding and composite fabrication [48, 132], and gas diffusion layers [9]. Kostornov and Shevchuk [64] performed experiments with several fluids and they observed that permeability was dependent on the working fluid, i.e., water resulted in higher permeability than alcohol. Models of Tomadakis and Robertson [11] and Van Doormaal and Pharoah [51] are also compared with Eq. (54) in Figure 42. For highly porous materials ($\varepsilon > 0.8$) the correlation proposed by Van Doormaal and Pharoah [51] also accurately predict the experimental data while the model of Tomadakis and Robertson [11] captures the trends of experimental data in lower porosities.

3.5.3.1 Three-directional structures

For simple cubic arrangement that is considered in this study as a simple representation of 3D fibrous materials, the ratio of the minimum frontal to the unit cell areas is $\beta = (S-d)^2/S^2$ and $\delta_{\min} = (S-d)/2$. Therefore, the permeability of 3D structures becomes:

82
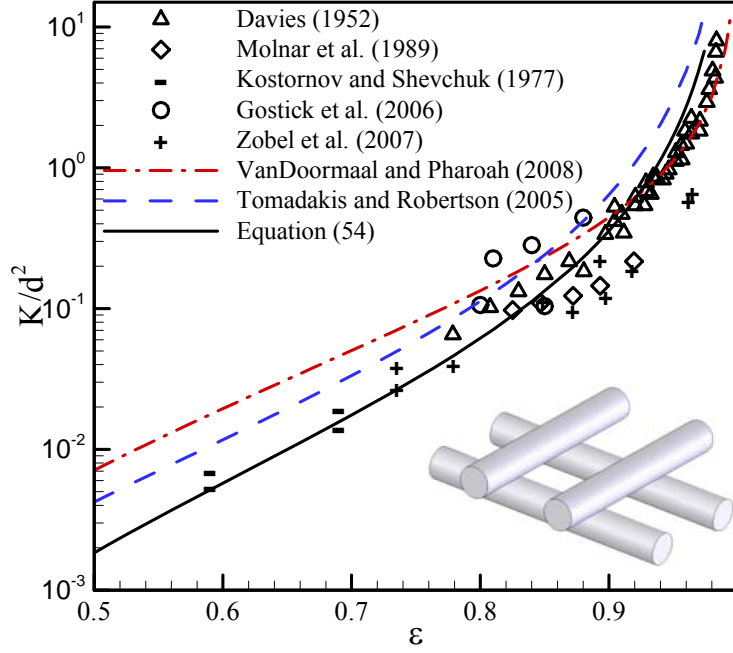
Figure 42: Comparison of the present model, models of Van Doormaal and Pharoah [51] and Tomadakis and Robertson [11] with experimental data for transverse permeability of 2D structures.

$$\frac{K}{d^2} = 0.08 \frac{(S-d)^4}{S^2 d^2 \varepsilon^{0.3}} \tag{55}$$

where the relationship between geometrical parameters of SC structure is:

$$\varphi = \frac{3\pi d^2}{4 S^2} - \sqrt{2} \frac{d^3}{S^3} \tag{56}$$

The constant in Eq. (55) is found to be 0.08 through comparison of this equation with the numerical data reported by Higdon and Ford [40] for SC arrangements over a wide range of porosity. Figure 43 includes the present model, models of Tomadakis and Robertson [11] and Jackson and James [54], current experimental measurements, and experimental data collected from different sources. The plotted data are based on the permeability values reported for polymer chain in solutions [65], glass wool randomly

83
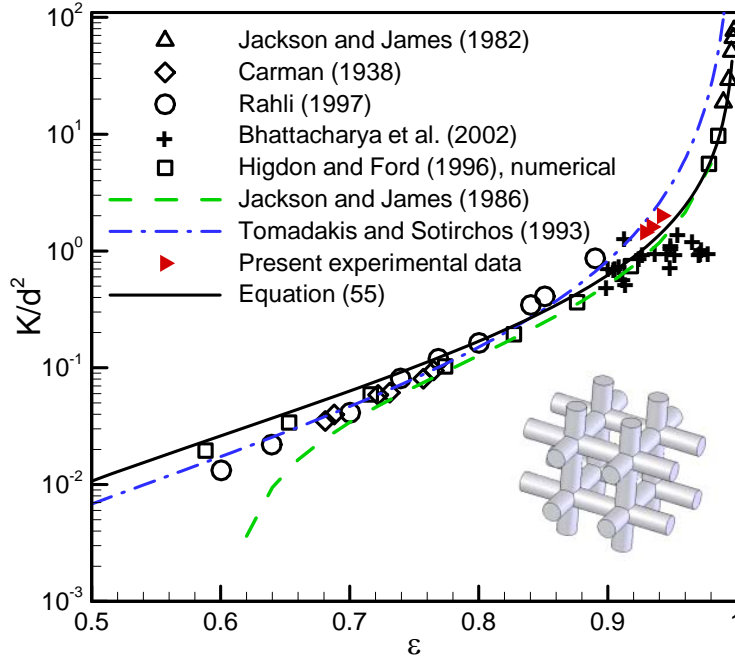
Figure 43: Comparison of the proposed model for 3D structures, models of Jackson and James [54] and Tomadakis and Robertson [11], present experimental results and data reported by others.

packed, stainless steel crimps [22], metallic fibers [69], and aluminum metalfoams [94].

It can be seen that the present model is in agreement with the experimental data and numerical results collected from a number of studies over the entire range of porosity. The average relative differences between the numerical data reported by Higdon and Ford [40] and Eq. (55), the model of Tomadakis and Robertson [11], and the model of Jackson and James [54] are listed in Table 8.

3.6 Through-plane permeability of carbon papers

Through-plane permeability of uncompressed carbon papers with no PTFE treatment can be estimated using the existing models for the permeability of planar fibrous structures. Based on the analogy between electrical and flow conductions, Tomadakis and Robertson [11] developed a model for permeability of randomly

distributed overlapping fibers in composite reinforcements. The scale analysis method and the developed model for 2D fibrous structures, Eq. (54), can also be applied to carbon papers. However, in an actual case, GDL is treated with PTFE and is compressed to manage the water transport and to seal the cell, respectively.

Since the model of [11] and Eq. (54) do not include the effect of PTFE content and mechanical compression on the through-plane permeability, there is a need for developing a general model that can accurately predict the through-plane permeability of GDLs as a function of compression ratio and PTFE content. In addition, more experimental investigations are required to find effects of mechanical compression and PTFE content on the through-plane permeability of GDLS.

3.6.1 Experimental Approach

3.6.1.1 Tested samples

The tested GDLs were purchased as Teflon treated carbon papers from Toray and Sigracet SGL. As a result of their similar production procedure, despite the different thicknesses, TGP-H-90 and 120 have similar microstructures. TGP-H-120 was obtained with 0, 5, 20, and 30% PTFE content while the tested TGP-H-90 have a 0% PTFE content. Figure 44a shows a SEM image of TGP-H-120 with 5% PTFE content. The SGL Sigracet 10AA, shown in Figure 44b, was obtained with 0% PTFE content.

The porosity of the samples which had been reported by manufacturer and Gostick et el. [9] were used in the present study. Fiber diameter was reported by

Table 9: Physical properties of different carbon papers used in the present study: porosity and PTFE content provided by the manufacturers; the measured thicknesses and fiber diameters.

GDL	Thickness (μm)	Porosity[*]	Fiber diameter (μm)	PTFE content (%)
SGL-Sigracet 10AA	390-410	0.88	9.2	0
TGP-H-90	255-270	0.79	9.3	0
TGP-H-120	370-385	0.79	9.3	0-30

[*]The porosity is reported for GDLs with 0% PTFE content.

Gostick et al. [9] and was also independently calculated using scanning electron microscopy (SEM) images. The thickness of the samples was measured using a micrometer; the maximum uncertainty associated with the measurements is less than $10\,\mu m$. The properties of the purchased samples are listed in Table 9.

3.6.1.2 Test apparatus

An air permeability test bed was designed and built for measuring the through-plane permeability, see Figure 45. The high pressure air was supplied by a high pressure air tank and controlled using a digital air pressure regulator; the output pressure of the air regulator valve was set to 6 *psi* during all experiments. Two aluminum blocks were machined and drilled with a 25*mm* diameter hole. The blocks were used as sample holders and the GDL samples were sandwiched between the blocks. An O-ring was used between the two aluminum blocks to prevent air leakage from the test section.
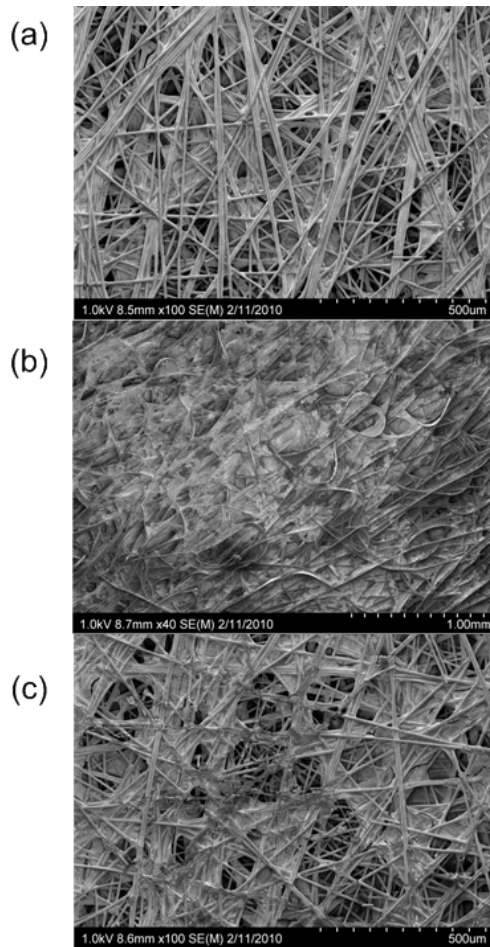
Figure 44: SEM Images: a) TGP 120 with 5% PTFE content; b) SGL Sigracet 10AA; c) compressed TGP 120 with 5% PTFE content.

The up and down stream air flow were connected to a differential pressure transducer, PX277-01D5V, supplied by Omega (Omega Inc., Laval, QC, Canada). The pressure transducer was connected to a PC, using a DAQ purchased from Omega (Omega Inc., Laval, QC, Canada), where the pressure drop values were recorded. The accuracy of the pressure transducer was 1% of its full scale measuring range (0-1 inch of water). The air flow rate passing through the GDLs was measured using a flow meter provided by Omega (Omega Inc., Laval, QC, Canada). The accuracy and the range of the air flow meter was 3% and 0-10 *lpm*, respectively.

The carbon papers were cut into circular samples of 3 cm diameter for the experiments. To investigate the compression effects, GDL samples were compressed using a GUNT WP 300 Universal Material Tester for 15 *min*; the maximum applied compressive force was less than 20 *kN*. The thickness of the compressed samples was measured after the load was released to determine the variation in its thickness, using the same micrometer.

3.6.1.3 Data analysis

Gas permeability, *K*, is defined using Darcy equation:

$$-\frac{\Delta P}{t} = \frac{\mu}{K} U_D \tag{57}$$

where U_D is the volume averaged velocity through porous media, μ is viscosity, ΔP is the pressure drop across the sample, and t is the GDLs thickness. Darcy equation is valid for incompressible, steady, constant properties, single-phase (no-surface tension forces), and low Reynolds number flows.

The Reynolds number based on the fiber diameter, $\mathrm{Re} = \rho\, U_D\, d\, /\, \mu$, was lower than 0.1 in the present study; therefore, the Darcy equation was applicable for analyzing the experimental results. The maximum measured pressure drop across the samples was less than 200 *Pa*. As such, it was assumed that the compressibility effects for such small values of pressure drop can be negligible and the Darcy equation in the form of Eq. (57) was applicable in the present study. U_D was calculated by dividing the volumetric flow rate by the sample cross-sectional area.
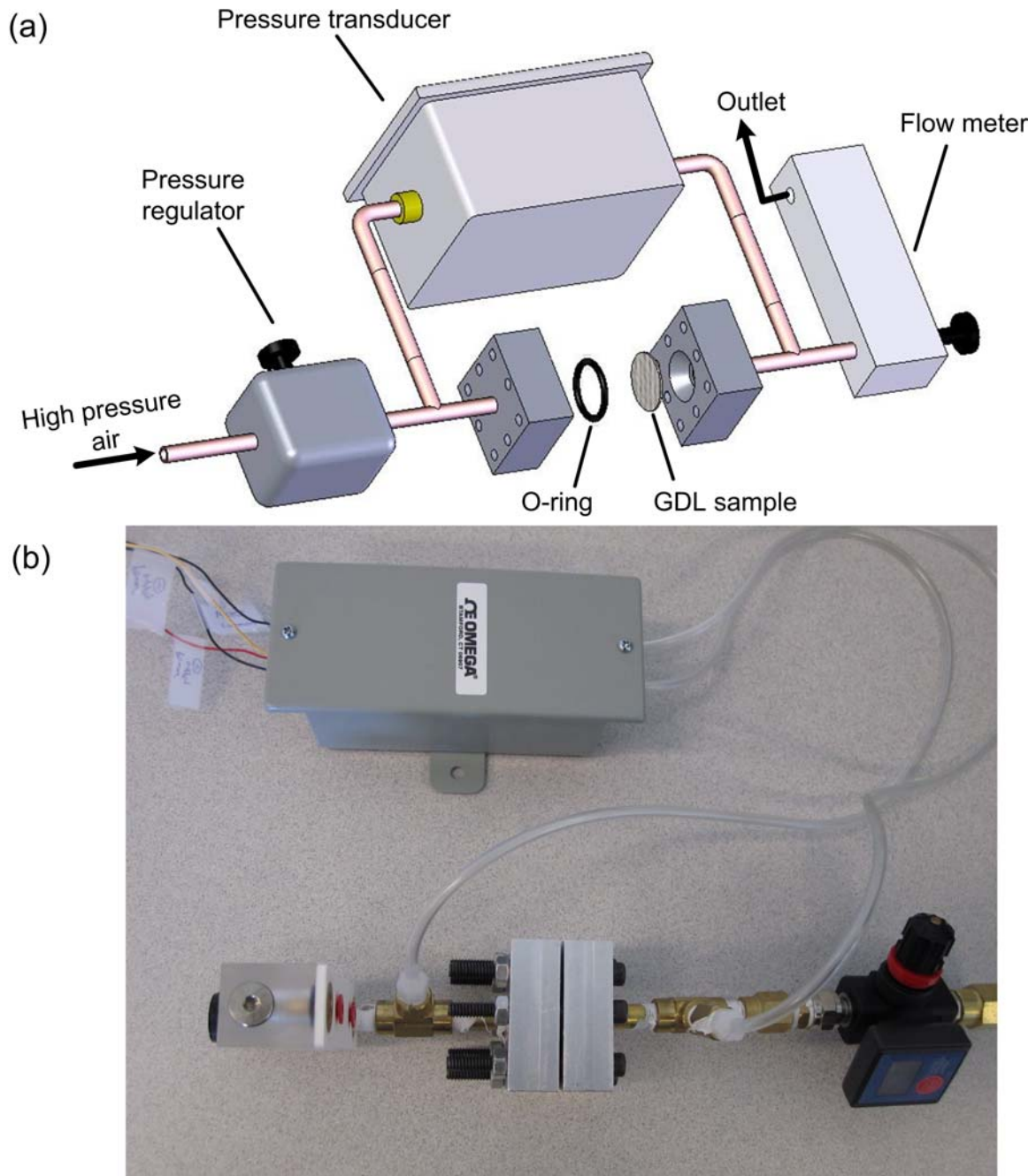
Figure 45: The air permeability test bed: a) schematic of the apparatus (exploded view) b) actual test setup.

Assuming Darcy's law in a porous structure implies a linear relationship between the pressure drop and the fluid velocity in the media. As an example, this linear

relationship can be observed in the experimental results for samples of compressed TGP-H-120 in Figure 46 which justifies Darcy's assumptions.

The measured values of pressure drop, ΔP_{total}, during the experiments were:

$$\Delta P_{total} = \Delta P_{sample} + \Delta P_{min} \tag{58}$$

where ΔP_{sample} is the pressure drop associated with the sample and ΔP_{min} is the pressure drop due to minor losses in the testbed, i.e., exit and entrance section of the sample holder. To account for the minor pressure losses, the pressure drop in the test section was measured once without any GDL samples to determine ΔP_{min} for the entire range of flow rate considered in the present experimental work.
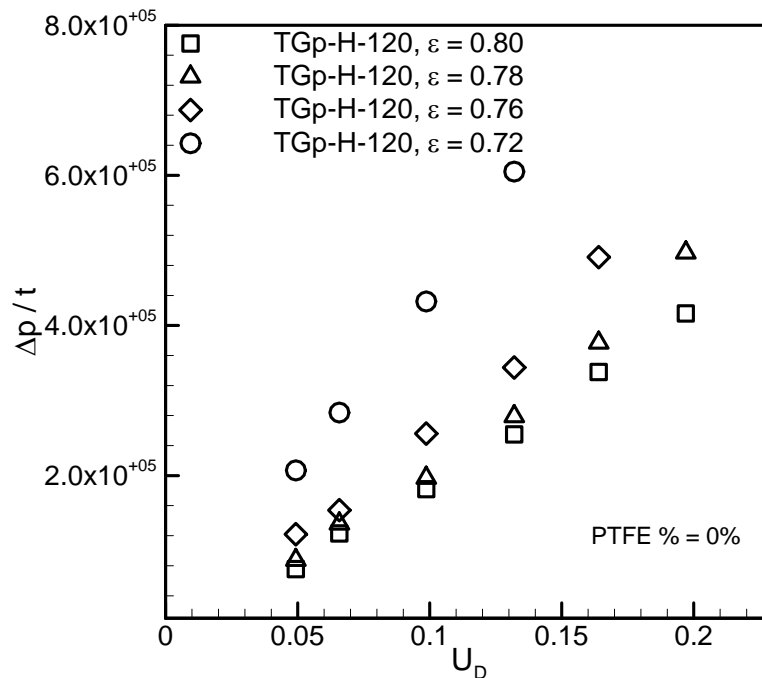
Figure 46: Measured pressure drops for samples of compressed TGP-H-120.

The uncertainty associated with the through-plane permeability, calculated based on the measured variables using the Darcy's equation, can be estimated from[133]:

$$\frac{E(K)}{K} = \sqrt{\left(\frac{E(t)}{t}\right)^2 + \left(\frac{E(\Delta P)}{\Delta P}\right)^2 + \left(\frac{E(U_D)}{U_D}\right)^2} \tag{59}$$

where $E(.)$ is the uncertainty in the measurement of each parameter; these values are listed in Table 10. The maximum uncertainty in the calculated values of permeability is estimated to be 9%.

3.6.2 Theoretical Model

Our scale analysis model, Eq. (54) was successfully compared with experimental data collected from various sources. The tortuosity factor used in derivation of Eq. (54) is based on the Bruggeman equation [134]. Hao and Cheng [49] numerically calculated the tortuosity factor for carbon papers and proposed the following correlation:

$$\tau = 1 + 0.72 \frac{1 - \varepsilon}{(\varepsilon - 0.11)^{0.54}} \tag{60}$$

Table 10: Uncertainty values for measured parameters

Parameter	Uncertainty
δ	10 μm
ΔP	1% of full scale
U_D	3% of full scale
ε	5%
K	9%

Our analysis showed that if the constant value in Eq. (54) is replaced by 0.012 and τ is calculated from Eq. (60) the resulting equation:

$$\frac{K}{d^2} = 0.012(1-\varphi)\left[\left(\frac{\pi}{4\varphi}\right)^2 - 2\frac{\pi}{4\varphi} + 1\right]\left[1 + 0.72\frac{\varphi}{(0.89-\varphi)^{0.54}}\right] \qquad (61)$$

can predict the experimental data for GDLs more accurately. To enable Eq. (61) to include the effects of compression factor and PTFE content, the relationship between these properties and the solid volume fraction should be determined.

Figure 44c shows that mechanical compression does not change the shape of fibers. It can be assumed that during the compression process only the thickness of the original fibrous samples changes while the volume of the solid carbon fiber remains constant. Therefore, the relationship between the solid volume fraction, φ_{comp}, of a compressed sample with the original value for an uncompressed carbon paper, φ_0, can be expressed as [49]:

$$\varphi_{comp} = \varphi_0 \frac{t_0}{t_{comp}} \qquad (62)$$

where t_{comp} and t_0 are the compressed and uncompressed GDL thicknesses, respectively. If the PTFE is added on the carbon paper GDL, the pore volume is randomly filled by the PTFE. It is postulated that PTFE changes the porosity and some pores in the medium are filled. The final porosity, ε_{PTFE}, can be expressed approximately as a function of PTFE content ω [49]:

$$\varepsilon_{PTFE} = \varepsilon_0 - a\frac{\omega\left(1-\varepsilon_0\right)}{1-\omega} \tag{63}$$

where ε_0 is the original porosity before PTFE treatment. Hao and Cheng [49] suggested $a = 0.9$ as the density ratio of the carbon fiber and the PTFE [76]. Employing Eqs. (62) and (63), one can predict effects of PTFE and compression on the permeability on the through-plane permeability of GDLs from the scale analysis technique.

3.6.3 Comparison of experimental and theoretical results

The permeability of various tested samples is calculated using Darcy's law, Eq. (57). The porosity of the compressed samples and GDLs treated with PTFE are calculated using Eq. (62) and (63), respectively.

The effect of mechanical compression and variation of GDL thickness on the permeability is shown in Figure 47. It can be seen that there is a linear relationships between the ratio of compressed to uncompressed permeability of the measured GDLs and the compression ratio, t_{comp}/t_0. The experimental data for the through-plane permeability of compressed GDLs, from the present study or reported by others, are plotted in Figure 48 and compared with the present model, Eq. (61). The comparison of experimental data with the modified TB model shows that proposed model, Eq. (61), captures the trends of experimental data for compressed GDLs. The through-plane permeability of uncompressed TGP-H-90 was measured as $8.7 \times 10^{-8} \ m^2$ which is in good agreement with the value of $8.99 \times 10^{-8} \ m^2$ reported by Gostick et al. [9].
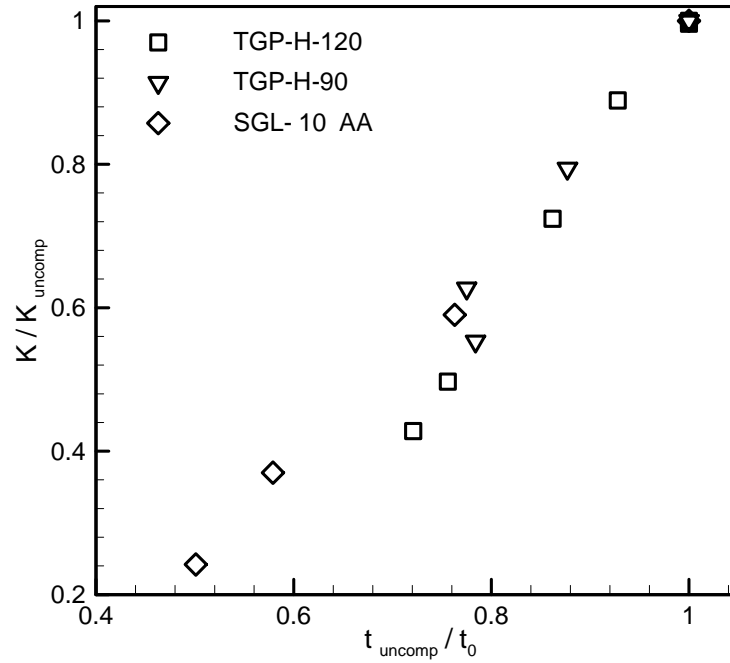
Figure 47: Effect of compression ratio, t_{comp} / t_0 on the variation of permeability.
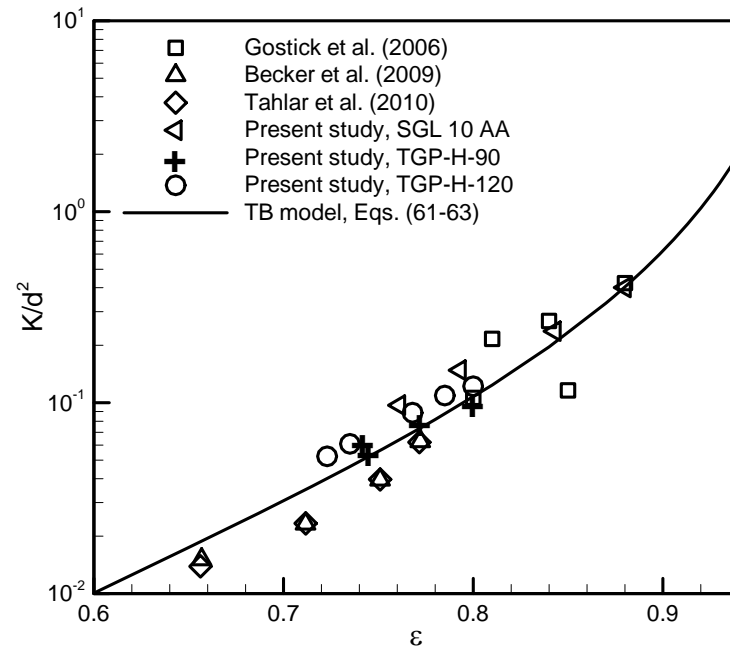
Figure 48: Comparison of the proposed model with the experimental data for compressed GDLs measured in the present study or collected from various sources.

The effect of PTFE content on the through-plane permeability of GDLs is presented in Figure 49. It can be seen that a reverse relationship exist between the PTFE content and the through-plane permeability. The experimental data for TGP-H-120 with various PTFE contents are plotted in Figure 50 and compared with TB model. Porosities of the samples are estimated from Eq. (63). The permeability of the PTFE treated GDLs has a reverse relationship with the PTFE content. It can be seen that Eq. (61) predicts the reverse relationship between permeability and PTFE contents; this is in agreement with the experimental data. Overall, it can be concluded that the modified TB model can be used in design and optimization process of PEMFCs.
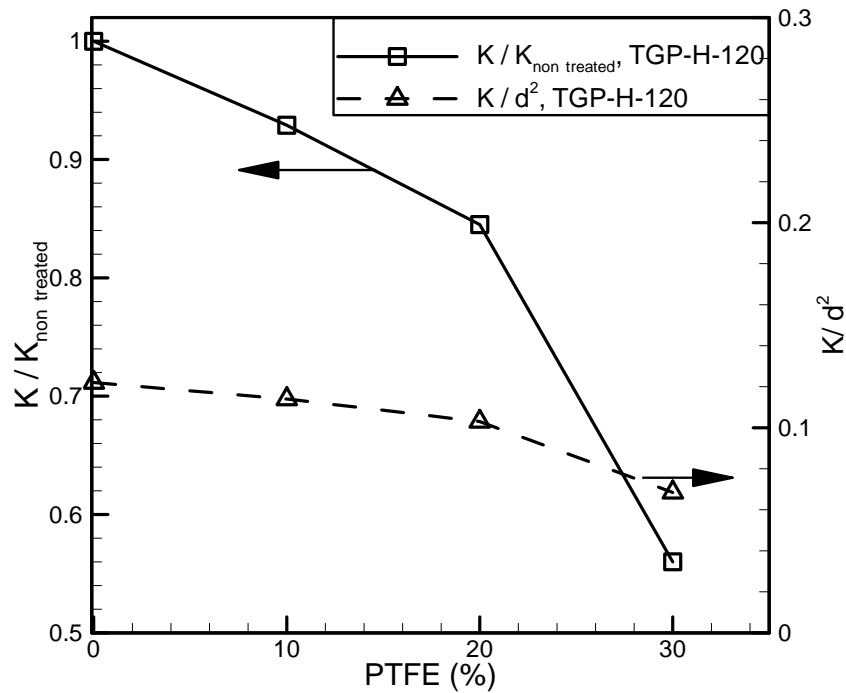
Figure 49: Effect of PTFE content on the through-plane permeability of two set of TGP-H-120 samples with various PTFE contents.
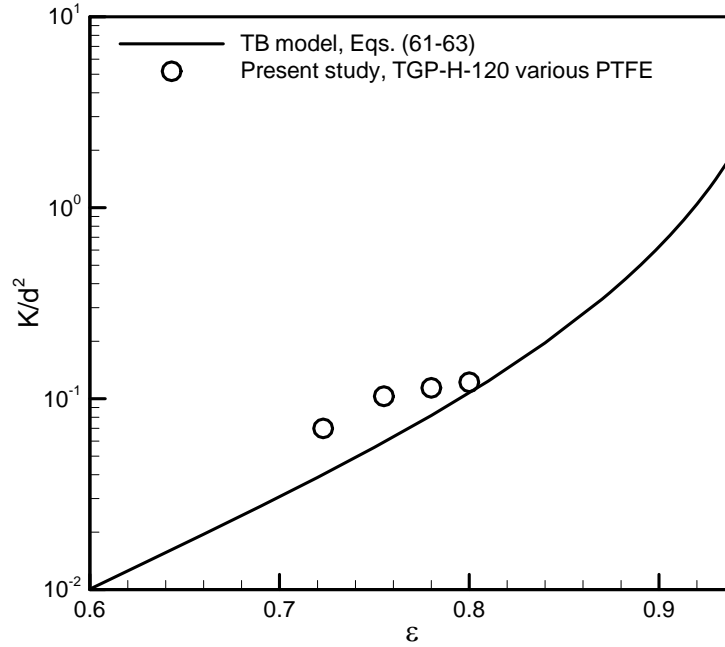
Figure 50: Comparison of the proposed model with the experimental data for TGP-H-120 with various PTFE contents.

3.7 Effect of microstructure on the flow properties of fibrous media

Our literature review revealed that no comprehensive studies exists in the literature on the effects of microstructure, especially fiber orientation, on the flow properties of fibrous materials in low to moderate range of Reynolds numbers. In addition, very few experimental works have been published for the flow through ordered fibers with moderate Reynolds numbers. In this study, the effects of porosity and fiber orientation on the flow coefficients of mono-dispersed fibrous materials are investigated. Parallel and transverse flow through a variety of fibrous matrices including square fiber arrangements, simple two directional mats, and simple cubic structures, shown in Figure 36 and Figure 37, are solved numerically over the porosity range of $0.4 < \varepsilon < 0.95$ and Reynolds number range of $0.01 < Re < 200$. The results are then used to find permeability and the inertial coefficient of the solid matrices. To verify the present numerical results, pressure

96

drop through three different tube banks with porosity range of $0.8 < \varepsilon < 0.9$ are tested using various water-glycerol mixtures to determine the flow coefficients.

If the pore sizes are much larger than the molecular mean free path, flow in pore scale is governed by Navier-Stokes equation; that is the continuum flow hypothesis which is considered here. Assuming incompressible, steady state flow, the microscopic equations become [118]:

$$\nabla . \vec{V} = 0 \tag{64}$$

$$\rho \vec{V} . \nabla \vec{V} = -\nabla P + \mu \nabla^2 \vec{V} \tag{65}$$

where $\vec{V}$ is the pore scale velocity vector, ρ and μ are the fluid density and viscosity, respectively. Eqs. (64) and (65) are subject to no-slip boundary condition at the fibers' surface. After volume averaging, Eq. (65) leads to Eq. (2) and in the creeping flow limit, reduces to Eq. (1). Equation (2) is usually written in the following form [1]:

$$-\nabla P = \frac{\mu}{K} U_D + \frac{\rho F}{\sqrt{K}} U_D^2 \tag{66}$$

where F is a dimensionless number called the Forchheimer coefficient. A special form of Eq. (66) is the Ergun equation:

$$-\nabla P = 150 \frac{(1-\varepsilon)^2}{\varepsilon^3 d^2} U_D + 1.75 \frac{(1-\varepsilon)}{\varepsilon^3 d} U_D^2 \tag{67}$$

where $K = \varepsilon^3 d^2 / 150(1-\varepsilon)^2$ and $F = 0.14 / \varepsilon^{3/2}$. Ergun equation is based on a curve fit of experimental data collected for granular materials [1].

3.7.1   Experimental approach

Experimental data for moderate Reynolds number flow through the fibrous structures that are of our interest is not abundant in the open literature. Three samples of tube banks with 1D square arrangement shown in Figure 38 were tested. To fabricate the tube bank sample, Polymethyl methacrylate (PMMA) sheets of 3 *mm* thickness were cut and drilled using a laser cutter with the accuracy of 0.05 *mm*. Glass capillary tubes with diameter of 1.5 *mm* were inserted and fixed using an adhesive tape to form the tube banks, as shown in Figure 38. The length of the tube banks were selected such that a minimum of 15 rows of cylinders existed in the flow direction for each sample. The properties of the samples are summarized in Table 7.

A custom-made gravity driven test bed, illustrated in Figure 38, was built that included an elevated reservoir, an entry section, a sample holder section, and an exit section with a ball valve. The liquid level was kept constant during the experiment to ensure that the variation of the pressure head was negligible during the experiment. The pressure drop across the samples was measured using a differential pressure transducer, PX-154 (BEC Controls). To minimize entrance and exit effects on the pressure drop measurements, pressure taps were located few rows apart (at least three rows) from the first and the last tube rows in the tube bank samples. Several water-glycerol mixtures with different mass concentrations and viscosities (0.015-1.4 *Ns/m^2*) were used to change the flow Reynolds number from 0.001 to 15. The bulk flow was calculated by weighting the collected test fluid over a period of time. The maximum uncertainty in the flow rate measurements was 4%.

To obtain the permeability and the inertial coefficient from the measured pressure drop (dp/dx) and mass flow rate values, the volume averaged superficial velocity, U_D, was calculated from the mass flow rate data and then $(dp/dx)/\mu U_D$ was plotted versus $\rho U_D/\mu$. The y-intercept and the slope of the data were then $1/K$ and $F/\sqrt{K}$, respectively; see Eq. (66). Using Eq. (2), the inertial coefficient was then calculated. From Figure 51, it can be seen that the measured pressure drops present a parabolic relationship with the volume-averaged velocity.

The uncertainty associated with the permeability and inertial coefficient, calculated based on the measured variables, can be estimated as:

$$\frac{E(\beta,K)}{\beta,K} = \sqrt{\left(\frac{E(\rho\,U_D/\mu)}{\rho\,U_D/\mu}\right)^2 + \left(\frac{E(\Delta P/L\mu U_D)}{\Delta P/L\mu U_D}\right)^2} \qquad (68)$$

where:

$$\frac{E(\rho\,U_D/\mu)}{\rho\,U_D/\mu} = \sqrt{\left(\frac{E(\rho)}{\rho}\right)^2 + \left(\frac{E(U_D)}{U_D}\right)^2 + \left(\frac{E(\mu)}{\mu}\right)^2} \qquad (69)$$

$$\frac{E(\Delta P/L\mu U_D)}{\Delta P/L\mu U_D} = \sqrt{\left(\frac{E(\Delta P/L)}{\Delta P/L}\right)^2 + \left(\frac{E(U_D)}{U_D}\right)^2 + \left(\frac{E(\mu)}{\mu}\right)^2} \qquad (70)$$

$E(.)$ is the uncertainty in measurement of each parameter; these values are listed in Table 11. The maximum uncertainty in the experimental values of permeability and inertial coefficient is estimated to be 12%.
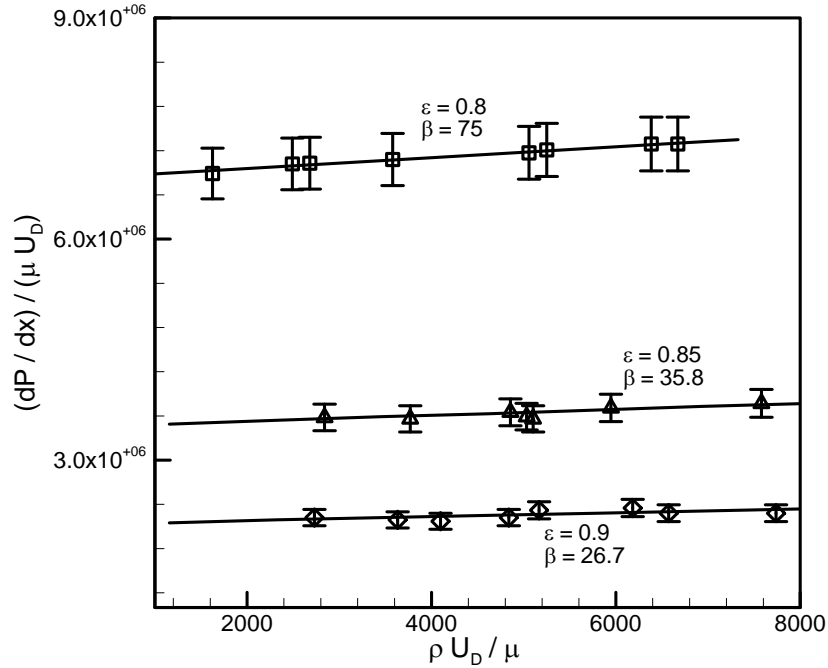
Figure 51: Measured values of $1/\mu U_D \left(dp/dx \right)$ **for the samples of tube bank with square fiber arrangement.**

Table 11: Uncertainty in the measured parameters.

Parameter	Uncertainty
ρ	3%
$\Delta P / L$	1% of full scale
Q	4% of full scale
U_D	4%
K	12%
β	12%

3.7.2   Numerical procedure

Equations (64) and (65) are solved using Fluent [122] which is a finite volume based software. The second order upwind scheme is selected to discretize the governing equations and SIMPLE algorithm [123] is employed for pressure-velocity coupling. The inlet and outlet boundaries of the computational domains are considered to be periodic,

i.e., the velocity distributions on both boundaries are the same [122]. The symmetry boundary condition is applied on the side borders of the considered unit cells; this means that normal velocity and gradient of parallel component of the velocity on the side borders are zero. However, for three dimensional cases, employing the periodic condition leads to a poor convergence rate. As a result of our limited computational resources, in some cases, a set of 7-10 unit cells in series are considered and velocity profiles are compared at the entrance to each unit cell. For these cases, the inlet velocity of the media is assumed to be uniform. Constant pressure boundary condition is applied on the computational domain outlet. The pressure drops used for calculation of flow properties are only the values obtained from the developed regions.

Structured grids and unstructured grids are generated for 1D/2D and 3D networks, respectively, using Gambit [122], the pre-processor in Fluent software. Numerical grid aspect ratios are kept in the range of 1-7. Grid independence is tested for different cases and the size of the computational grids used for each geometry is selected such that the maximum difference in the predicted values for pressure gradient is less than 2%. The maximum number of grids used for 1D and 2D/3D structures are approximately 14k and 1,400k, respectively. It should be noted that the convergence criterion, maximum relative error in the value of dependent variables between two successive iterations, is set at 10^{-6}.

In this part, numerical simulations are carried out for fibrous networks in the porosity range of 0.3 - 0.95 and in the Reynolds number range of 0.001 – 200. SC arrangements are orthotropic while the rest of the considered structures are anisotropic [11]. Therefore, numerical simulations are conducted for flow parallel to different coordinate axes. The same method as described in the previous section is employed to

determine the permeability and the inertial/Forchheimer coefficient from numerical results for different unit cells. The summary of the computed flow coefficients are reported in Table 12.

Flow parallel to axes of square arrays of cylinders is similar to laminar channel flows. This leads to zero value for Forchheimer coefficient in parallel flow as reported in Table 12. Similarly, for 2D structures, the in-plane Forchheimer coefficients have lower values than the calculated values for through-plane flow. This is resulted from the fact that 50% of the fibers in the considered geometry are parallel to the flow direction. Therefore, no inertial drag forces are exerted on these fibers.

3.7.3 Comparison of the numerical results with existing data in the literature

3.7.3.1 Square arrangement (1D)

To validate the numerical analysis, the calculated values of the dimensionless normal permeability, K/d^2, are successfully compared with present experimental results and the data collected from several sources in Figure 52. Moreover, in Figure 53, the calculated Forchheimer coefficients for square arrangements are compared with the present experimental data, the numerical results of Ghaddar [84] and Papathanasiou et al. [85] for monodisperse and bimodal fiber arrays, respectively. In addition, the experimental data of Bergelin et al. [61] (oil flowing across tube banks) are included in Figure 53. In general, the present results are in good agreement with the collected and reported data by others.

Table 12: Flow properties for the considered fibrous structures.

Square array (1D)					
Normal flow			Parallel flow		
ε	K/d^2	F	ε	K/d^2	F
0.45	0.0015	0.13	0.45	0.0079	0
0.65	0.014	0.026	0.55	0.0177	0
0.8	0.072	0.018	0.65	0.0378	0
0.9	0.300	0.011	0.8	0.1667	0
0.95	0.892	0.009	0.9	0.643	0

Planar structures (2D)					
Through plane flow			In-plane flow		
ε	K/d^2	F	ε	K/d^2	F
0.35	0.0007	0.313	0.35	0.0016	0.092
0.5	0.0046	0.118	0.5	0.0069	0.046
0.6	0.012	0.091	0.6	0.0164	0.033
0.8	0.106	0.033	0.8	0.0807	0.018
0.9	0.439	0.0028	0.9	0.4119	0.013

Simple cubic (3D)		
ε	K/d^2	F
0.31	0.0011	0.914
0.37	0.0023	0.562
0.59	0.0174	0.141
0.79	0.118	0.041
0.87	0.336	0.024
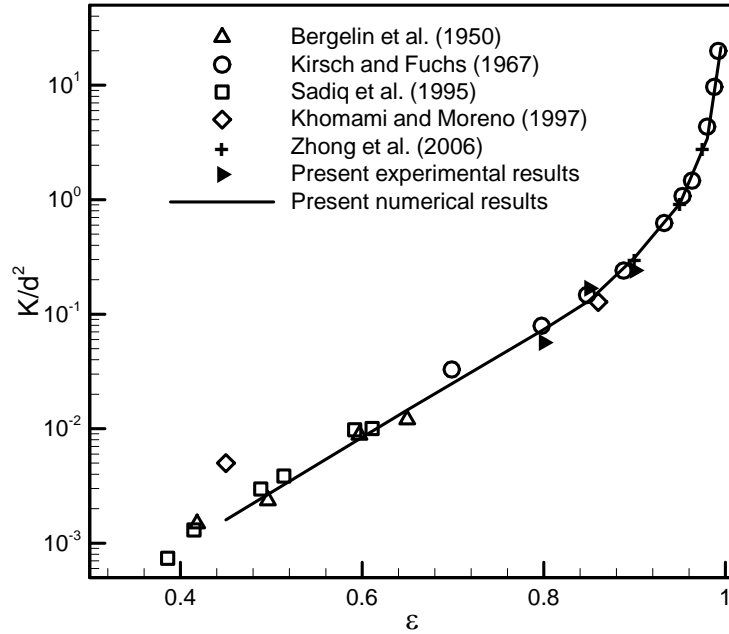
Figure 52: Comparison between the present numerical results, collected experimental results, and data from various sources, for normal flow through square fiber arrays.
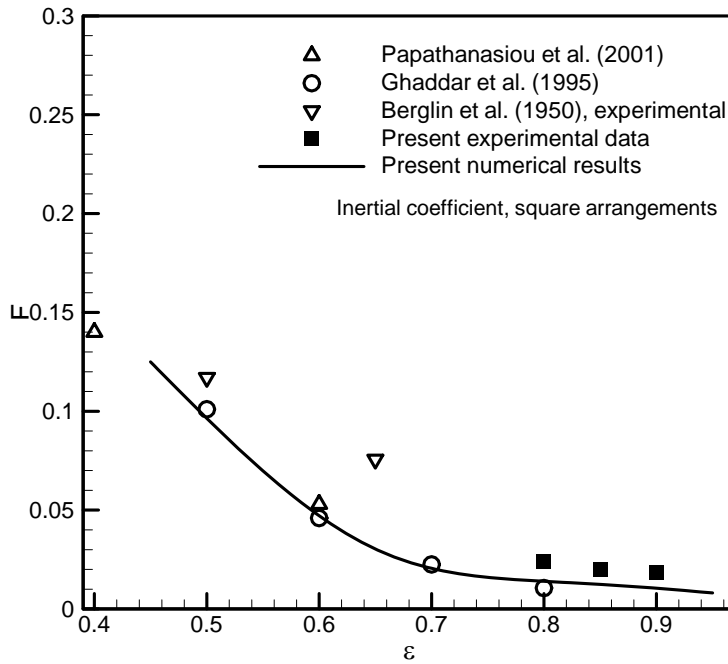
Figure 53: Comparison between the present numerical and experimental results for Forchheimer coefficient with experimental and numerical data of others.

3.7.3.2 2D and 3D simple cubic structures

There is no experimental data for moderate Reynolds number flows through the ordered 2D and 3D structures considered in the present study. To validate the analysis, the calculated permeability values for simple cubic arrangement are compared with the numerical results of Higdon and Ford [40] and experimental data for actual 3D materials with random fiber distribution collected from different sources in Figure 54. The plotted data are based on permeability results for polymer chain in solutions [65], glass wool randomly packed, stainless steel crimps [22], metallic fibers [69], and aluminum metal foams [94, 135].

3.7.4 Effects of microstructure on flow properties

Effects of microstructure and more specifically fibers orientation on permeability and Forchheimer coefficient are investigated in Figure 55 and Figure 56, respectively. As expected, 1D arrangements are the most anisotropic geometry and the normal and parallel permeability of such structures provide the lower and upper bounds for permeability of fibrous media. Effects of microstructure are more pronounced in lower porosities.

The plotted data in Figure 56 indicates that 1D and 2D geometries are anisotropic and the Forchheimer coefficient for 3D structures is higher than values for 1D and 2D geometries. The Forchheimer coefficient is a measure of inertial effects. Thus, it is more influenced by microstructure in the porosity range of $\varepsilon < 0.7$.

105
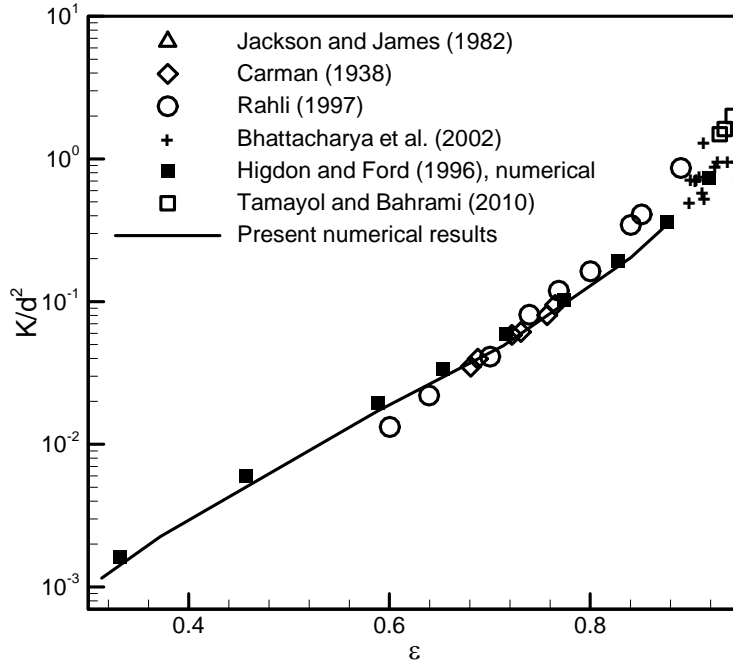
Figure 54: Comparison between the present numerical results for permeability of simple cubic arrangements with existing numerical and experimental data of 3D materials.
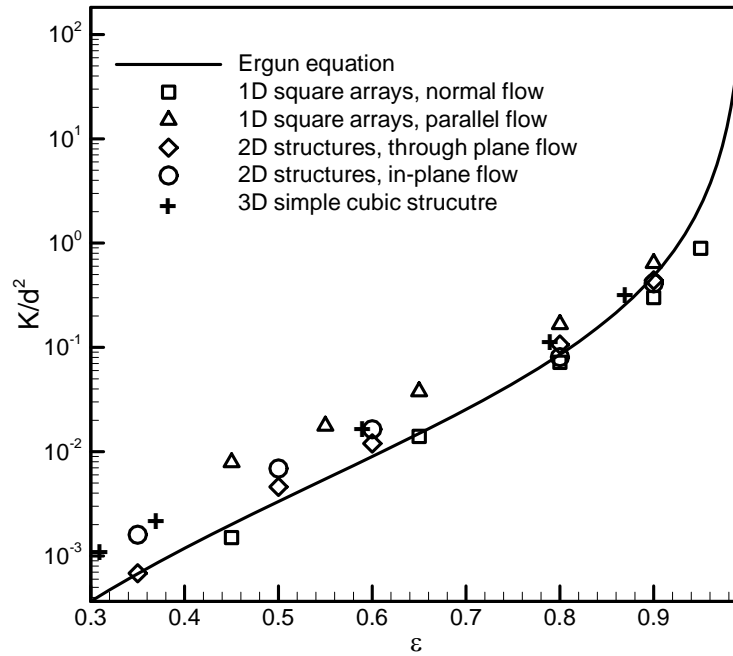
Figure 55: Comparison of numerical values of dimensionless permeability of fibrous media with Ergun equation.
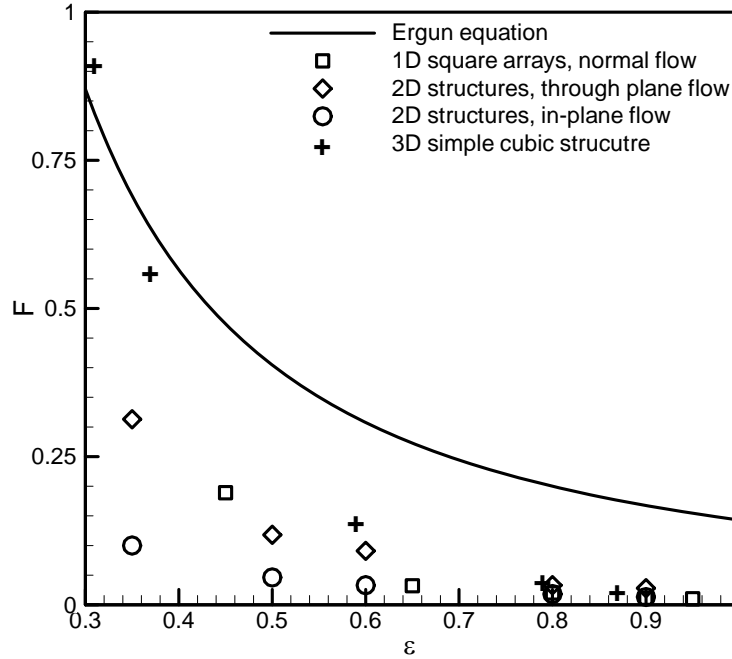
Figure 56: Comparison of numerical values of Forchheimer coefficient of fibrous media with Ergun equation.

Ergun equation, Eq. (67), is a widely accepted equation for prediction of pressure drop across granular materials. However; there are two main differences between fibrous and granular materials are:

- Shape of the particles in granular materials is spherical while fibrous media are made up of cylindrical like particles.

- Porosity of granular materials are in the range of 0.2 – 0.6, while the porosity of fibrous materials usually is in the range of 0.6 - 0.999.

The present numerical results are compared with the values predicted by the Ergun equation to investigate the accuracy of this equation for high porosity fibrous structures. Figure 55 includes the predicted values of permeability from Ergun equation and the present numerical results. It can be seen that the Ergun equation can only predict trends of numerical data qualitatively and the differences are significant especially in low

107

porosities. The Forchheimer results calculated from the Ergun equation are plotted against the current numerical results in Figure 56. The comparison shows that the Ergun equation is only in agreement with numerical results for 3D materials with low porosities. For higher porosities Eq. (67) is incapable of predicting the pressure drop for fibrous media.

Creeping flow through fibrous media has been investigated in the previous subsections and accurate models have been proposed for calculating the permeability. However, no compact relationships exist for estimating the Forchheimer coefficient of various fibrous structures. Using our numerical results, a series of compact correlations are developed for 1D, 2D, and 3D fibrous structures and are listed in Table 13. The proposed correlations are accurate within 2% of the present numerical results.

Table 13: Proposed compact correlations for Forchheimer coefficient in fibrous media.

Flow direction/microstructure	$F = \left(a + b \varepsilon \right)^{-1/c}$		
	a	b	c
Normal/square arrays (1D)	-5.32	18.42	0.532
Through plane- 2D structures	-0.14	5.05	0.418
In-plane/2D structures	1.037	0.0863	0.025
Simple cubic arrangements (3D)	0.534	1.56	0.184

4: MACROSCOPIC FLOW IN CONFINED POROUS MEDIA

In some applications, the porous material is confined by solid walls, e.g., mini/microchannels filled with porous media (micro-porous channels), or the flow inside the porous media is boundary driven. In such applications, flow and pressure distribution in the porous media cannot be described by the Darcy's law. In the present thesis, flow in channels fully and partially filled channels is investigated.

4.1 Pressure drop in microchannels filled with porous media

The porous medium is represented by several square arrangements of cylinders. The micro-porous channel, shown in Figure 57, consists of repeating square arrangements of mono disperse cylinders, embedded in a rectangular microchannel of depth h. In the creeping flow regime, the volume-averaged velocity distribution is given by Brinkman equation [19]:

$$-\frac{dP}{dx} = \frac{\mu}{K} U_D + \mu_{eff} \frac{d^2 U_D}{dy^2} \tag{71}$$

where μ_{eff} is called the effective viscosity. Previous studies have shown that the viscosity ratio $\mu' = \mu / \mu_{eff}$, varies between 1 to 10 [136]. Some researchers has postulated that $\mu' = 1$; see for example [137]. According to [137], this assumption is

reasonable for highly porous materials. However, Ochoa-Tapia and Whitaker [116] have shown that $\mu'=1/\varepsilon$ is a more suitable estimation.

The last term in the right hand side of Eq. (71) has been originally added to the Darcy equation to allow considering the no-slip boundary condition on solid walls. In the limiting case where either there is no porous medium inside the channel or the boundary effects are dominant, Darcy term, the first term in the right hand side of Eq. (71), vanishes and this equation becomes identical to Navier-Stokes (NS) equation. On the other hand, in the limit of very dense porous media, the Darcy term becomes dominant and Eq. (71) reduces to Eq. (1).

Hooman and Merrikh [138] developed analytical solutions for flow and pressure drop inside large scale rectangular channels filled with porous media:

$$-\frac{\Delta P}{L} = \frac{\mu}{Wh^3} \frac{1}{2\sum\limits_{n=1}^{\infty}\frac{1}{\lambda_n^2 m^2}\left(1-\frac{\tanh m\varepsilon'}{m\varepsilon'}\right)} \tag{72}$$
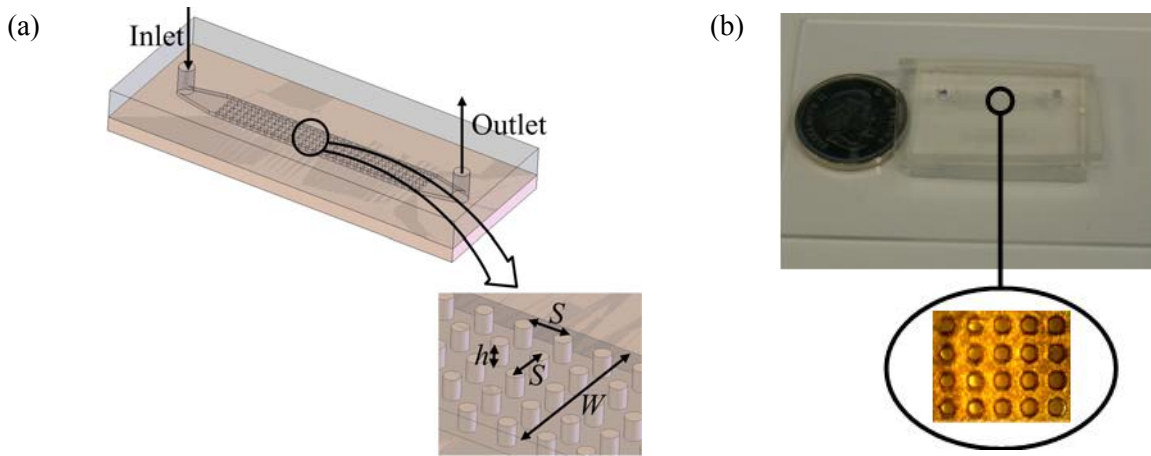
Figure 57: Structure of the considered micro-porous channels a) the schematic, b) a fabricated sample.

Where:

$$\varepsilon' = \frac{h}{W}, \quad \lambda_n = \frac{(2n-1)\pi}{2}, \quad Da = \frac{h}{\sqrt{K}}, \quad m = \left(\lambda_n^2 + Da^2\right)^{1/2} \tag{73}$$

and h, L and W are the depth, length, and width of the porous channel, respectively. They also assumed that $\mu' = 1$. The cross-sectional aspect ratio, $\varepsilon' = h/W$, in the samples tested in the present study is smaller than 0.1. Therefore, instead of considering the whole rectangular cross-section, the sample can be envisioned as a porous medium sandwiched between two parallel plates as shown in Figure 58. The solution of Eq. (71), the volume averaged velocity distribution, for 2D flow between parallel plates subject to no-slip boundary condition on the channel walls becomes:

$$U = \frac{K}{\mu} \frac{dP}{dx} \left[\frac{\sinh\left(\frac{y}{\sqrt{\mu' K}}\right) - \sinh\left(\frac{y-h}{\sqrt{\mu' K}}\right)}{\sinh\left(\frac{h}{\sqrt{\mu' K}}\right)} - 1 \right] \tag{74}$$

Consequently, the pressure drop for the simplified geometry becomes:

$$-\frac{\Delta P}{L} = \frac{\mu Q \sinh\left(\frac{h}{\sqrt{\mu' K}}\right)}{K h \left[2\frac{\sqrt{\mu' K}}{h}\left[-1 + \cosh\left(\frac{h}{\sqrt{\mu' K}}\right)\right] - \sinh\left(\frac{h}{\sqrt{\mu' K}}\right)\right]} \tag{75}$$

To determine the pressure drop from Eq. (75), one needs to calculate the permeability of the fibers arrangement in normal directions from the model developed in Section 4.2, Eq. (51).

$U(h) = 0$

h

y

x

$U(0) = 0$
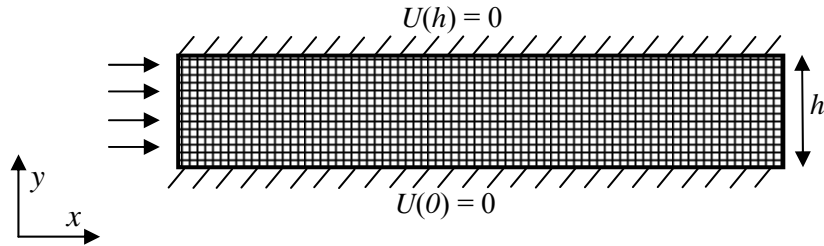
Figure 58: Schematic of the simplified 2D geometry.

4.2 Experimental procedure

4.2.1 Microfabrication

4.2.1.1 Soft lithography

Five different PDMS/PDMS samples were fabricated using the soft lithography technique [139] described by Erickson et al. [140]. A schematic of the process is provided in Figure 59. The fabrication process has two main parts: 1) preparing the mold; 2) making the PDMS replica.

SU-8 was used for preparing the molds; SU-8 is a negative tone epoxy-based photoresist that can be photo patterned using deep UV light. SU-8-100 was chosen for micromold fabrication as it can be patterned in very thick films (up to 1mm thick) and can make an excellent mold for PDMS. Square glass slides of 75 x 75 *mm* and 1 *mm* thick were used as substrates which were first cleaned in 100% Micro 90 Detergent (purchased from International Products Corporation, USA) using ultrasonic agitation for 5 minutes and then rinsed with de-ionized (DI) water, acetone, isopropyl alcohol (IPA) and DI water. Substrates were blow dried using nitrogen followed by dehydration baking for 20 minutes at 120 °*C* in a convection oven and cooling to room temperature. A 25 *nm* thick chrome layer was sputtered on each glass substrate which acts as an adhesion promoter

for the SU-8 100. A 100 μm thick layer of SU-8 100 was spin coated (at 2250 RPM) on top of the adhesion layer of each substrate, followed by soft baking at 90 °C for 80 minutes and cooling to room temperature. Structures were patterned using photolithographic UV exposure through a photomask for 60 seconds. Full crosslinking of the SU-8 100 was achieved by a post-exposure bake at a temperature of 60°C for 65 minutes (ramp rate: 300 °C/hr) followed by cooling to room temperature. The structural layer on each substrate was then developed in SU-8 Developer (Microchem™) for 90 seconds in an ultrasonic bath. Liquid PDMS was then poured over the mold and trapped bubbles were extracted by placing the liquid PDMS inside a vacuum chamber for 1h. The replica was then cured at 85°C for 45 minutes yielding a negative cast of the microchannel pattern. An enclosed microchannel was then formed by bonding the PDMS cast with another piece of PDMS via plasma treatment. The fabrication steps are depicted in Figure 59.

As a result of the fabrication uncertainty, the sizes of the channels and the cylinders were different from their intended dimensions. To measure the actual sizes, an image processing technique, utilized by Akbari et al. [131], was used. Accuracy of this method was reported by Akbari et al. [131] to be 3.6 μm.

(a)

UV

Photo mask

SU8-100

Chrome

Glass slide

(b)

SU8-100

Chrome

Glass slide

(c)

PDMS

SU8-100 mold

Glass slide

(d)
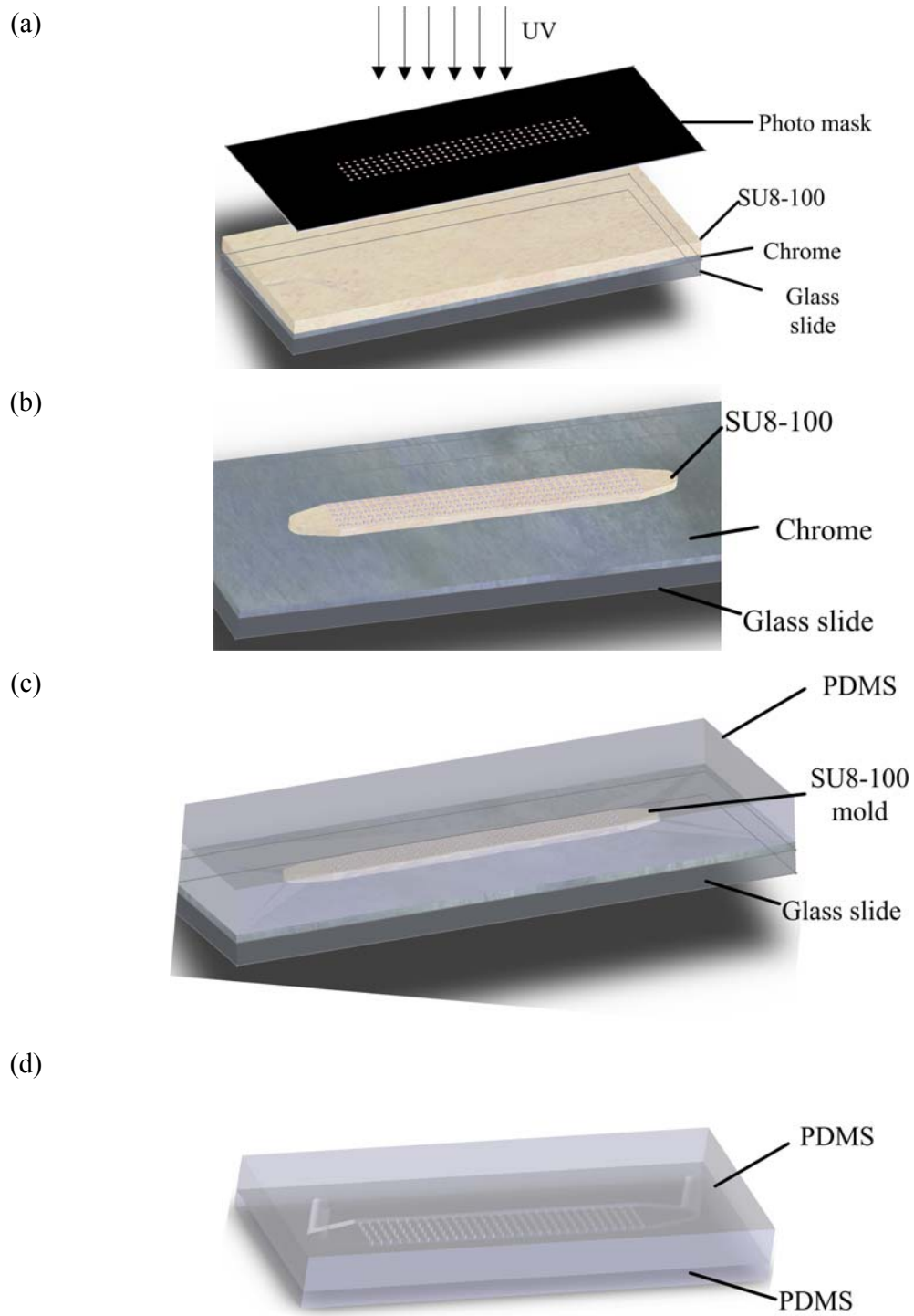
PDMS

PDMS

Figure 59: Fabrication process steps for SU-8 micromold preparation via photopatterning of SU-8 100 epoxy-based photopolymer: a) UV exposure, b) making the mold, c) pouring liquid PDMS, and d) plasma bonding and making the channels.

114

Our images revealed that the surfaces of the fabricated cylinders were rough, see Figure 60. As such, for determining the cylinders sizes, diameters of ten different cylinders were measured in three different directions for each sample and the average of these thirty values was considered as the size of the cylinders. In order to measure the width and the depth, the samples were cut at three random locations. The cutting lines were perpendicular to the channel to ensure a 90 deg viewing angle. The average of the measured values was considered as the actual size of the channels. The geometrical properties of the samples are summarized in Table 7. The channels' names in the table indicate the cylinder arrangement, intended porosity, and the expected cylinders diameter, e.g., Sq-0.40-400 corresponds to square arrangement of 400 μm cylinders with a porosity of 0.4. In addition, the permeability of the embedded porous media, calculated from Eq. (51), is reported in Table 14.

4.2.1.2 Test setup

The open loop system, illustrated in Figure 61, was employed for measuring the steady-state pressure drop in the fabricated samples of micro-porous channels. A syringe
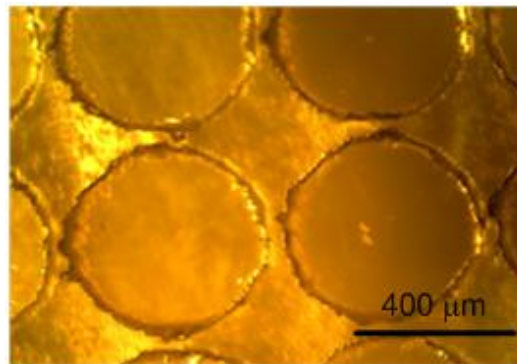
Figure 60: Rough surface of the fabricated cylinders, Sq 04-400 (1).

Table 14: Geometrical properties of the fabricated samples.

Channel	$d\ (\mu m)$	$S\ (\mu m)$	ε	$K\ (m^2)$, Eq. (51)
Sq-0.40-400 (1)	426	456	0.32	1.85×10^{-11}
Sq-0.40-400 (2)	418	456	0.34	3.30×10^{-11}
Sq-0.70-100	92	162	0.75	3.93×10^{-10}
Sq-0.90-50	52	129	0.89	8.49×10^{-10}
Sq-0.95-50	54	118	0.94	2.49×10^{-9}
Channel	$W\ (mm)$	$h\ (\mu m)$	$L\ (cm)$	
Sq-0.40-400 (1)	3.18	96	1.46	
Sq-0.40-400 (2)	3.19	105	1.46	
Sq-0.70-100	1.45	105	1.72	
Sq-0.90-50	1.27	129	2.00	
Sq-0.95-50	1.70	118	2.22	

pump (Harvard Apparatus, QC, Canada) fed the system with a controlled flow rate with 0.5% accuracy. Distilled water flowed through a submicron filter before entering the channel.

To measure the pressure drop, a gauge pressure transducer (Omega Inc., Laval, QC, Canada) was fixed at the channel inlet while the channel outlet was discharged to the atmosphere. Teflon tubing (Scientific Products and Equipment, North York, Canada) was employed to connect the pressure transducer to the syringe pump and the microchannel. Pressure drops were measured for several flow rates in the range of 50-800 $\mu lit/\min$.
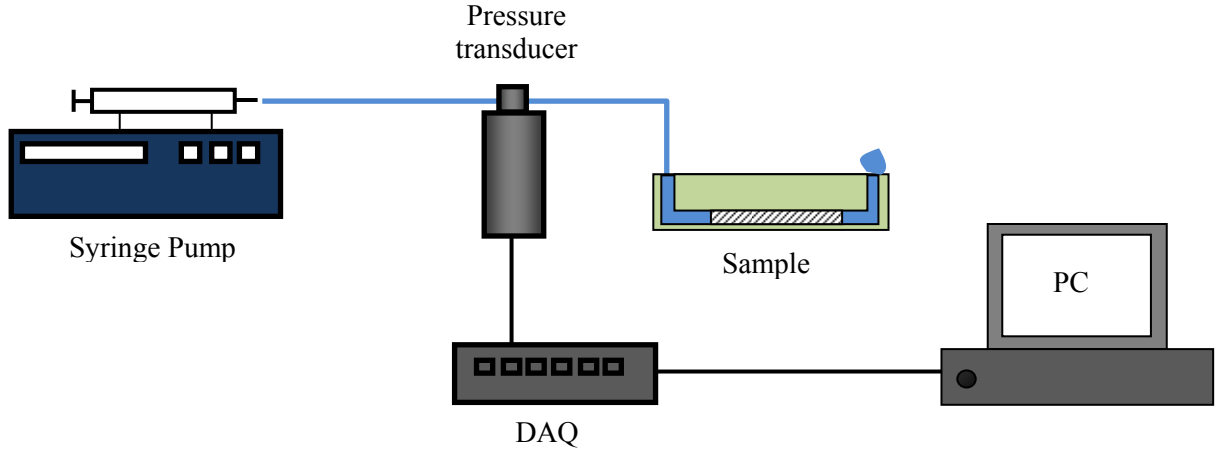
Figure 61: Schematic of the experimental setup for testing pressure drop in micro-porous channels.

4.2.1.3 Analysis of experimental data

Viscous dissipation effects are neglected in this study; thus, the properties of the flowing water are considered to be constant. The measured pressure drop during the experiment, ΔP_{total}, is:

$$\Delta P_{total} = \Delta P_c + \Delta P_D + \Delta P_{FD} + \Delta P_{minor} + \Delta P_{ev} \tag{76}$$

where ΔP_c is the pressure loss in the connecting tubes between the pressure transducer and the sample inlet, see Figure 61, ΔP_D is the pressure drop in the developing region of the samples where the fully-developed flow is not achieved, ΔP_{FD} is the pressure drop in the regions with fully-developed velocity distribution. ΔP_{minor} is the pressure drop due to minor losses in the samples including 90 deg bends in the inlet and outlet of the samples, and ΔP_{ev} is the pressure drop corresponding to the electroviscous effect [141]. Akbari et al. [131] showed that ΔP_{minor} and ΔP_{ev} are less than 1% of the ΔP_{FD} and can be neglected.

The connecting pressure loss, ΔP_C, is measured directly at each flow rate when the end of the tubing is disconnected from the sample. To perform accurate measurements, the level of the tubing end should be identical to the case where the samples are connected; this prevents any error due to hydrostatic pressure difference. Akbari et al. [131] showed that the developing pressure drop in microchannels is less than 1% of the total pressure loss and is negligible. In addition, for the case of pack fibers, fully-developed condition is achieved in the first three rows [63]. Therefore, it is expected that the measured pressure drop in the sample is associated with the fully-developed condition which is presented by Eq. (75).

The uncertainty of the analysis is mostly a result of the uncertainty in the fabrication process and the uncertainty in the measurements. These uncertainties will affect the porosity and consequently the permeability of the porous medium which is a nonlinear function of porosity. The uncertainty in the permeability predictions can be determined from the following relationship:

$$E(K) = \sqrt{\left(\frac{d(K)}{d(\varepsilon)}E(\varepsilon)\right)^2 + \left(\frac{d(K)}{d(d)}E(d)\right)^2} \tag{77}$$

The uncertainty in the measurement of pressure drop can be evaluated from the following equation:

$$E\left(\frac{\Delta P}{L}\right) = \sqrt{\left(\frac{d(\Delta P/L)}{d(Da)}E(Da)\right)^2 + \left(\frac{d(\Delta P/L)}{d(h)}E(h)\right)^2 + \left(\frac{d(\Delta P/L)}{d(K)}E(K)\right)^2 + \left(\frac{d(\Delta P/L)}{d(Q)}E(Q)\right)^2} \tag{78}$$

Table 15: Uncertainty in the calculation of the involved parameters.

Sample	$\dfrac{E(\varepsilon)}{\varepsilon}$	$\dfrac{E(K)}{K}$	$\dfrac{E(h)}{h}$	$\dfrac{E(\Delta P/L)}{(\Delta P/L)}$
Sq-0.40-400 (1)	0.02	0.59	0.10	0.60
Sq-0.40-400 (2)	0.02	0.54	0.10	0.55
Sq-0.70-100	0.026	0.34	0.10	0.36
Sq-0.90-50	0.02	0.44	0.08	0.44
Sq-0.95-50	0.01	0.07	0.08	0.11

where:

$$\frac{E(Da)}{Da} = \sqrt{\left(\frac{E(h)}{h}\right)^2 + \left(\frac{1}{2}\frac{E(K)}{K}\right)^2} \tag{79}$$

The associated uncertainty with different parameters involved in the analysis is listed in Table 15. It can be seen that the overall uncertainty is significant; this is a direct result of the nonlinear nature of the relationship between geometrical parameters with permeability and the overall pressure drop. In the comparison of the experimental data with the theoretical predictions only the trends should be considered.

4.2.2 Comparison of the model with the experimental data

Figure 62 and Figure 63 include the measured values of pressure drop in the tested micro-porous channels versus the volumetric flow rate. The flow rates were selected such that the pressure drop in the channels was higher than the accuracy of the pressure transducer. It can be seen that the trends of the experimental data were well predicted by the theoretical results, Eq. (75). The difference between most of the measured data and the predicted values from Eq. (75) was less than %15. The deviations were more intense for Sq-0.9-50 (max 20%); therefore, the $\pm$ 15% region for theoretical

predictions is shown in Figure 63. It should be noted the deviation of the experimental data from the theoretical predictions is mostly caused by the inaccuracy in the channels cross-section measurement as discussed before and the deviations are lower than the uncertainty of the analysis.

The experimental values of pressure drop had a linear relationship with volumetric flow rate. It can be argued that the channels had not been deformed during the experiment else a nonlinear trend would have been observed in the experimental data; for detailed discussions see [142]. Moreover, the linear trend of the experimental data shows that the minor losses and the inertial effects are insignificant in the tested samples. It should be noted that the maximum Reynolds number based on cylinders' diameter is less than 5; this justifies the observed trends in the measured values.

4.2.3   Numerical simulations

Our analysis showed a significant uncertainty in the experimental study. Therefore, to further investigate the accuracy of the current analysis, the proposed analytical model will be verified through comparison with independent numerical simulations. Flow through 7 different geometries, listed in Table 16, is solved numerically using Fluent. The geometrical parameters of the fist 5 samples are identical to the fabricated channels. The geometry of the last 2 samples is selected such that a wider range of porosity and permeability is covered.
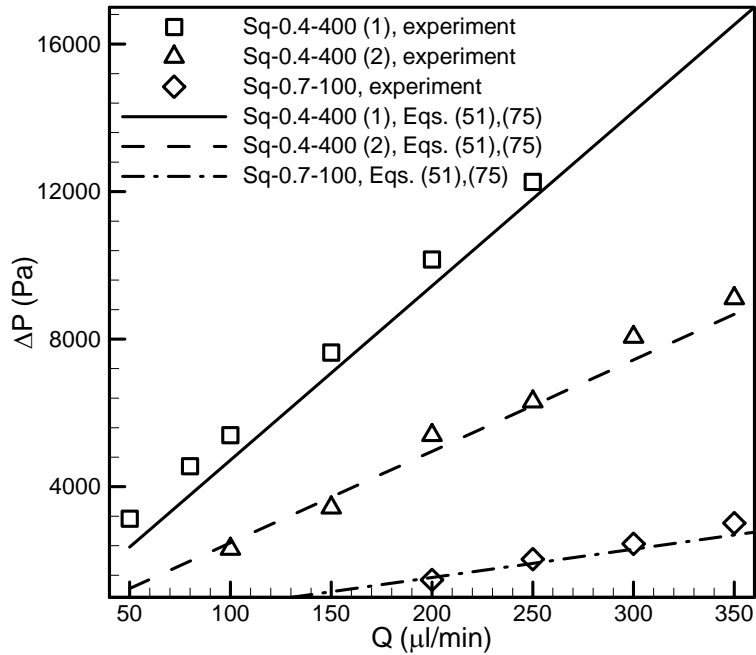
Figure 62: Channel pressure drop versus flow rate for Sq-0.4-400 (1), Sq-0.4-400 (2), and Sq-0.7-100. Lines show the theoretical values of pressure drop predicted by Eq. (75) and symbols show the experimental data.
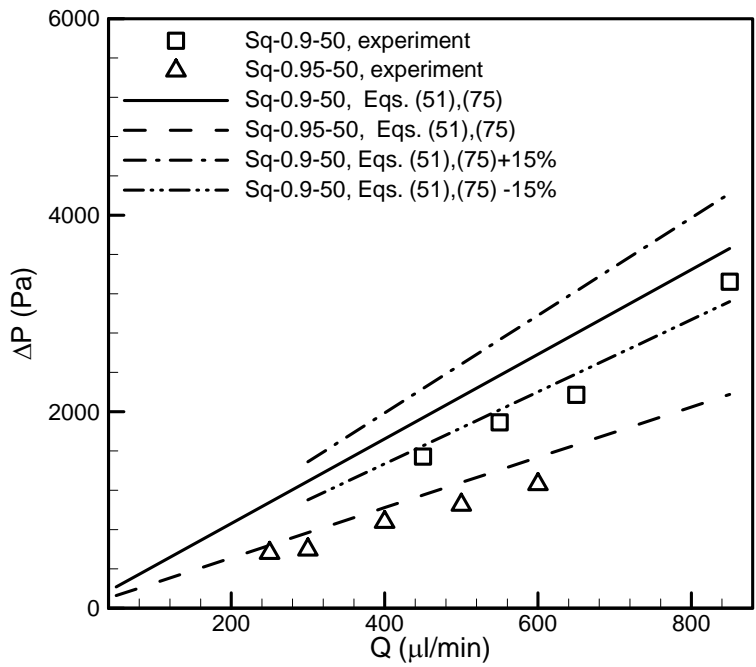
Figure 63: Channel pressure drop versus flow rate for Sq-0.9-50 and Sq-0.95-50. Lines show the theoretical values of pressure drop predicted by Eq. (75) and symbols show the experimental data.
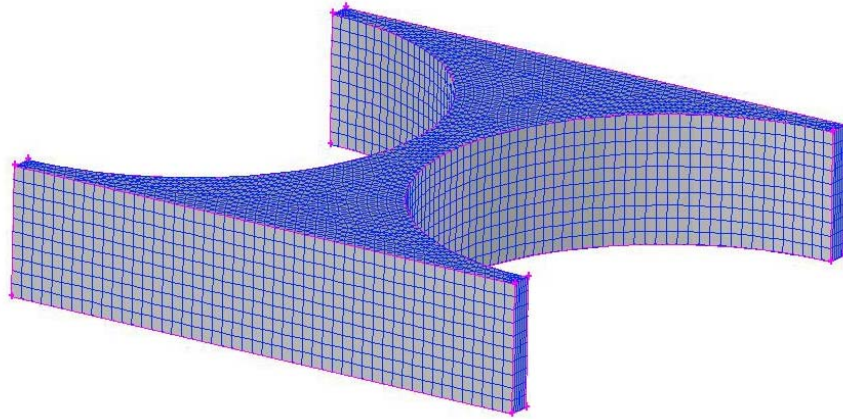
Figure 64: The considered unit cell and produced numerical grid for modeling of sample Sq-04-400(2).

The flow is assumed to be fully-developed, creeping, and constant properties (constant density and viscosity); therefore, modeling the region between two adjacent cylinders and applying a periodic boundary condition enable us to estimate the pressure gradient in the samples. An example of the considered geometry and the numerical grid produced by Gambit [122] is shown in Figure 64.

The volumetric flow rate is set in the range covered by the experimental data to ensure that the Reynolds number based on averaged velocity and the cylinders diameter is low and the inertial effects are negligible. Fluent software [122] is used as the solver. Second order upwind scheme is selected to discretize the governing equations. SIMPLE algorithm is employed for pressure-velocity coupling. The inlet and outlet faces of the geometry are considered to be Periodic. Symmetry boundary condition is applied at sides of the considered unit cell. Grid parameters are varied to assess whether the predicted pressure drops are independent of the computational grid.

Table 16: Geometrical parameters of the samples considered in the numerical simulations.

Channel	$d\,(\mu m)$	$S\,(\mu m)$	ε	$W\,(mm)$	$h\,(\mu m)$	$L\,(cm)$
Sq-0.40-400 (1)	426	456	0.32	3.18	96	1.46
Sq-0.40-400 (2)	418	456	0.34	3.19	105	1.46
Sq-0.40-400 (3)	400	450	0.4	3.15	100	1.5
Sq-0.50-400	400	500	0.5	3.0	100	1.5
Sq-0.70-100	92	162	0.75	1.45	105	1.72
Sq-0.90-50	52	129	0.89	1.27	129	2.00
Sq-0.95-50	54	118	0.94	1.70	118	2.22

In Figure 65 and Figure 66, the computed values of pressure drop for the tested samples are compared with the model and the experimental data. It can be seen that Eq. (75) can predict the trends of the experimental and numerical data; with the exception of Sq-0.9-50 the deviations between the model and the data is less than 15%. However, the difference between the numerical and the experimental results is due to the effects of the geometrical uncertainty involved in the experiments.

4.2.4 Parametric study

In the present micro-porous channels, two parameters affect the pressure drop: 1) the permeability, K; 2) the channel depth, h. To investigate the effect of these parameters, the dimensionless pressure drop is plotted versus the Darcy number in Figure 67. According to Nield and Kuznetsov [143] and Tamayol et al. [137], the hydrodynamic boundary layer thickness scales with $\sqrt{K}$. The Darcy number, $h/\sqrt{K}$, can be interpreted as the ratio of the boundary layer thickness to the depth of the channel.
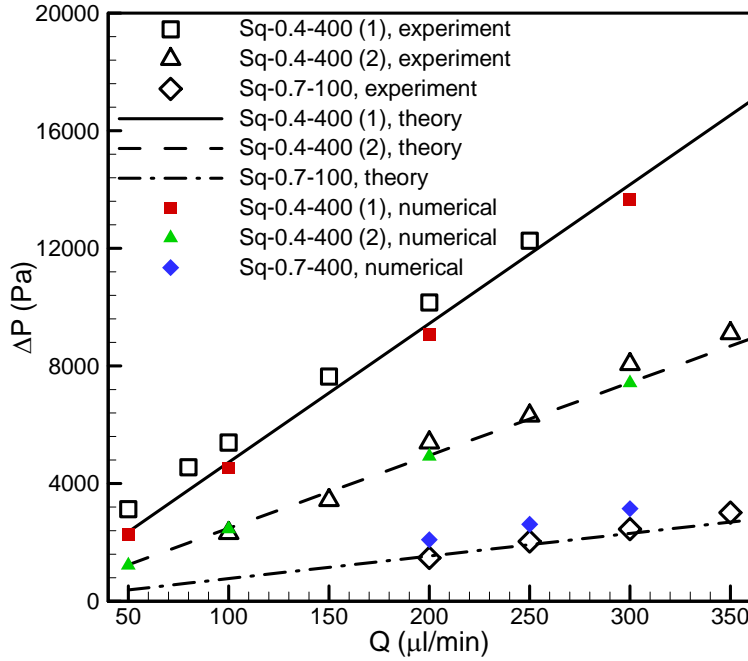
Figure 65: Experimental, numerical, and theoretical values of channel pressure drop predicted by Eq. (75) versus flow rate for Sq-0.4-400 (1), Sq-0.4-400 (2), and Sq-0.7-100.
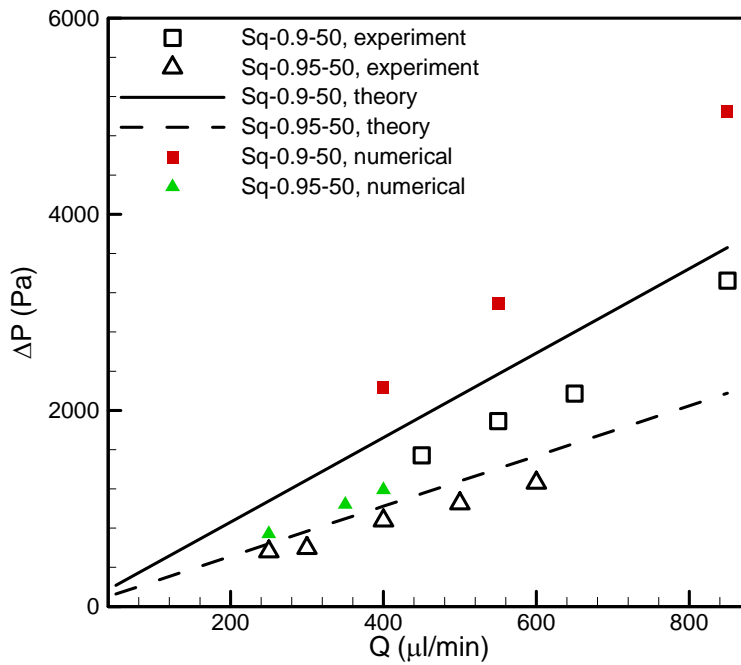
Figure 66: Experimental, numerical, and theoretical values of channel pressure drop predicted by Eq. (75) versus flow rate for Sq-0.9-50 and Sq-0.95-50.

Figure 67 shows that Eq. (75) is in reasonable agreement with the experimental data. In addition, it can be seen that Eq. (75) has two asymptotes. For micro-porous channels with very dilute porous medium, i.e., low Darcy number, the pressure drop can be predicted by solving the Navier-Stokes equation for plain fluid. For channels with very packed porous medium, i.e., high Darcy numbers, Eq. (75) and the Darcy law predict the same results. Therefore, one can conclude that the Darcy number can be used for determining the controlling parameter in the pressure drop in micro-porous channels.

4.3 Flow in channels partially filled with porous media

As discussed in Chapter 2, fluid flow in channel or systems partially filled with porous media has a wide range of engineering applications. In this study, creeping flow
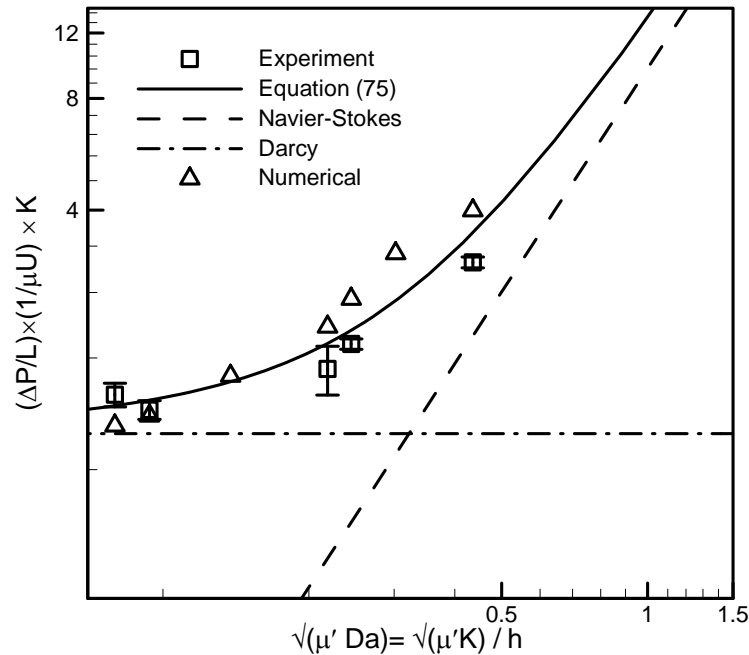
Figure 67: Dimensionless pressure drop versus Darcy number squared.

125

through mini/microchannels filled with regular arrays of cylinders, as shown in Figure 68, is investigated. Similar to the analysis of flow through channels fully filled with porous media, the channel is considered to be wide enough such that the flow-field can be modeled two dimensionally, as shown in Figure 68c. Moreover, flow is assumed to be incompressible, constant properties, fully-developed, and creeping.
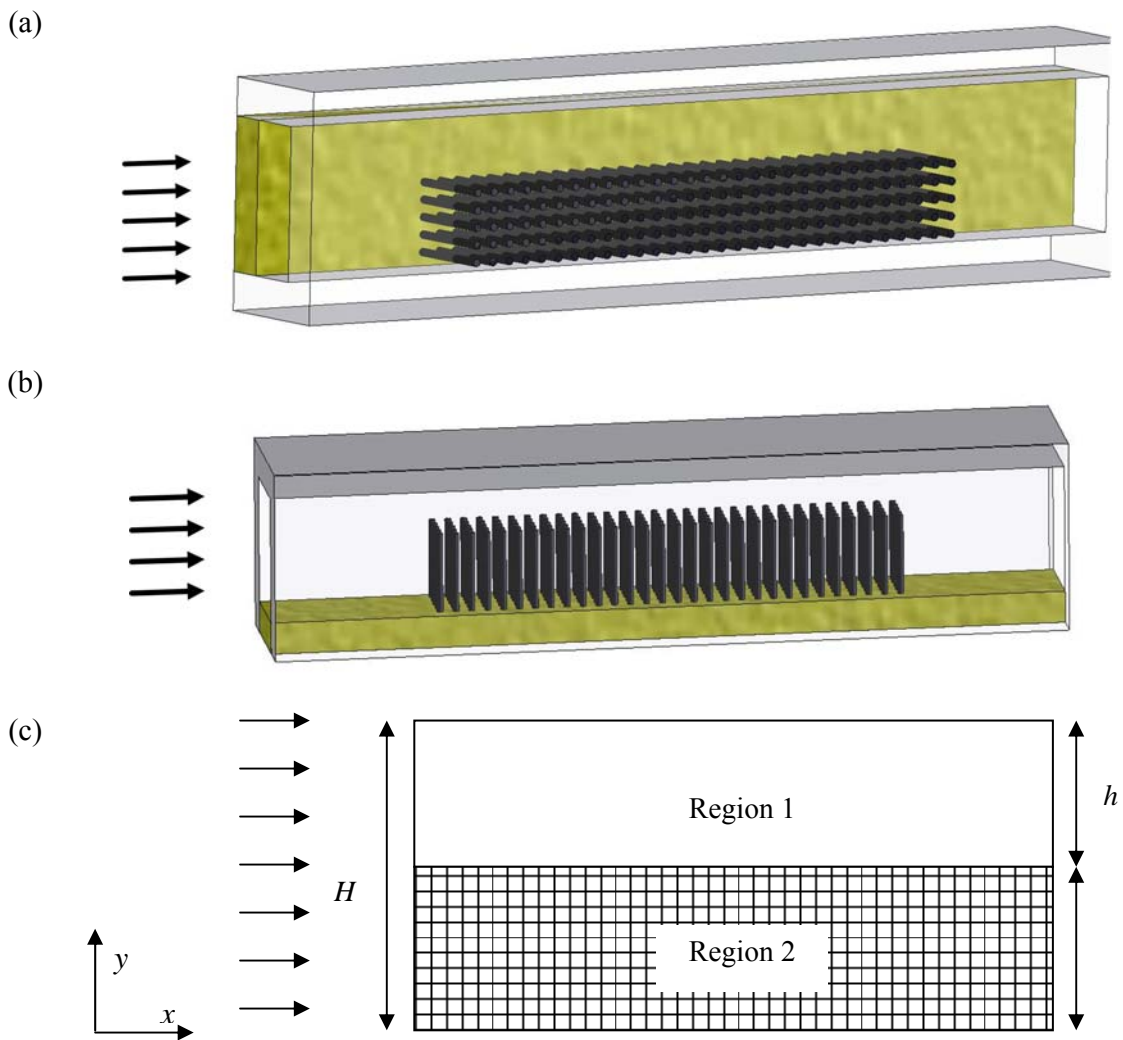
Figure 68: a) and b) Flow through channels partially filled with arrays of cylinders, c) simplified 2D geometry.

The domain can be divided into two regions. The upper region in Figure 68c only contains the fluid phase; thus, the Stokes equation can be used:

$$\frac{\partial^2 u}{\partial y^2} = -\frac{1}{\mu}\frac{dP}{dx}, \quad y \geq \delta \tag{80}$$

The applied boundary conditions in the region 1 are:

$$u(\delta) = u_{\text{int}}, \quad u(H) = 0 \tag{81}$$

where u_{int} is the interface velocity in the region 1. In the porous region (Region 2), Brinkman equation is used for calculating the volume averaged velocity distribution:

$$-\frac{dP}{dx} = \frac{\mu}{K}U_D + \mu_{eff}\frac{d^2 U_D}{dy^2}, \quad y \leq \delta \tag{82}$$

with the following boundary conditions:

$$U_D(0) = 0, \quad U_D(\delta) = U_{D\text{int}} \tag{83}$$

where $U_{D\text{int}}$ is the interface velocity in the porous region.

4.3.1 Solution development

The velocity distribution in the fluid region described by Eq. (80) subjected to boundary conditions (81), is:

$$u = -\frac{dP}{\mu\,dx}\left(\frac{(H-y)^2}{2} - \frac{(H-\delta)(H-y)}{2}\right) + u_{\text{int}}\frac{H-y}{H-\delta} \tag{84}$$

The solution of Eq. (82) with the boundary conditions of (83) is:

127

$$U_D = -\frac{dP}{\mu\,dx}K + C_1\,e^{y/\sqrt{\mu'K}} + C_2\,e^{-y/\sqrt{\mu'K}} \tag{85}$$

where:

$$C_2 = -\frac{dP}{\mu\,dx}K\left(\frac{1-e^{\delta/\sqrt{\mu'K}}}{e^{-\delta/\sqrt{\mu'K}}-e^{\delta/\sqrt{\mu'K}}}\right) + \frac{U_{D\text{int}}}{e^{-\delta/\sqrt{\mu'K}}-e^{\delta/\sqrt{\mu'K}}} \tag{86}$$

$$C_1 = -\frac{dP}{\mu\,dx}K - C_2 \tag{87}$$

In Eqs. (84)-(87), $U_{D\text{int}}$ and u_{int} remain unknown. These parameters can be found through applying suitable conditions at the fluid porous interface. Various interface boundary conditions proposed by researchers have been reviewed by Vafai and Alazmi [117]. Moreover, they [117] showed that the overall effects of various interface conditions on the velocity distribution are not significant. As such, the following conditions are considered at the interface:

$$U_D(\delta) = u(\delta), \quad \mu\left.\frac{du}{dy}\right|_{y=\delta} = \mu_{eff}\left.\frac{dU_D}{dy}\right|_{y=\delta} \tag{88}$$

which indicate the continuity of velocity and shear stress at the interface. Using Eqs. (84)-(87) and the interface conditions of (88) the interface velocity is calculated as:

$$U_{D\text{int}} = u_{\text{int}} =$$
$$\mu\frac{dp}{dx}\left[\frac{(H-\delta)\left(-2\mu'K+2\mu'K\cosh\left(\frac{\delta}{\sqrt{\mu'K}}\right)+\sqrt{\mu'K}(H-\delta)\sinh\left(\frac{\delta}{\sqrt{\mu'K}}\right)\right)}{2\left(\sqrt{\mu'}(H-\delta)\cosh\left(\frac{\delta}{\sqrt{\mu'K}}\right)+\sqrt{\mu'K}\sinh\left(\frac{\delta}{\sqrt{\mu'K}}\right)\right)}\right] \tag{89}$$

Having the velocity distribution, Eqs. (84)-(87) and (89) can be integrated over the entire area, H, to calculate the pressure drop as a function of flow rate and the geometrical properties of the channel and the porous medium. It is noteworthy that permeability should be calculated from Eq. (51).

4.3.2 Comparison with experimental data

Arthur et al. [115], using a PIV technique, measured the velocity distribution through a channel partially filled with porous media comprised of regular arrays of cylinders. The reported values for velocity in the porous region are volume averaged velocity. The properties of the tested samples are listed in Table 17. In Figure 69, the reported velocity profile reported by Arthur et al. [115] is compared by the theoretical calculations. It can be seen that the proposed solution can capture the observed trends in the experimental results with a reasonable accuracy. Moreover, It can be seen that as the porosity increases, i.e., the permeability increases, a larger volumetric flow rate passes through the porous medium. For the case 1 with $\varepsilon = 0.99$, the velocity distribution is very similar to an empty channel without porous medium and the effect of the porous medium is not significant.

4.3.3 Numerical simulations

To investigate the accuracy of the current analysis, the proposed analytical model will be verified through comparison with numerical simulations. Flow through 3 different geometries, listed in Table 18, is solved numerically using Fluent. The flow is assumed to

Table 17: Geometrical parameters and averaged velocity for the samples tested by Arthur et al. [115].

Case	$d\,(mm)$	$S\,(mm)$	ε	$H\,(mm)$	U (mm/s)
1	1.59	14.09	0.99	25	0.71
2	1.59	8.91	0.975	25	0.55
3	3.18	8.91	0.9	25	0.59
4	3.18	6.01	0.78	25	0.56
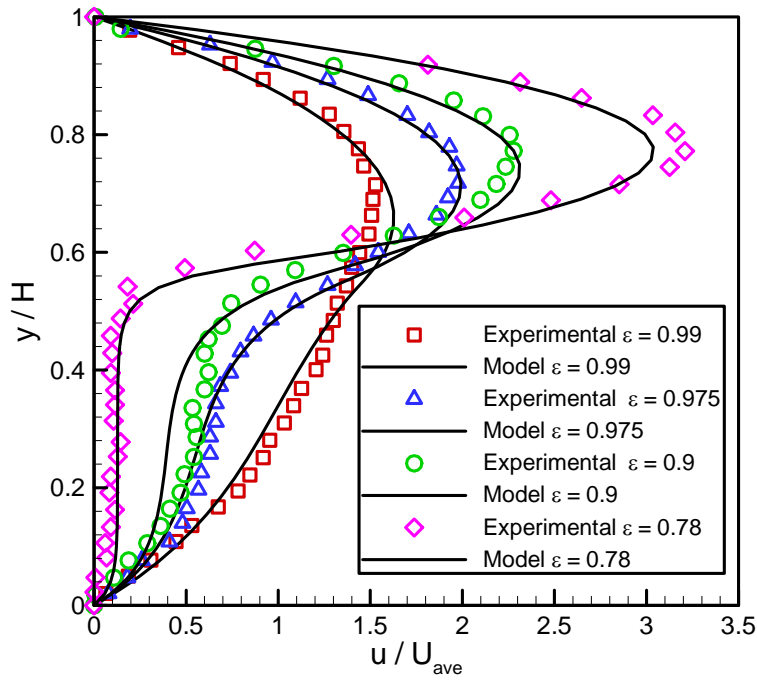
Figure 69: Comparison of the velocity distribution reported by Arthur et al. [115] and the theoretical predictions by Eqs. (51) and (89).

be fully-developed, creeping, and constant properties; therefore, by applying a periodic boundary condition, only flow through one row of cylinders is solved numerically. An example of the considered geometry and the numerical grid produced by Gambit [122] is shown in Figure 70.

130

Fluent software [122] is used as the solver. Second order upwind scheme is selected to discretize the governing equations. SIMPLE algorithm is employed for pressure-velocity coupling. The inlet and outlet faces of the geometry are considered to be Periodic. A no slip boundary condition is applied at the solid surfaces including the channel walls. Grid parameters are varied to test whether the predicted pressure drops are independent of the computational grid.

(a)

(b)
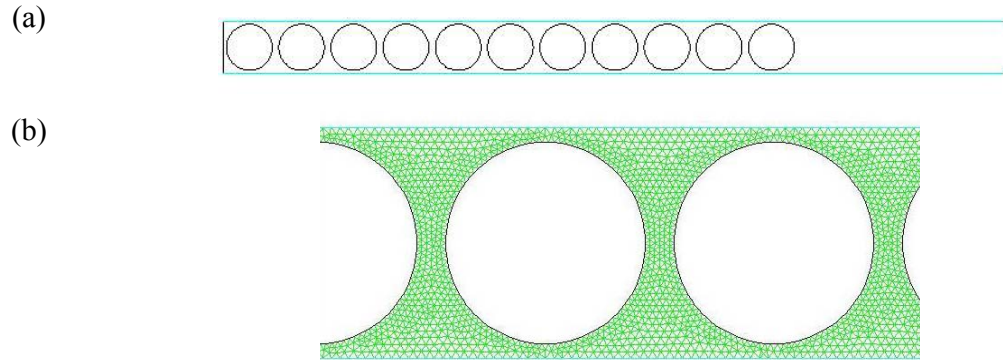
Figure 70: a) The considered geometry and b) the produced numerical grid for modeling of sample with ε =0.4.

The volume averaged and the actual velocity distributions for porous media with ε = 0.7 and 0.9 are compared in Figure 71 and Figure 72, respectively. The model can accurately predict the average of the actual velocity profiles.

Table 18: Geometrical parameters considered in the numerical simulations.

Channel	$d\,(\mu m)$	$S\,(\mu m)$	ε	$H\,(mm)$	$\delta\,(mm)$	$K\,(m^2)$
1	100	114	0.99	1.7	1.25	6.62×10^{-8}
2	100	162	0.975	2.4	1.75	2.79×10^{-6}
3	100	280	0.9	4.2	3.0	3.52×10^{-5}
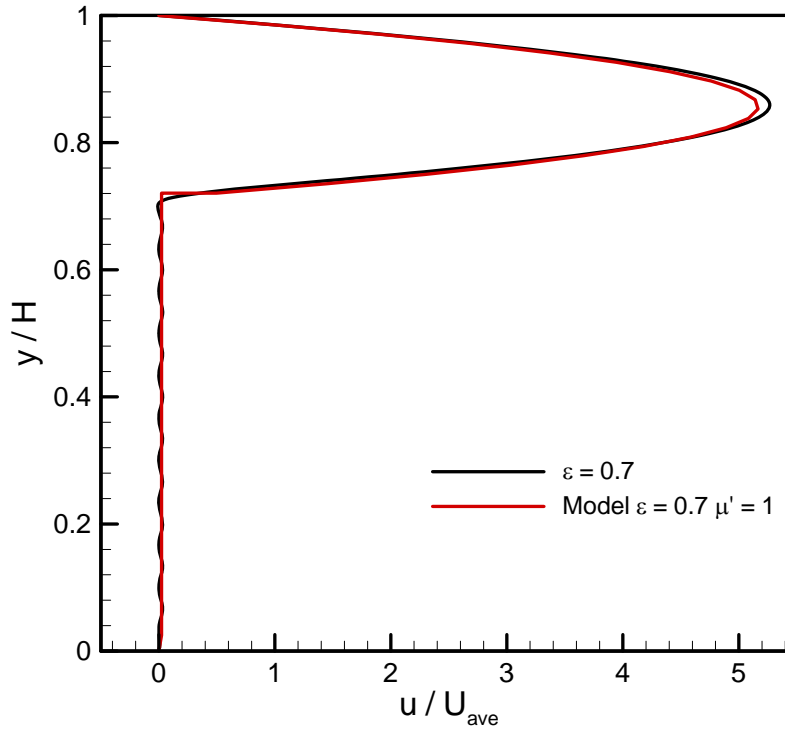
Figure 71: Comparison of the volume averaged (Eqs. (51) and (89)) and actual dimensionless velocity distributions in the channel filled with porous media with ε =0.7.

The computed velocity distributions for the three different cases are plotted in Figure 73. It can be seen that as the porosity increases, i.e., the permeability increases, a larger fraction of the flow passes through the porous medium. This is in agreement with the observed trends in the experimental data reported by Arthur et al. [115]. Therefore, for example for a typical fuel cell shown in Figure 4c where the GDL thickness is less than 400 μm, the in-plane permeability is approximately $1 \times 10^{-11} m^2$, and the channel height is 3 mm, less than 3% of flow passes through GDL. This result, confirms that gas transport in the GDL is mostly diffusive rather than convective.
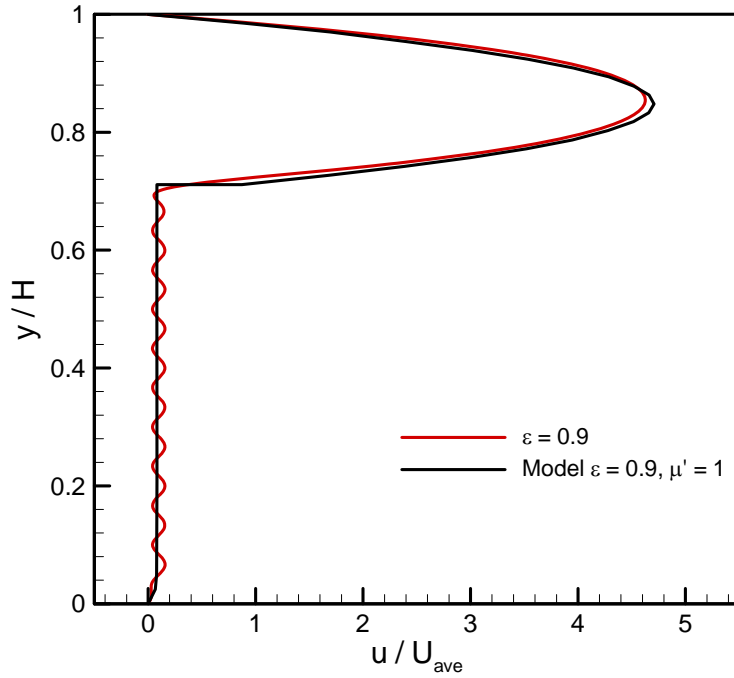
Figure 72: Comparison of the volume averaged (Eqs. (51) and (89))and actual dimensionless velocity distributions in the channel filled with porous media with ε =0.9.
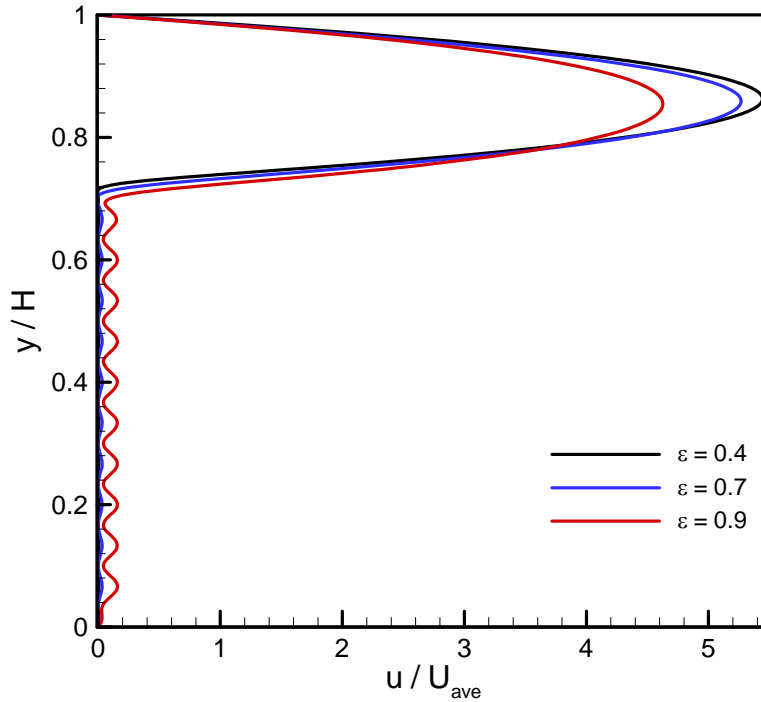
Figure 73: Effects of porosity on the dimensionless microscopic velocity distribution through the channels partially filled with porous media.

5: CONCLUSIONS AND FUTURE WORK

The main focuses of this dissertation were on studying flow through systems that include fibrous porous media and the resulting pressure drop both theoretically and experimentally. The project was divided into two main parts: i) microscopic analysis and ii) macroscopic modeling.

Flow properties of fibrous porous media including permeability and inertial coefficient were investigated. Various techniques were employed to develop fundamental understanding and models on the relationship between flow properties and salient geometrical parameters. Moreover, three different testbeds were designed and built for performing experiments to verify the theoretical analyses. The key contributions of the present dissertation in this part can be summarized as follows:

1- An approximate but accurate model for flow distribution and permeability of ordered arrays of fibers/cylinders was developed.

2- A novel scale analysis technique for permeability of 1D, 2D, and 3D fibrous materials was proposed. The developed relationships were verified through comparison with experimental data for a variety of materials measured during this research or reported by others.

3- Mixing rules were successfully employed for predicting in-plane permeability of complex, random microstructures.

4- Effects of compression and PTFE content on the permeability of GDLs were measured. Moreover, the proposed model could capture the observed trends in the experimental data.

5- Effects of salient microstructural properties specifically fiber orientation on the pressure drop for moderate Reynolds number flows were investigated. The results were used to develop correlations for inertial coefficient in the investigated materials.

In the second part of the thesis, the developed models for permeability were combined with volume-averaged equations to estimate volume-averaged velocity distribution and pressure drop in confined porous media. The considered problems were flow through channels fully or partially filled with fibrous media. The highlights of my research in this part are:

1- In a novel analysis, the accuracy of the Brinkman equation in the micron-size system was investigated.

2- Simple, closed-form analytical solutions for flow through channels partially filled with porous media were developed and it was shown that this simple analysis was accurate enough to be used in engineering analysis.

The outcomes of this dissertation provide new insights on the convective transport in fibrous porous materials and are beneficial for designing related systems such as fuel cells and compact heat exchangers.

5.1   Future plan

The following directions can be considered as the continuation of this dissertation:

1- Perform numerical simulations and experimental measurements on fibrous materials with random microstructure. This should be used to develop compact relationships for the inertial coefficient of the tested materials.

2- Extend the analysis to convective heat transfer. Specially, the scale analysis technique and the mixing rules have the potential to be used for determining the interstitial heat transfer coefficient of complex microstructures.

3- Investigate two phase flow through hydrophobic fibrous media such as GDLs of PEMFCs or porous structures with pore size distribution in the range of nano to micro millimeters. The water permeability (apparent permeability) in these structures is different from the actual permeability studied in this dissertation.

4- Conduct experiments on flow through various GDLs in the in-plane and through-plane directions and including effects of microporous layer in the analysis.

5- Test other regular and irregular arrays of microcylinders and also random fibrous nanostructures to verify the analysis for microchannels fully or partially filled with porous media for more cases.

6: REFERENCES

[1] M. Kaviany, Principles of Heat Transfer in Porous Media, 2nd ed., Springer-Verlag, New York, 1995.

[2] L. Tadrist, M. Miscevic, O. Rahli, F. Topin, About the use of fibrous materials in compact heat exchangers, Experimental Thermal and Fluid Science, 28(2-3) (2004) 193-199.

[3] S. Mahjoob, K. .Vafai, A synthesis of fluid and thermal transport models for metal foam heat exchangers, International Journal of Heat and Mass Transfer, 51(15-16) (2008) 3701-3711.

[4] G. A. Truskey, F. Yuan, D.E. Katz, Transport phenomena in biological systems, Pearson Prentience Hall New Jersey, 2004.

[5] L. Spielman, S. L. Goren, Model for predicting pressure drop and filtration efficiency in fibrous media, Current Research, 2 (1968) 279-287.

[6] M. A. Choi, M. H. Lee, J. Chang, S. J. Lee, Permeability modeling of fibrous media in composite processing, Journal of Non-Newtonian Fluid Mechanics, 79(2-3) (1998) 585-598.

[7] C. Antoine, P. Nygård, O. W. Gregersen, R. Holmstad, T. Weitkamp, C. Rau, 3D images of paper obtained by phase-contrast X-ray microtomography: image quality and binarisation, Nuclear Instruments and Methods in Physics Research Section A:

Accelerators, Spectrometers, Detectors and Associated Equipment, 490(1-2) (2002) 392-402.

[8] J. P. Feser, A. K. Prasad, S. G. Advani, Experimental characterization of in-plane permeability of gas diffusion layers, Journal of Power Sources, 162(2) (2006) 1226-1231.

[9] J. T. Gostick, M. W. Fowler, M. D. Pritzker, M. A. Ioannidis, L.M. Behra, In-plane and through-plane gas permeability of carbon fiber electrode backing layers, Journal of Power Sources, 162(1) (2006) 228-238.

[10] F. Samani, M. Kokabi, M. Soleimani, M.R. V., Fabrication and characterization of electrospun fibrous nanocomposite scaffolds based on poly(lactide-<I>co</I>-glycolide)/poly(vinyl alcohol) blends, Polymer International, (2010).

[11] M. M. Tomadakis, T.J. Robertson, Viscous permeability of random fiber structures: comparison of electrical and diffusional estimates with experimental and analytical results, Journal of Composite Materials, 39(2) (2005) 163-188.

[12] A. Faghri, Z. Guo, Challenges and opportunities of thermal management issues related to fuel cell technology and modeling, International Journal of Heat and Mass Transfer, 48(19-20) (2005) 3891-3920.

[13] J. G. Pharoah, On the permeability of gas diffusion media used in PEM fuel cells, Journal of Power Sources, 144(1) (2005) 77-82.

[14] T. V. Nguyen, A gas distributor design for proton-exchange-membrane fuel cells, Journal of The Electrochemical Society, 143(5) (1996) L103-L105.

[15] B. T. Astrom, R. B. Pipes, S.G. Advani, On flow through aligned fiber beds and its application to composites processing, Journal of Composite Materials, 26(9) (1992) 1351-1373.

[16] P.R. Waghmare, S.K. Mithra, A. Mather, J. McLaughlin, Modeling, fabrication and simulation of microfilters, in: ECI International Conference on Heat Transfer and Fluid Flow in Microscale, Whistler, Canada, 2008.

[17] C. Yu, M. H. Davey, F. Svec, J. M. J. Fréchet, Monolithic porous polymer for on-chip solid-phase extraction and preconcentration prepared by photoinitiated in situ polymerization within a microfluidic device, Analytical Chemistry, 73(21) (2001) 5088-5096.

[18] D. J. Throckmorton, T. J. Shepodd, A. K. Singh, Electrochromatography in microchips: reversed-phase separation of peptides and amino acids using photopatterned rigid polymer monoliths, Analytical Chemistry, 74(4) (2002) 784-789.

[19] H. C. Brinkman, A calculation of the viscous force exerted by a flowing fluid on a dense swarm of particles, Applied Scientific Research, 1(1) (1949) 27-34.

[20] F. A. L. Dullien, Porous media: fluid transport and pore structure, 2nd ed., Academic Press, New York, 1992.

[21] J. Happel, H. Brenner, Low Reynolds number hydrodynamics: with special applications to particulate media, 2nd ed., Martinus Nijhoff Publishers, The Hague, 1991.

[22] P.C. Carman, The determination of the specific surface of powders, Journal of the Society of Chemical Industry, 57 (1938) 225-234.

[23] B. Markicevic, A. Bazylak, N. Djilali, Determination of transport parameters for multiphase flow in porous gas diffusion electrodes using a capillary network model, Journal of Power Sources, 171(2) (2007) 706-717.

[24] A. Bazylak, V. Berejnov, B. Markicevic, D. Sinton, N. Djilali, Numerical and microfluidic pore networks: Towards designs for directed water transport in GDLs, Electrochimica Acta, 53(26) (2008) 7630-7637.

[25] O. Chapuis, M. Prat, M. Quintard, E. Chane-Kane, O. Guillot, N. Mayer, Two-phase flow and evaporation in model fibrous media: Application to the gas diffusion layer of PEM fuel cells, Journal of Power Sources, 178(1) (2008) 258-268.

[26] P. K. Sinha, C. Y. Wang, Pore-network modeling of liquid water transport in gas diffusion layer of a polymer electrolyte fuel cell, Electrochimica Acta, 52(28) (2007) 7936-7945.

[27] S. Kuwabara, The forces experienced by randomly distributed parallel circular cylinders or spheres in a viscous flow at small Reynolds numbers, Journal of Physical Society of Japan, 14 (1959) 527-532.

[28] J. Happel, Viscous flow relative to arrays of cylinders, AIChE Journal, 5(2) (1959) 174-177.

[29] H. Hasimoto, On the periodic fundamental solutions of the Stokes equations and their application to viscous flow past a cubic array of spheres, Journal of Fluid Mechanics 5(02) (1959) 317-328.

[30] E. M. Sparrow, A. L. Loeffler, Longitudinal laminar flow between cylinders arranged in regular array, AIChE Journal, 5 (1959) 325-330.

[31] A. S. Sangani , A. Acrivos, Slow flow past periodic arrays of cylinders with application to heat transfer, International Journal of Multiphase Flow, 8(3) (1982) 193-206.

[32] J. E. Drummond, M.I. Tahir, Laminar viscous flow through regular arrays of parallel solid cylinders, International Journal of Multiphase Flow, 10(5) (1984) 515-540.

[33] J. B. Keller, Viscous flow through a grating or lattice of cylinders, Journal of Fluid Mechanics 18 (1964) 94-96.

[34] B. R. Gebart, Permeability of Unidirectional Reinforcements for RTM, Journal of Composite Materials, 26(8) (1992) 1100-1133.

[35] J. Van der Westhuizen, J. P. Du Plessis, An attempt to quantify fibre bed permeability utilizing the phase average Navier-Stokes equation, Composites Part A: Applied Science and Manufacturing, 27(4) (1996) 263-269.

[36] L. Skartsis, B. Khomami, J.L. Kardos, Resin flow through fiber beds during composite manufacturing processes. Part II: Numerical and experimental studies of newtonian flow through ideal and actual fiber beds, Polymer Engineering & Science, 32(4) (1992) 231-239.

[37] M. P. Sobera, C.R. Kleijn, Hydraulic permeability of ordered and disordered single-layer arrays of cylinders, Physical Review E, 74(3) (2006) 036301.

[38] M. Sahraoui, M. Kaviany, Slip and no-slip velocity boundary conditions at interface of porous, plain media, International Journal of Heat and Mass Transfer, 35(4) (1992) 927-943.

[39] A. S. Sangani, C. Yao, Transport processes in random arrays of cylinders. II. Viscous flow, Physics of Fluids, 31(9) (1988) 2435-2444.

[40] J. J. L. Higdon, G.D. Ford, Permeability of three-dimensional models of fibrous porous media, Journal of Fluid Mechanics 308(-1) (1996) 341-361.

[41] D. S. Clague, R. J. Phillips, A numerical calculation of the hydraulic permeability of three-dimensional disordered fibrous media, Physics of Fluids, 9(6) (1997) 1562-1572.

[42] D. S. Clague, B. D. Kandhai, R. Zhang, P. M. A. Sloot, Hydraulic permeability of (un)bounded fibrous media using the lattice Boltzmann method, Physical Review E, 61(1) (2000) 616-625.

[43] K. Boomsma, D. Poulikakos, Y. Ventikos, Simulations of flow through open cell metal foams using an idealized periodic cell structure, International Journal of Heat and Fluid Flow, 24(6) (2003) 825-834.

[44] M. Palassini, A. Remuzzi, Numerical analysis of viscous flow through fibrous media: a model for glomerular basement membrane permeability, American Journal of Physiology- Renal Physiology, 274(1) (1998) F223-231.

[45] T. Stylianopoulos, A. Yeckel, J. J. Derby, X. J. Luo, M. S. Shephard, E. A. Sander, V. H. Barocas, Permeability calculations in three-dimensional isotropic and oriented fiber networks, Physics of Fluids, 20(12) (2008) 123601.

[46] M. A. Tahir, H.V. Tafreshi, Influence of fiber orientation on the transverse permeability of fibrous media, Physics of Fluids, 21(8) (2009) 083604.

[47] A. Koponen, D. Kandhai, E. Hellén, M. Alava, A. Hoekstra, M. Kataja, K. Niskanen, P. Sloot, J. Timonen, Permeability of three-dimensional random fiber webs, Physical Review Letters, 80(4) (1998) 716-719.

[48] S. Zobel, B. Maze, H. Vahedi Tafreshi, Q. Wang, B. Pourdeyhimi, Simulating permeability of 3-D calendered fibrous structures, Chemical Engineering Science, 62(22) (2007) 6285-6296.

[49] L. Hao, P. Cheng, Lattice Boltzmann simulations of anisotropic permeabilities in carbon paper gas diffusion layers, Journal of Power Sources, 186(1) (2009) 104-114.

[50] A. Nabovati, E. W. Llewellin, A.C.M. Sousa, A general model for the permeability of fibrous porous media based on fluid flow simulations using the lattice Boltzmann method, Composites Part A: Applied Science and Manufacturing, 40(6-7) (2009) 860-869.

[51] M. A. VanDoormaal, J.G. Pharoah, Determination of permeability in fibrous porous media using the lattice Boltzmann method with application to PEM fuel cells, International Journal for Numerical Methods in Fluids, 59(1) (2009) 75-89.

[52] G. Neale, W. Nader, Practical significance of brinkman's extension of darcy's law: Coupled parallel flows within a channel and a bounding porous medium, The Canadian Journal of Chemical Engineering, 52(4) (1974) 475-478.

[53] A. Tamayol, M. Bahrami, In-plane gas permeability of proton exchange membrane fuel cell gas diffusion layers, Journal of Power Sources, 196(7) (2011) 3559-3564.

[54] G. W. Jackson, D.F. James, The permeability of fibrous porous media, The Canadian Journal of Chemical Engineering, 64(3) (1986) 364-374.

[55] K. J. Mattern, W.M. Deen, Mixing rules for estimating the hydraulic permeability of fiber mixtures, AIChE Journal, 54(1) (2008) 32-41.

[56] S. R. Eisenberg, A. J. Grodzinsky, Electrokinetic micromodel of extracellular matrix and other polyelectrolyte networks, Physicochemical Hydrodynamics, 10 (1988) 517-539.

[57] D. L. Johnson, J. Koplik, L. M. Schwartz, New pore-size parameter characterizing transport in porous media, Physical Review Letters, 57(20) (1986) 2564-2567

[58] M. M. Tomadakis, S.V. Sotirchos, Transport properties of random arrays of freely overlapping cylinders with various orientation distributions, The Journal of Chemical Physics, 98(1) (1993) 616-626.

[59] E. J. Wiggins, W. B. Campbell, O. Mass, Determination of the Specific surface of fibrous materials, The Canadian Journal of Research

17 (1939) 318-324.

[60] R. R. Sullivan, Specific surface measurements on compact bundles of parallel fibers, Journal of Applied Physics, 13(11) (1942) 725-730.

[61] O. P. Bergelin, G. A. Brown, H. L. Hull, F. W. Sullivan, Heat transfer and fluid friction during viscous flow across banks of tubes–III. A study of tube spacing and tube size, ASME Transactions, 72 (1950) 881–888.

[62] C. N. Davies, The Separation of Airborne Dust and Particles, in: The Institution of Mechanical Engineers, London, 1952, pp. 185–213.

[63] A. A. Kirsch, N.A. Fuchs, Studies on fibrous aerosol filters--II. pressure drops in systems of parallel cylinders, Annals of Occupational Hygiene, 10(1) (1967) 23-30.

[64] A. G. Kostornov, M.S. Shevchuk, Hydraulic characteristics and structure of porous metal fiber materials, Powder Metallurgy and Metal Ceramics, 16(9) (1977) 694-699.

[65] D. F. James, G. W. Jackson, The hydrodynamic resistance of hyaluronic acid and its contribution to tissue permeability, Biorhelogy, 19 (1982) 317-330.

[66] T. G. Gutowski, Z. Cai, S. Bauer, D. Boucher, J. Kingery, S. Wineman, Consolidation experiments for laminate composites, Journal of Composite Materials, 21(7) (1987) 650-669.

[67] C. Chmielewski, K. Jayaraman, The effect of polymer extensibility on crossflow of polymer solutions through cylinder arrays, Journal of Rheology, 36(6) (1992) 1105-1126.

[68] B. Khomami, L.D. Moreno, Stability of viscoelastic flow around periodic arrays of cylinders, Rheologica Acta, 36(4) (1997) 367-383.

[69] O. Rahli, L. Tadrist, M. Miscevic, R. Santini, Fluid flow through randomly packed monodisperse fibers: The Kozeny-Carman parameter analysis, Journal of Fluids Engineering, 119(1) (1997) 188-192.

[70] C. H. Shih, L.J. Lee, Effect of fiber architecture on permeability in liquid composite molding, Polymer Composites, 19(5) (1998) 626-639.

[71] W. Zhong, I. Currie, D. James, Creeping flow through a model fibrous porous medium, Experiments in Fluids, 40(1) (2006) 119-126.

[72] M. V. Williams, E. Begg, L. Bonville, H. R. Kunz, J.M. Fenton, Characterization of gas diffusion layers for PEMFC, Journal of The Electrochemical Society, 151(8) (2004) A1173-A1180.

[73] J. Ihonen, M. Mikkola, G. Lindbergh, Flooding of gas diffusion backing in PEFCs, Journal of The Electrochemical Society, 151(8) (2004) A1152-A1161.

[74] B. Mueller, T. A. Zawodzinski, J. Bauman, F. Uribe, S. Gottesfeld, Carbon cloth diffusion backings for high performance PEFC cathodes, in: T. F. Fuller, S. Gottesfeld (Eds.) The Second International Symposium on Proton Conducting Membrane Fuel Cells, 1999, pp. 1-9.

[75] M. Prasanna, H. Y. Ha, E. A. Cho, S. A. Hong, I.H. Oh, Influence of cathode gas diffusion media on the performance of the PEMFCs, Journal of Power Sources, 131(1-2) (2004) 147-154.

[76] M. F. Mathias, J. Roth, J. Fleming, W. Lehnert, Diffusion media materials and characterization, in: W. Vielstich, H. A. Gasteiger, A. Lamm (Eds.) Handbook of Fuel Cells—Fundamentals, Technology and Applications, John Wiley & Sons New York, 2003, pp. 517–537.

[77] L. Cindrella, A. M. Kannan, J. F. Lin, K. Saminathan, Y. Ho, C. W. Lin, J. Wertz, Gas diffusion layer for proton exchange membrane fuel cells--A review, Journal of Power Sources, 194(1) (2009) 146-160.

[78] W. A. Khan, J. R. Culham, M.M. Yovanovich, Convection heat transfer from tube banks in crossflow: Analytical approach, International Journal of Heat and Mass Transfer, 49(25-26) (2006) 4831-4838.

[79] D. Nagelhout, M. S. Bhat, J. C. Heinrich, D.R. Poirier, Permeability for flow normal to a sparse array of fibres, Anglais, 191(1-2) (1995) 203-208.

[80] A. R. Martin, C. Saltiel, W. Shyy, Frictional losses and convective heat transfer in sparse, periodic cylinder arrays in cross flow, International journal of heat and mass transfer, 41(15) (1998) 2383-2397.

[81] S. L. Lee, J.H. Yang, Modeling of Darcy-Forchheimer drag for fluid flow across a bank of circular cylinders, International journal of heat and mass transfer, 40(13) (1997) 3149-3155.

[82] D. L. Koch, A.J.C. Ladd, Moderate Reynolds number flows through periodic and random arrays of aligned cylinders, Journal of Fluid Mechanics, 349(-1) (1997) 31-66.

[83] D. A. Edwards, M. Shapiro, P. Bar-Yoseph, M. Shapira, The influence of Reynolds number upon the apparent permeability of spatially periodic arrays of cylinders, Physics of Fluids A: Fluid Dynamics, 2(1) (1990) 45-55.

[84] C. K. Ghaddar, On the permeability of unidirectional fibrous media: A parallel computational approach, Physics of Fluids, 7(11) (1995) 2563-2586.

[85] T. D. Papathanasiou, B. Markicevic, E.D. Dendy, A computational evaluation of the Ergun and Forchheimer equations for fibrous porous media, Physics of Fluids, 13(10) (2001) 2795-2804.

[86] X. Rong, G. He, D. Qi, Flows with inertia in a three-dimensional random fiber network, Chemical Engineering Communications, 194 (2007) 398-406.

[87] F.P. Incropera, D.P. De Witt, Fundamentals of heat and mass transfer, 4th edition ed., J. Wiley & Sons, 1996.

[88] O. P. Bergelin, G. A. Brown, S. C. Doberstein, Heat transfer and fluid friction during flow across banks of tubes-IV: A study of the transition zone between viscous and turbulent flow, ASME Journal of Heat Transfer, 74(953-959) (1952).

[89] M. L. Hunt, C.L. Tien, Effects of thermal dispersion on forced convection in fibrous media, International Journal of Heat and Mass Transfer, 31(2) (1988) 301-309.

[90] V. V. Calmidi, R.L. Mahajan, Forced convection in high porosity metal foams, Journal of Heat Transfer, 122(3) (2000) 557-565.

[91] K. Boomsma, D. Poulikakos, F. Zwick, Metal foams as compact high performance heat exchangers, Mechanics of Materials, 35(12) (2003) 1161-1176.

[92] K. Boomsma, D. Poulikakos, The effects of compression and pore size variations on the liquid flow characteristics in metal foams, Journal of Fluids Engineering, 124(1) (2002) 263-272.

[93] J. J. Hwang, G. J. Hwang, R. H. Yeh, C.H. Chao, Measurement of interstitial convective heat transfer and frictional drag for flow across metal foams, Journal of Heat Transfer, 124(1) (2002) 120-129.

[94] A. Bhattacharya, V. V. Calmidi, R.L. Mahajan, Thermophysical properties of high porosity metal foams, International Journal of Heat and Mass Transfer, 45(5) (2002) 1017-1031.

[95] S. Y. Kim, J. W. Paek, B. H. Kang, Thermal performance of aluminum-foam heat sinks by forced air cooling, Components and Packaging Technologies, 26(1) (2003) 262-267.

[96] P. Khayargoli, V. Loya, L. P. Lefebvre, M. Medraj, The impact of microstructure on the permeability of metalfoams, in: CSME Forum 2004 2004, pp. 220-228.

[97] J. P. Bonnet, F. Topin, L. Tadrist, Flow laws in metal foams: compressibility and pore size effects, Transport in Porous Media, 73(2) (2008) 233-254.

[98] N. Dukhan, Correlations for the pressure drop for flow through metal foam, Experiments in Fluids, 41(4) (2006) 665-672.

[99] N. Dukhan, K. C. Chen, Heat transfer measurements in metal foam subjected to constant heat flux, Experimental Thermal and Fluid Science, 32(2) (2007) 624-631.

[100] N. Dukhan, R. Picon-Feliciano, A. R. Alvarez-Hernandez, Air flow through compressed and uncompressed aluminum foam: measurements and correlations, Journal of Fluids Engineering, 128(5) (2006) 1004-1012.

[101] A. Haji-Sheikh, Fully developed heat transfer to fluid flow in rectangular passages filled with porous materials, Journal of Heat Transfer, 128(6) (2006) 550-556.

[102] A. Haji-Sheikh, W. J. Minkowycz, E.M. Sparrow, Green's function solution of temperature field for flow in porous passages, International Journal of Heat and Mass Transfer, 47(22) (2004) 4685-4695.

[103] A. V. Kuznetsov, M. Xiong, D.A. Nield, Thermally developing forced convection in a porous medium: circular duct with walls at constant temperature, with longitudinal

conduction and viscous dissipation effects, Transport in Porous Media, 53(3) (2003) 331-345.

[104] K. Hooman A superposition approach to study slip-flow forced convection in straight microchannels of uniform but arbitrary cross-section, International Journal of Heat and Mass Transfer, 51(15-16) (2008) 3753-3762.

[105] K. Hooman, Slip flow forced convection in a microporous duct of rectangular cross-section, Applied Thermal Engineering, 29(5-6) (2009) 1012-1019.

[106] A. Kosar, C. Mishra, Y. Peles, Laminar flow across a bank of low aspect ratio micro pin fins, Journal of Fluids Engineering, 127(3) (2005) 419-430.

[107] S. Vanapalli, H. J. M. ter Brake, H. V. Jansen, J. F. Burger, H. J. Holland, T. T. Veenstra, M.C. Elwenspoek, Pressure drop of laminar gas flows in a microchannel containing various pillar matrices, Journal of Micromechanics and Microengineering, 17(7) (2007) 1381.

[108] J. Yeom, D. D. Agonafer, J. H. Han, M.A. Shannon, Low Reynolds number flow across an array of cylindrical microposts in a microchannel and figure-of-merit analysis of micropost-filled microreactors, Journal of Micromechanics and Microengineering, 19(6) (2009) 065025.

[109] G. S. Beavers, D. D. Joseph, Boundary conditions at a naturally permeable wall, Journal of Fluid Mechanics, 30(01) (1967) 197-207.

[110] K. Vafai, S. J. Kim, On the limitations of the Brinkman-Forchheimer-extended Darcy equation, International Journal of Heat and Fluid Flow, 16(1) (1995) 11-15.

[111] A. V. Kuznetsov, Analytical studies of forced convection in partly porous configurations, in: K. Vafai (Ed.) Handbook of Porous Media, New York, 2000, pp. 269-312.

[112] A. M. J. Davis, D. F. James, Penetration of shear flow into an array of rods aligned with the flow, The Canadian Journal of Chemical Engineering, 82(6) (2004) 1169-1174.

[113] M. F. Tachie, D. F. James, I. G. Currie, Slow flow through a brush, Physics of Fluids, 16(2) (2004) 445-451.

[114] M. Agelinchaab, M. F. Tachie, D. W. Ruth, Velocity measurement of flow through a model three-dimensional porous medium, Physics of Fluids, 18(1) (2006) 017105.

[115] J. K. ARTHUR, D. W. RUTH, M. F. TACHIE, PIV measurements of flow through a model porous medium with varying boundary conditions, Journal of Fluid Mechanics, 629 (2009) 343-374.

[116] J. A. Ochoa-Tapia, S. Whitaker, Momentum transfer at the boundary between a porous medium and a homogeneous fluid--I. Theoretical development, International Journal of Heat and Mass Transfer, 38(14) (1995) 2635-2646.

[117] B. Alazmi, K. Vafai, Analysis of fluid flow and heat transfer interfacial conditions between a porous medium and a fluid layer, International Journal of Heat and Mass Transfer, 44(9) (2001) 1735-1749.

[118] F. M. White, Fluid mechanics, 5th ed., McGraw-Hill Higher Education, 2003

[119] M. Bahrami, M. M. Yovanovich, J.R. Culham, Pressure drop of fully-developed, laminar flow in microchannels of arbitrary cross-Section, Journal of Fluids Engineering, 128(5) (2006) 1036-1044.

[120] T. A. K. Sadiq, S. G. Advani, R.S. Parnas, Experimental investigation of transverse flow through aligned cylinders, International Journal of Multiphase Flow, 21(5) (1995) 755-774.

[121] A. Tamayol, M. Bahrami, Analytical determination of viscous permeability of fibrous porous media, International Journal of Heat and Mass Transfer, 52(9-10) (2009) 2407-2414.

[122] Fluent 6.3 User's Guide, in, Fluent Inc., Lebanon, USA, 2007.

[123] H. K. Versteeg, W. Malalasekera, An introduction to computational fluid dynamics, Longman Scientific and Technical, Essex, UK, 1995.

[124] A. Tamayol, M. Bahrami, Laminar flow in microchannels with noncircular cross section, Journal of Fluids Engineering, 132(11) (2010) 111201.

[125] F.S. Shit, Laminar flow in axisymmetric conduits by a rational approach, The Canadian Journal of Chemical Engineering, 45(5) (1967) 285-294.

[126] A. Tamayol, M. Bahrami, Laminar flow in microchannels with noncircular cross section, Journal of Fluids Engineering, 132(11) (2010) 111201.

[127] D. A. Nield, A. Bejan, Convection in porous media, 2nd ed., Springer-Verlag, New York, 1999.

[128] B. P. Boudreau, The diffusive tortuosity of fine-grained unlithified sediments, Geochimica et Cosmochimica Acta, 60(16) (1996) 3139-3142.

[129] L. Shen, Z. Chen, Critical review of the impact of tortuosity on diffusion, Chemical Engineering Science, 62(14) (2007) 3748-3755.

[130] G. E. Archie, The Electrical Resistivity Log as an Aid in Determining Some Reservoir Characteristics Transactions of AIME, 146 (1942) 54-62.

[131] M. Akbari, D. Sinton, M. Bahrami, Pressure drop in rectangular microchannels as compared with theory based on arbitrary cross section, Journal of Fluids Engineering, 131(4) (2009) 041202-041201-041208.

[132] J. A. Molnar, L. Trevino, L. J. Lee, Liquid flow in molds with percolated fiber mats, Polymer Composites, 10(6) (1989) 414–423.

[133] J. R. Taylor, An introduction to error analysis: The study of uncertainties in physical measurements, Second ed., University Science Books,, Sausalito, USA, 1997.

[134] A. Z. Weber, J. Newman, Modeling transport in polymer-electrolyte fuel cells, Chemical Reviews, 104(10) (2004) 4679-4726.

[135] A. Tamayol, M. Bahrami, Transverse permeability of fibrous porous media Physical Review E, In Press (2011).

[136] R. C. Givler, S.A. Altobelli, A determination of the effective viscosity for the Brinkman–Forchheimer flow model, Journal of Fluid Mechanics 258(1) (1994) 355-370.

[137] A. Tamayol, K. Hooman, M. Bahrami, Thermal analysis of flow in a porous medium over a permeable stretching wall, Transport in Porous Media, 85(3) (2010) 661-676.

[138] K. Hooman, A. A. Merrikh, Analytical solution of forced convection in a duct of rectangular cross section saturated by a porous medium, Journal of Heat Transfer, 128(6) (2006) 596-600.

[139] J. C. McDonald, D. C. Duffy, J. R. Anderson, D. T. Chiu, H. Wu, O. J. A. Schueller, G.M. Whitesides, Fabrication of microfluidic systems in poly(dimethylsiloxane), Electrophoresis, 21(1) (2000) 27-40.

[140] D. Erickson, D. Sinton, D. Li, Joule heating and heat transfer in poly(dimethylsiloxane) microfluidic systems, Lab on a Chip, 3 (2003) 141-149.

[141] R.F. Probstein, Physicochemical hydrodynamics: An introduction, 2nd ed., John Wiley & Sons Inc., New York, 1994.

[142] M. A. Holden, S. Kumar, A. Beskok, P. S. Cremer, Microfluidic diffusion diluter: bulging of PDMS Microchannels under pressure driven flow, Journal of Micromechanics and Microengineering, 13 (2003) 412–418.

[143] D.A. Nield, A.V. Kuznetsov, Forced convection in porous media: transverse heterogeneity effects and thermal development, in: K. Vafai (Ed.) Handbook of Porous Media, Taylor and Francis,, New York,, 2005, pp. 143-193.

APPENDIX A: EXPERIMENTAL DATA COLLECTED FROM DIFFERENT SOURCES

The experimental and numerical data that are used in various sections of the dissertation are listed in Table 19-Table 24. Other information, such as the tested materials, working fluid, and the range of Reynolds numbers are provided in Table 3 for all the listed data.

Table 19: Summary of the experimental data used in the dissertation for normal permeability of 1D ordered arrangements of fibers.

Authors	Porosity (ε)	Dimensionless permeability (K/d^2)
Sadiq et al. (1995)	0.386	0.0007
	0.415	0.0013
	0.488	0.0030
	0.514	0.0039
	0.592	0.0098
	0.611	0.0100
Bergelin et al. (1950)	0.418	0.0015
	0.496	0.0024
	0.597	0.0088
	0.650	0.0120
Kirsch and Fuchs (1967)	0.699	0.0329
	0.798	0.0792
	0.848	0.1472
	0.888	0.2405
	0.933	0.6255
	0.953	1.0761
	0.963	1.4674
	0.980	4.3425
	0.988	9.6748
	0.992	19.9407
Chemielewski and Jayaraman (1992)	0.700	0.027

Khomami and Moreno (1997)	0.450	0.005
	0.860	0.128
Zhong et al. (2006)	0.900	0.308
	0.950	0.952
	0.975	2.857
Skartsis et al. (1992)	0.455	0.0015
	0.68	0.024
Higdon and Ford (1996), numerical	0.99	9.773
	0.95	0.998
	0.9	0.313
	0.8	0.077
	0.7	0.027
	0.6	0.011
	0.5	0.004
	0.4	0.00145
	0.3	0.00041
	0.25	0.00018
	0.215	0.00009

Table 20: Summary of the experimental and numerical data used in the dissertation for parallel permeability of 1D ordered arrangements of fibers.

Authors	Porosity (ε)	Dimensionless permeability (K/d^2)
Sangani and Yao (1988), numerical	0.3	0.0002
	0.5	0.0011
	0.7	0.0058
	0.9	0.0638
Sullivan (1942)	0.215	0.0012
	0.091	0.00008
Skartsis et al. (1992)	0.4373	0.00827

Table 21: Summary of the experimental and numerical data used in the dissertation for parallel permeability of 2D materials including GDLs.

Authors	Porosity (ε)	Dimensionless permeability (K/d^2)
Gostick et al. (2006)	0.735	0.0334
	0.762	0.0400
	0.778	0.0509
	0.811	0.0776
	0.828	0.1130
	0.849	0.1839
	0.859	0.2453
	0.732	0.0622
	0.76	0.0777
	0.773	0.0928
	0.787	0.1384
	0.808	0.1848
	0.645	0.0358
	0.685	0.0466
	0.731	0.0790
	0.755	0.0943
	0.773	0.1149
	0.783	0.1464
	0.791	0.1746
Feser et al. (2006)	0.71	0.052
	0.73	0.069
	0.76	0.087
	0.77	0.113
Shi and Lee (1998)	0.56	0.0063
	0.57	0.0081
	0.64	0.0199
	0.69	0.0311

Table 22: Summary of the experimental data used in the dissertation for normal permeability of 2D materials including GDLs.

Authors	Porosity (ε)	Dimensionless permeability (K/d^2)
Molnar (1989)	0.825	0.0974
	0.847	0.1095
	0.872	0.1231
	0.893	0.1451
	0.919	0.2162

Authors	Porosity (ε)	Dimensionless permeability (K/d^2)
Davies (1952)	0.779	0.0654
	0.808	0.1021
	0.83	0.1321
	0.85	0.1750
	0.87	0.2162
	0.88	0.1835
	0.90	0.3375
	0.90	0.4168
	0.90	0.5269
	0.91	0.4686
	0.91	0.3454
	0.92	0.5394
	0.92	0.6209
	0.92	0.5394
Gostick et al. (2006)	0.88	0.423
	0.81	0.216
	0.84	0.268
	0.85	0.110
	0.8	0.102
Zobel et al. (2007)	0.965	0.666
	0.962	0.586
	0.918	0.189
	0.898	0.123
	0.893	0.225
	0.872	0.097
	0.849	0.115
Kostornov and Shevchuck (1967)	0.29	0.00004
	0.36	0.00035
	0.49	0.00150
	0.59	0.00538
	0.69	0.01428
	0.29	0.00019
	0.36	0.00054
	0.49	0.00210
	0.59	0.00705
	0.69	0.01925
	0.29	0.00004

Table 23: Summary of the experimental and numerical data used in the dissertation for normal permeability of 3D materials with the exception of metalfoams.

Authors	Porosity (ε)	Dimensionless permeability (K/d^2)
Carman (1937)	0.681	0.035
	0.688	0.040
	0.722	0.0585
	0.731	0.0613
	0.757	0.0805
	0.765	0.09475
Rahli et al. (1997)	0.600	0.013
	0.640	0.022
	0.700	0.041
	0.739	0.081
	0.769	0.119
	0.800	0.163
	0.840	0.345
	0.851	0.409
	0.890	0.864
Jackson and James (1982)	0.9896	18.75
	0.99379	29.25
	0.99586	51
	0.99724	66.75
	0.99793	77
	0.99862	125
	0.99931	332.5
Rahli et al. (1996)	0.388	0.00083
	0.462	0.00259
	0.525	0.00440
	0.599	0.013
	0.643	0.021
	0.697	0.041
	0.739	0.079
	0.773	0.124
	0.804	0.164
	0.847	0.342
	0.896	0.803
Higdon and Ford (1996), numerical	0.9856	9.681
	0.9784	5.566
	0.9179	0.7414
	0.8762	0.3639
	0.8272	0.1933
	0.7739	0.1027
	0.7163	0.0591
	0.653	0.0339
	0.5882	0.0195

Authors	Porosity (ε)	Dimensionless permeability (K/d^2)
	0.4571	0.0059
	0.3318	0.0016
	0.2166	0.00029

Table 24: Summary of the experimental and numerical data used in the dissertation for permeability of metalfoams.

Authors	Porosity (ε)	PPI	Ligament diameter (d)	Pore diameter (d_p)	Permeability (K)
Khayargoli et al. (2004)	0.9	11.16	N.A.	1.40×10^{-3}	2.76×10^{-8}
	0.89	17.23	N.A.	9.00×10^{-4}	1.55×10^{-8}
	0.9	27.33	N.A.	6.00×10^{-4}	4.87×10^{-9}
	0.83	37.43	N.A.	5.00×10^{-4}	3.39×10^{-9}
	0.86	47.53	N.A.	4.00×10^{-4}	1.77×10^{-9}
	0.9	11.16	N.A.	1.40×10^{-3}	2.76×10^{-8}
Boomsma and Poulikakos (2002)	0.921	10	N.A.	0.0069	3.53×10^{-7}
	0.92	20	N.A.	0.0036	1.09×10^{-7}
	0.928	40	N.A.	0.0023	7.12×10^{-8}
	0.921	10	N.A.	0.0069	3.53×10^{-7}
Dukhan (2006)	0.919	10	0.000439	0.002057	1×10^{-7}
	0.915	10	0.000443	0.002053	8×10^{-8}
	0.919	20	0.000222	0.001037	6.3×10^{-8}
	0.924	20	0.00022	0.00104	5.4×10^{-8}
Bhattacharya et al. (2002)	0.9726	5	0.0005	0.00402	2.70×10^{-7}
	0.9118	5	0.00055	0.0038	1.80×10^{-7}
	0.9486	10	0.0004	0.00313	1.20×10^{-7}
	0.9138	10	0.00045	0.00328	1.10×10^{-7}
	0.8991	10	0.00043	0.0032	9.40E-08
	0.9546	20	0.0003	0.0027	1.30×10^{-7}
	0.9245	20	0.00035	0.0029	1.10×10^{-7}
	0.9005	20	0.00035	0.00258	9.00×10^{-8}
	0.9659	40	0.0002	0.0019	5.00×10^{-8}
	0.9272	40	0.00025	0.00202	6.10×10^{-8}
	0.9132	40	0.0002	0.0018	5.30×10^{-8}
	0.971	5	0.00051	0.004	2.52×10^{-7}
	0.946	5	0.00047	0.0039	2.17×10^{-7}
	0.905	5	0.00049	0.0038	1.74×10^{-7}
	0.949	10	0.00037	0.0031	1.49×10^{-7}
	0.909	10	0.00038	0.00296	1.11×10^{-7}
	0.978	20	0.00038	0.0028	1.42×10^{-7}
	0.949	20	0.00032	0.0027	1.19×10^{-7}

Authors	Porosity (ε)	PPI	Ligament diameter (d)	Pore diameter (d_p)	Permeability (K)
	0.906	20	0.00034	0.0026	8.54×10^{-8}
	0.972	40	0.00023	0.0018	5.20×10^{-8}
	0.952	40	0.00024	0.00198	5.62×10^{-8}
	0.937	40	0.00024	0.002	5.68×10^{-8}
	0.92	10	N.A.	0.00443	2.00×10^{-7}
	0.87	50	N.A.	0.0004	2.28×10^{-9}
	0.87	50	N.A.	0.000569	2.68×10^{-9}
	0.91	50	N.A.	0.000831	6.19×10^{-9}
	0.88	50	N.A.	0.00184	2.32×10^{-8}
	0.89	50	N.A.	0.002452	2.98×10^{-8}
	0.89	100	N.A.	0.002452	3.35×10^{-8}
Bonnet et al. (2008)	0.92	10	N.A.	0.00443	2.00×10^{-7}
	0.87	50	N.A.	0.0004	2.28×10^{-9}
	0.87	50	N.A.	0.000569	2.68×10^{-9}
	0.91	50	N.A.	0.000831	6.19×10^{-9}
	0.88	50	N.A.	0.00184	2.32×10^{-8}
	0.89	50	N.A.	0.002452	2.98×10^{-8}
	0.89	100	N.A.	0.002452	3.35×10^{-8}

APPENDIX B: DETAILS OF THE EXPERIMENTAL MEASUREMENTS CARRIED OUT IN THE DISSERTATION

Details of the experimental measurements for calculating flow properties of the investigated materials, described in Sections 3.5, 3.6, and 3.7, are listed in this appendix. In Table 25-Table 27 data from different trials for measuring properties of similar samples are also included. The analysis of uncertainty associated with each experiment is available in the designated section in the text.

Table 25: Summary of the measurements and calculations for determining permeability of tube banks and metalfoams; pure glycerol with viscosity of 1.4 is used as working fluid.

Porosity (ε)	Fiber diameter (*mm*)	Flow rate (*lps*$\times 10^{-7}$)	Length[*] (*mm*)	Pressure drop (*Pa*)	Reynolds number	Permeability ($K \times 10^{-7}$)
			Tube bank			
0.8	1.5	2.7	59	243.5	0.00065	1.3
0.8	1.5	65	59	601.2	0.00158	1.2
0.8	1.5	57	59	523.8	0.00138	1.2
0.8	1.5	16	59	144.7	0.00040	1.3
0.8	1.5	4.9	59	42.0	0.00012	1.3
0.8	1.5	13	59	121.9	0.00032	1.3
0.8	1.5	38	59	337.1	0.00091	1.3
0.8	1.5	6.3	52	47.1	0.00016	1.2
0.8	1.5	57	52	460.8	0.00139	1.1
0.8	1.5	32	52	251.4	0.00079	1.2
0.8	1.5	21	52	158.9	0.00051	1.2
0.8	1.5	13	52	101.1	0.00033	1.2
0.85	1.5	1.87	52	56.8	0.0005	3.42
0.85	1.5	2.89	52	90.0	0.0007	3.33
0.85	1.5	9.12	52	281.0	0.0023	3.37
0.85	1.5	5.04	52	155.1	0.0013	3.37
0.85	1.5	10.91	52	330.9	0.0027	3.42

Porosity (ε)	Fiber diameter (*mm*)	Flow rate (*lps*$\times 10^{-7}$)	Length[*] (*mm*)	Pressure drop (*Pa*)	Reynolds number	Permeability ($K \times 10^{-7}$)
0.85	1.5	12.95	52	397.4	0.0032	3.38
0.85	1.5	2.94	52	89.5	0.0007	3.41
0.85	1.5	7.40	52	222.6	0.0018	3.45
0.85	1.5	1.34	52	40.6	0.0003	3.42
0.85	1.5	4.56	52	136.6	0.0011	3.46
0.85	1.5	5.27	52	156.5	0.0013	3.50
0.85	1.5	2.27	52	67.7	0.0006	3.48
0.85	1.5	12.13	52	361.3	0.0030	3.48
0.9	1.5	4.68	80	135.6	0.0012	5.55
0.9	1.5	3.3	80	92.9	0.0008	5.73
0.9	1.5	12	80	356.5	0.0030	5.42
0.9	1.5	14.4	80	434.0	0.0036	5.36
0.9	1.5	20.3	80	620.2	0.0051	5.27
0.9	1.5	2.25	80	62.5	0.0006	5.79
0.9	1.5	5.67	80	171.7	0.0014	5.32
0.9	1.5	3.53	52	70.6	0.0009	3.33
0.9	1.5	1.12	52	21.5	0.0003	3.48
0.9	1.5	5.58	52	111.9	0.0014	3.32
0.9	1.5	8.70	52	153.6	0.0021	3.77
0.9	1.5	17.50	52	323.5	0.0043	3.60
0.9	1.5	10.97	52	201.5	0.0027	3.63
			Metalfoams			
0.929 (10)‡	0.41	9.60	52	443.9	0.00075	2.51
0.929	0.41	2.73	52	126.7	0.00021	2.50
0.929	0.41	0.82	52	30.8	0.00006	3.08
0.929	0.41	2.51	52	116.5	0.00020	2.50
0.929	0.41	5.36	52	260.8	0.00042	2.38
0.929	0.41	14.80	52	712.3	0.00116	2.41
0.929	0.41	1.95	52	84.0	0.00015	2.69
0.929	0.41	7.59	52	333.5	0.00059	2.64
0.929	0.41	7.65	52	357.7	0.00060	2.48
0.929 (10)	0.41	2.12	52	87.1	0.00017	2.71
0.929	0.41	10.56	52	527.5	0.00084	2.68
0.929	0.41	3.30	52	131.9	0.00026	2.78
0.929	0.41	7.53	52	304.3	0.00060	2.75
0.934 (20)	0.3	2.38	52	195.0	0.00013	1.48
0.934	0.3	4.17	52	363.7	0.00024	1.39
0.934	0.3	1.65	52	136.6	0.00009	1.46
0.934	0.3	0.70	52	54.9	0.00004	1.55
0.934	0.3	2.92	52	248.2	0.00017	1.43
0.934	0.3	4.88	52	421.6	0.00028	1.40
0.934	0.3	2.49	52	209.3	0.00014	1.44
0.934	0.3	7.80	52	632.1	0.00044	1.50
0.934 (20)	0.3	3.28	52	228.7	0.00020	1.61
0.934	0.3	9.42	52	668.6	0.00057	1.58

Porosity (ε)	Fiber diameter (mm)	Flow rate $(lps \times 10^{-7})$	Length[*] (mm)	Pressure drop (Pa)	Reynolds number	Permeability $(K \times 10^{-7})$
0.934	0.3	1.34	52	81.0	0.00008	1.86
0.934	0.3	5.09	52	341.8	0.00031	1.68
0.934	0.3	2.35	52	150.4	0.00014	1.76
0.934	0.3	2.93	52	249.2	0.00018	1.32
0.942 (40)	0.2	2.79	52	115.2	0.00037	0.84
0.942	0.2	2.75	52	112.4	0.00036	0.85
0.942	0.2	9.74	52	455.3	0.00129	0.74
0.942	0.2	9.08	52	422.1	0.00120	0.74
0.942	0.2	3.82	52	151.3	0.00050	0.87
0.942	0.2	6.51	52	291.4	0.00086	0.77
0.942	0.2	11.73	52	543.2	0.00155	0.75
0.942	0.2	12.47	52	555.1	0.00165	0.78
0.942 (40)	0.2	0.81	52	417.3	0.00011	0.81
0.942	0.2	0.81	52	412.6	0.00010	0.81
0.942	0.2	0.82	52	562.2	0.00014	0.82
0.942	0.2	0.80	52	745.1	0.00019	0.80
0.942	0.2	0.81	52	236.8	0.00006	0.81

[*] The distance between pressure taps.

‡ The number in the parentheses shows the PPI in metalfoam samples.

Table 26: Summary of the measurements and calculations for determining the permeability of GDLs; samples diameter is 0.0254 m.

Initial thickness (μm)	Thickness (μm)	Porosity (ε)	PTFE $(\%)$	Pressure drop (Pa)	Flow rate (lpm)	Permeability (K)
			Toray TGP 120			
380	380	0.8	0	28.6	1.5	1.30×10^{-11}
380	380	0.8	0	46.8	2	1.06×10^{-11}
380	380	0.8	0	69.0	3	1.08×10^{-11}
380	380	0.8	0	96.9	4	1.02×10^{-11}
380	380	0.8	0	128.3	5	9.64×10^{-12}
380	380	0.8	0	157.9	6	9.40×10^{-12}
368	368	0.8	0	35.9	1.5	1.00×10^{-11}
368	368	0.8	0	45.8	2	1.05×10^{-11}
368	368	0.8	0	66.3	3	1.09×10^{-11}
368	368	0.8	0	87.4	4	1.10×10^{-11}
368	368	0.8	0	114.8	5	1.04×10^{-11}
377	350	0.78	0	30.6	1.5	1.12×10^{-11}
377	350	0.78	0	47.6	2	9.58×10^{-12}
377	350	0.78	0	69.0	3	9.91×10^{-12}
377	350	0.78	0	97.7	4	9.33×10^{-12}

Initial thickness (μm)	Thickness (μm)	Porosity (ε)	PTFE (%)	Pressure drop (*Pa*)	Flow rate (*lpm*)	Permeability (K)
377	350	0.78	0	132.1	5	8.63×10^{-12}
377	350	0.78	0	173.9	6	7.86×10^{-12}
374	325	0.76	0	39.6	1.5	8.02×10^{-12}
374	325	0.76	0	50.0	2	8.46×10^{-12}
374	325	0.76	0	83.2	3	7.63×10^{-12}
374	325	0.76	0	111.8	4	7.57×10^{-12}
374	325	0.76	0	159.7	5	6.63×10^{-12}
379	285	0.73	0	49.6	1.5	5.61×10^{-12}
379	285	0.73	0	66.3	2	5.60×10^{-12}
379	285	0.73	0	102.7	3	5.42×10^{-12}
379	285	0.73	0	144.3	4	5.14×10^{-12}
379	285	0.73	0	204.1	5	4.55×10^{-12}
372	272	0.72	0	56.3	1.5	4.72×10^{-12}
372	272	0.72	0	77.2	2	4.59×10^{-12}
372	272	0.72	0	117.6	3	4.52×10^{-12}
372	272	0.72	0	164.7	4	4.30×10^{-12}
364	364	0.79	10	36.4	1.5	9.77×10^{-12}
364	364	0.79	10	47.3	2	1.00×10^{-11}
364	364	0.79	10	72.0	3	9.88×10^{-12}
364	364	0.79	10	93.7	4	1.01×10^{-11}
364	364	0.79	10	121.3	5	9.77×10^{-12}
364	364	0.79	10	150.3	6	9.47×10^{-12}
365	365	0.79	10	33.9	1.5	1.05×10^{-11}
365	365	0.79	10	46.1	2	1.03×10^{-11}
365	365	0.79	10	68.5	3	1.04×10^{-11}
365	365	0.79	10	94.7	4	1.00×10^{-11}
365	365	0.79	10	128.1	5	9.28×10^{-12}
365	365	0.79	10	160.7	6	8.87×10^{-12}
365	365	0.77	20	35.7	1.5	1.00×10^{-11}
365	365	0.77	20	45.0	2	1.06×10^{-11}
365	365	0.77	20	76.4	3	9.33×10^{-12}
365	365	0.77	20	108.1	4	8.80×10^{-12}
365	365	0.77	20	148.9	5	7.98×10^{-12}
365	365	0.77	20	203.0	6	7.03×10^{-12}
371	371	0.77	20	36.9	1.5	9.80×10^{-12}
371	371	0.77	20	50.3	2	9.57×10^{-12}
371	371	0.77	20	74.0	3	9.77×10^{-12}
371	371	0.77	20	108.9	4	8.85×10^{-12}
371	371	0.77	20	141.8	5	8.50×10^{-12}
347	347	0.76	30	54.1	1.5	6.27×10^{-12}
347	347	0.76	30	76.5	2	5.91×10^{-12}
347	347	0.76	30	121.1	3	5.60×10^{-12}
347	347	0.76	30	53.3	1.5	6.36×10^{-12}
347	347	0.76	30	78.7	2	5.74×10^{-12}

Initial thickness (μm)	Thickness (μm)	Porosity (ε)	PTFE (%)	Pressure drop (*Pa*)	Flow rate (*lpm*)	Permeability (K)
			Toray TGP 90			
267	267	0.8	0	21.6	1.5	1.02×10^{-11}
267	267	0.8	0	31.0	2	9.22×10^{-12}
267	267	0.8	0	46.2	3	8.71×10^{-12}
267	267	0.8	0	63.4	4	8.45×10^{-12}
267	267	0.8	0	86.7	5	7.76×10^{-12}
254	240	0.8	0	113.6	6	7.45×10^{-12}
254	240	0.79	0	30.6	1.5	1.09×10^{-11}
254	240	0.79	0	39.5	2	1.01×10^{-11}
254	240	0.79	0	64.1	3	1.01×10^{-11}
254	240	0.79	0	83.0	4	9.86×10^{-12}
254	240	0.79	0	114.7	5	9.02×10^{-12}
254	240	0.79	0	154.5	6	8.26×10^{-12}
260	228	0.77	0	30.6	1.5	7.27×10^{-12}
260	228	0.77	0	39.5	2	7.51×10^{-12}
260	228	0.77	0	64.1	3	6.95×10^{-12}
260	228	0.77	0	83.0	4	7.15×10^{-12}
260	228	0.77	0	114.7	5	6.47×10^{-12}
260	228	0.77	0	154.5	6	5.77×10^{-12}
267	207	0.74	0	31.7	1.5	6.38×10^{-12}
267	207	0.74	0	44.8	2	6.02×10^{-12}
267	207	0.74	0	71.2	3	5.68×10^{-12}
267	207	0.74	0	99.4	4	5.43×10^{-12}
267	207	0.74	0	142.3	5	4.74×10^{-12}
267	207	0.74	0	192.6	6	4.20×10^{-12}
255	200	0.74	0	34.6	1.5	5.65×10^{-12}
255	200	0.74	0	52.0	2	5.01×10^{-12}
255	200	0.74	0	77.4	3	5.05×10^{-12}
255	200	0.74	0	107.8	4	4.83×10^{-12}
255	200	0.74	0	149.0	5	4.37×10^{-12}
255	200	0.74	0	209.5	6	3.73×10^{-12}
			Sigracet SGL 10AA			
414	414	0.88	0	9.1	1.5	4.46×10^{-11}
414	414	0.88	0	13.3	2	4.05×10^{-11}
414	414	0.88	0	22.2	3	3.65×10^{-11}
414	414	0.88	0	32.3	4	3.33×10^{-11}
414	414	0.88	0	47.8	5	2.82×10^{-11}
414	414	0.88	0	64.3	6	2.51×10^{-11}
385	290	0.84	0	11.2	1.5	2.53×10^{-11}
385	290	0.84	0	16.0	2	2.36×10^{-11}
385	290	0.84	0	25.5	3	2.22×10^{-11}
385	290	0.84	0	37.9	4	1.99×10^{-11}
385	290	0.84	0	55.0	5	1.72×10^{-11}
385	290	0.84	0	76.6	6	1.48×10^{-11}

Initial thickness (μm)	Thickness (μm)	Porosity (ε)	PTFE (%)	Pressure drop (Pa)	Flow rate (*lpm*)	Permeability (K)
432	250	0.79	0	14.7	1.5	1.66×10^{-11}
432	250	0.79	0	20.4	2	1.60×10^{-11}
432	250	0.79	0	34.3	3	1.42×10^{-11}
432	250	0.79	0	48.0	4	1.36×10^{-11}
432	250	0.79	0	67.4	5	1.21×10^{-11}
432	250	0.79	0	95.7	6	1.02×10^{-11}
409	207	0.76	0	17.1	1.5	1.17×10^{-11}
409	207	0.76	0	26.9	2	9.92×10^{-12}
409	207	0.76	0	44.4	3	9.03×10^{-12}
409	207	0.76	0	63.8	4	8.37×10^{-12}
409	207	0.76	0	88.9	5	7.51×10^{-12}
409	207	0.76	0	125.8	6	6.37×10^{-12}

Table 27: Summary of the measurements and calculations for determining flow properties of tube banks in the moderate range of Reynolds number; the distance between pressure taps is 0.052 *m* and the fiber diameter is 1.5 *mm*.

Porosity (ε)	Darcy velocity (*m/s*)	Pressure drop (Pa)	Density (kg/m^3)	Reynolds number	$\rho U / \mu$	$\Delta P / U \mu L \times 10^6$
0.8	0.010	141.3	1182	0.48	313.2	6.88
0.8	0.012	162.7	1182	0.56	361.0	6.87
0.8	0.022	303.8	1182	1.03	671.1	6.90
0.8	0.012	158.9	1182	0.55	354.3	6.83
0.8	0.045	624.0	1182	2.11	1373.3	6.92
0.8	0.032	436.3	1182	1.48	960.2	6.92
0.8	0.039	529.5	1182	1.80	1168.0	6.91
0.8	0.022	304.3	1182	1.04	675.0	6.87
0.8	0.074	393.6	1148	10.92	7093.3	8.73
0.8	0.062	322.8	1148	9.22	5985.7	8.49
0.8	0.044	225.4	1148	6.52	4235.0	8.38
0.8	0.033	167.5	1148	4.88	3170.8	8.31
0.8	0.082	432.5	1148	12.16	7894.8	8.62
0.8	0.064	336.6	1148	9.57	6212.7	8.53
0.8	0.031	155.6	1148	4.54	2948.1	8.31
0.8	0.020	99.5	1148	2.96	1922.3	8.15
0.8	0.078	414.0	1148	11.64	7555.3	8.63
0.85	0.037	101.0	1148	3.9	2506.6	3.16
0.85	0.063	176.0	1148	6.6	4285.1	3.22
0.85	0.065	179.3	1148	6.8	4439.8	3.17
0.85	0.049	133.3	1148	5.1	3326.5	3.14
0.85	0.139	406.4	1148	14.6	9475.5	3.36
0.85	0.066	180.3	1148	6.9	4502.5	3.14

Porosity (ε)	Darcy velocity (*m/s*)	Pressure drop (*Pa*)	Density (kg/m³)	Reynolds number	$\rho U / \mu$	$\Delta P / U \mu L \times 10^6$
0.85	0.077	218.8	1148	8.1	5247.2	3.27
0.85	0.098	283.4	1148	10.3	6687.2	3.32
0.85	0.018	82.4	1182	1.1	682.0	2.68
0.85	0.052	236.8	1182	3.0	1924.5	2.73
0.85	0.069	324.7	1182	3.9	2549.9	2.83
0.85	0.017	80.0	1182	1.0	629.5	2.82
0.85	0.038	172.7	1182	2.2	1413.1	2.71
0.85	0.095	459.1	1182	5.4	3509.0	2.90
0.85	0.054	243.9	1182	3.0	1977.3	2.74
0.85	0.078	354.6	1182	4.4	2887.1	2.73
0.90	0.036	119.5	1182	1.8	1138.0	1.78
0.90	0.061	208.4	1182	3.0	1945.4	1.81
0.90	0.063	212.3	1182	3.1	2015.7	1.78
0.90	0.047	157.8	1182	2.3	1510.2	1.77
0.90	0.135	469.9	1182	6.6	4301.8	1.85
0.90	0.064	213.5	1182	3.1	2044.1	1.76
0.90	0.075	259.0	1182	3.7	2382.2	1.84
0.90	0.095	329.9	1182	4.7	3036.0	1.84
0.90	0.035	60.1	1148	3.9	2560.1	2.08
0.90	0.053	88.1	1148	5.9	3841.6	2.03
0.90	0.080	144.2	1148	8.9	5796.5	2.20
0.90	0.067	119.0	1148	7.5	4843.9	2.18
0.90	0.100	175.1	1148	11.2	7253.8	2.14
0.90	0.047	79.1	1148	5.2	3405.9	2.06
0.90	0.063	106.7	1148	7.0	4536.0	2.08
0.90	0.085	148.9	1148	9.5	6162.6	2.14

APPENDIX C: DETAILS OF THE NUMERICAL SIMULATIONS PERFORMED IN THE DISSERTATION

Numerical simulations are used in various parts of this dissertation to verify the developed theoretical models/solutions. In this appendix, more details on the numerical results and calculations are provided. Numerical grid generation and then computations for all the studied cases are carried out using Gambit and Fluent software, respectively.

Flow normal to ordered array of cylinders (Sections 3.2 and 3.7):

Although fully-developed solution for normal flow can be found by simulating a single unit cell and applying periodic boundary condition, to determine the developing length for flow in the medium, as was shown in Figure 16a, a set of 7-10 unit cells in series are considered and velocity profiles are compared at the entrance to each unit cell, see Figure 74. The pressure drops used for calculation of permeability are the values obtained from the regions with fully-developed flow.

The inlet velocity of the media is assumed to be uniform. Constant pressure boundary condition is applied at the computational domain outlet. The symmetry boundary condition is applied on the side borders of the considered unit cells; this means that normal velocity and gradient of parallel component of the velocity on the side borders are zero.

In Figure 74, the comparison of the entrance and exit velocity profile to the fourth (out of 10) unit cell with $\varepsilon = 0.9$ indicates that fully developed condition is achieved after the

third row of cylinders. It should be noted that in the unit cell with $\varepsilon = 0.9$, the distance between the fibers is larger than other cases; thus, has the longest developing length. As such, it is expected that a similar trend holds for the rest of the studied cases, i.e., the fully developed condition is achieved after the third row of cylinders.
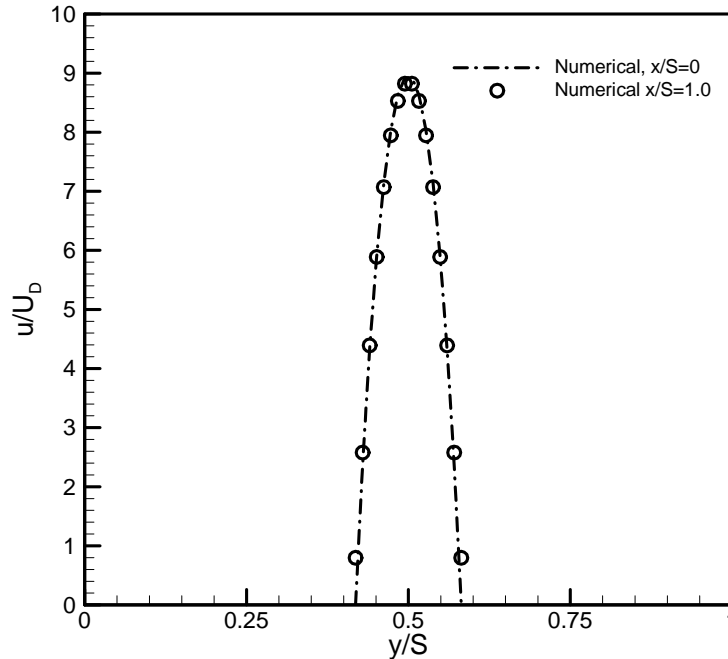
Figure 74: Developed velocity profiles in the inlet and outlet of the fourth unit cell with $\varepsilon =0.9$.

Independence of the results from numerical grid size is tested for different cases and the size of computational grid used for each geometry is selected such that the maximum difference in the predicted values for pressure gradient to be less than 2%. For example, Figure 75 illustrates the independency of the calculated values of pressure drop over a unit cell with $\varepsilon = 0.9$ after a computational grid size of 16000. Moreover, as shown in Figure 76, the numerical results are in reasonable agreement with experimental and numerical data reported by other; this also confirms the accuracy of the analysis. The summary of the calculated results is presented in Table 28. Therefore, a grid size of

15,000 – 20,000 is used through the analysis for predicting the flow properties of ordered
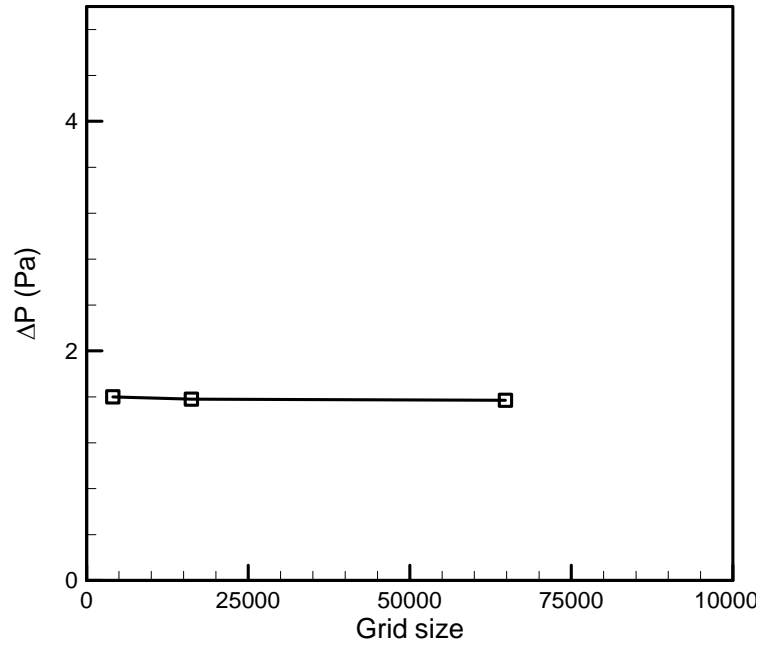
arrays of cylinders.

Figure 75: The pressure drop over a unit cell with ε =0.9 calculated with different number of grids.
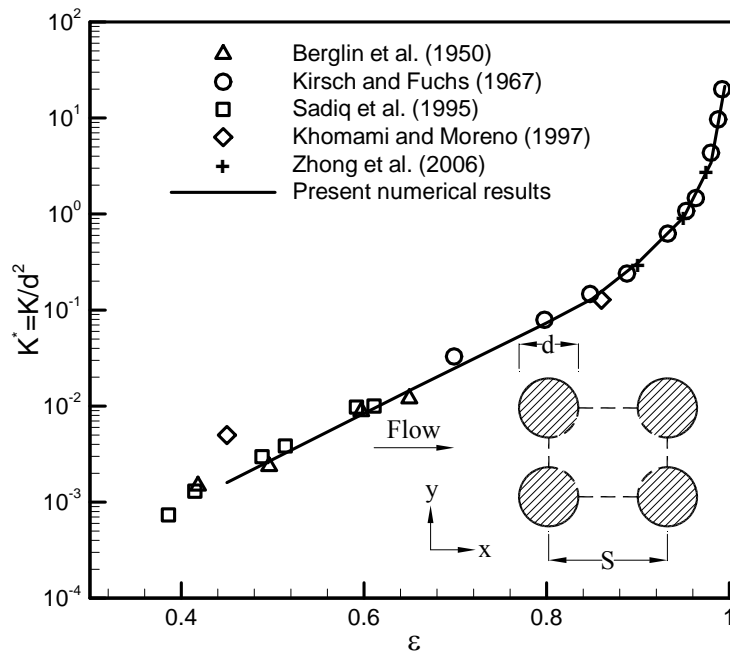

Figure 76: Comparison between the present numerical results and experimental data, normal flow through square arrays of cylinders.

171

Table 28: Important parameters for calculation of normal permeability of square arrays of fibers.

Porosity (ε)	S (cm)	d (cm)	u_{inlet} (m/s)	U_D (m/s)	ΔP (Pa)*	μ (Ns/m^2)	K (m^2)
0.45	1.195	1	0.05	0.0081	61	0.1	0.00160
0.65	1.498	1	0.05	0.0166	17.1	0.1	0.0146
0.8	1.981	1	0.05	0.0248	6.67	0.1	0.0736
0.85	2.288	1	0.05	0.0281	4.9	0.1	0.1314
0.9	2.802	1	0.05	0.0322	2.9	0.1	0.3107
0.95	3.962	1	0.05	0.0374	1.6	0.1	0.9257
0.98	6.265	1	0.05	0.0420	0.77	0.1	3.4188
0.995	12.530	1	0.05	0.0460	0.27	0.1	21.3518

* Pressure drop over the length of the unit cell, i.e., *L= S*.

Flow parallel to ordered arrays of cylinders (Sections 3.3 and 3.7):

The volume between parallel cylinders is considered as the unit cell and the computational domain, as was shown in Figure 16. Similar to normal flow through ordered arrays of cylinders, uniform velocity at the inlet, constant pressure on the computational domain outlet, and the symmetry boundary condition on the side borders of the considered unit cells are considered. Therefore, to ensure fully developed condition near the outlet of the computational domain, long cylinders are considered in the simulations.

Independency of the simulated results for parallel creeping flow through arrays of cylinders with ε = 0.9 from the numerical grid size is shown in Figure 77. Moreover, the comparison of the present computational results with the numerical results of Sangani and Yao [39] in Figure 78 confirms the accuracy of the performed computations. The summary of the calculated results is presented in Table 29.
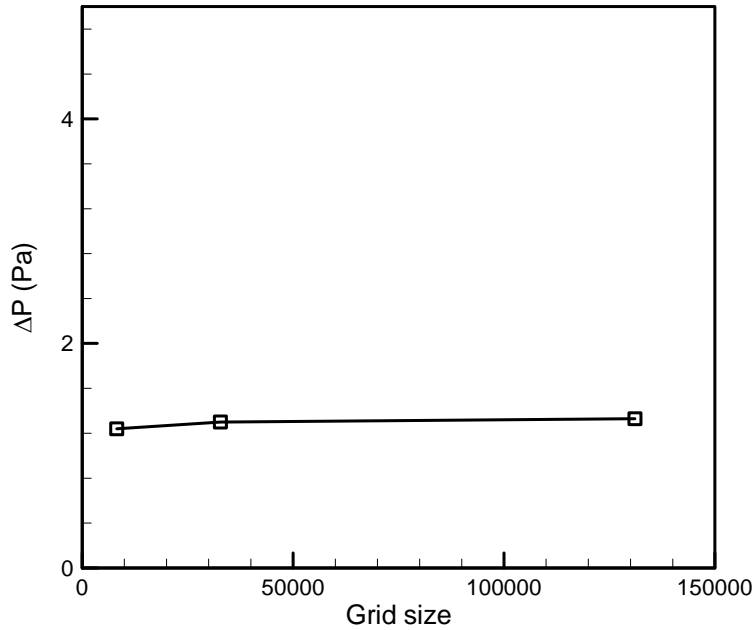
Figure 77: The pressure drop over a length of 2*cm* for square arrays of cylinders with *d*= 1 *cm* and ε =0.9 calculated with different number of grids.
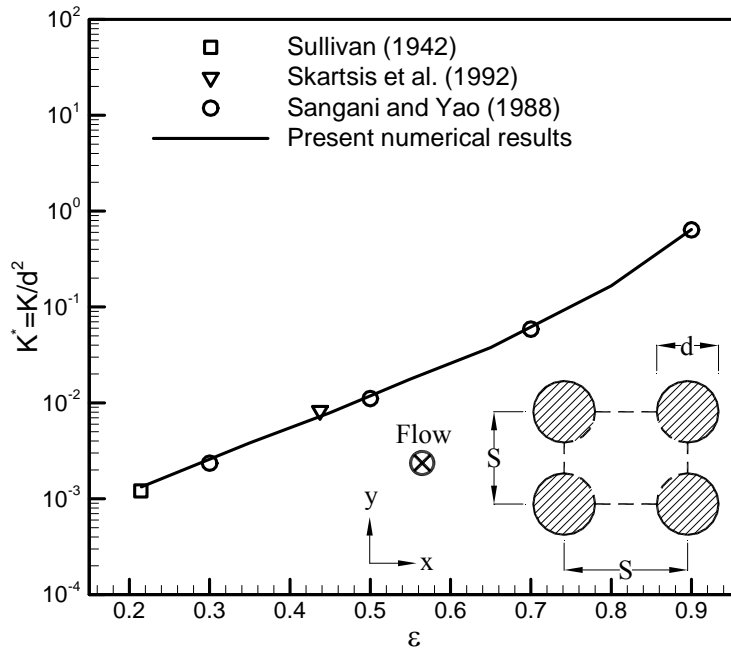

Figure 78: Comparison between the present numerical results, experimental data, and the numerical results of Sangani and Yao [39] for parallel permeability of square arrays of cylinders.

173

Table 29: The numerical results of parallel permeability in square arrays of fibers, $d = 1\,cm$ **and** $u_{inlet} = 0.05\,m/s$ **.**

ε	$S\,(cm)$	$\ell\,(cm)$	$U_D\,(m/s)$	$\Delta P\,(Pa)$	K^*
0.215	1	5	0.01075	404.3	0.0013
0.35	1.10	5	0.0175	228.7	0.0038
0.45	1.19	2	0.0225	56.8	0.0079
0.55	1.32	5	0.0275	77.6	0.0177
0.65	1.50	5	0.0325	43	0.0378
0.8	1.98	5	0.04	12	0.1667
0.9	2.80	2	0.045	1.33	0.6712

Flow parallel and normal to ordered 2D and 3D arrays of cylinders (Section 3.7):

Navier-Stokes equations are solved numerically using Fluent [122]. The second order upwind scheme is selected to discretize the governing equations and SIMPLE algorithm [123] is employed for pressure-velocity coupling. For simple cubic structures, the inlet and outlet boundaries of the computational domains are considered to be periodic, i.e., the velocity distributions on both boundaries are the same. The symmetry boundary condition is applied on the side borders of the considered unit cells; this means that normal velocity and gradient of parallel component of the velocity on the side borders are zero. However, for 3 dimensional cases, employing the periodic condition leads to a poor convergence rate. As a result of our limited computational resources, following our results for 1D structures, a set of 7-10 unit cells in series is considered and velocity profiles are compared at the entrance to each unit cell for modeling flow normal and parallel to 2D structures. For these cases, the inlet velocity of the media is assumed to be uniform. Constant pressure boundary condition is applied on the computational domain outlet. The pressure drops used for calculation of flow properties are only the values obtained from

the developed regions. Typical computational grids used in the analysis are shown in Figure 79.

In spite of the complexity of the computational domain, our analysis showed that the number of computational grids used in the analysis does not significantly affect the numerical flow-field. For example, in Figure 80, the plotted pressure drops per unit length in 3D structures calculated by two different grids confirm that grid size has a negligible effect on the numerical results over a wide range of Reynolds numbers. This is mainly a result of laminar nature of flow-field without turbulent and major recirculation regions. In addition, the very good agreement of the predicted values of permeability for SC structures with the results reported by Higdon and Ford [40], shown in Figure 54, justifies the accuracy of the present computations.

Details of the numerical results used for calculating the inertial coefficient in 1D, 2D, and 3D structures are presented in Table 30.
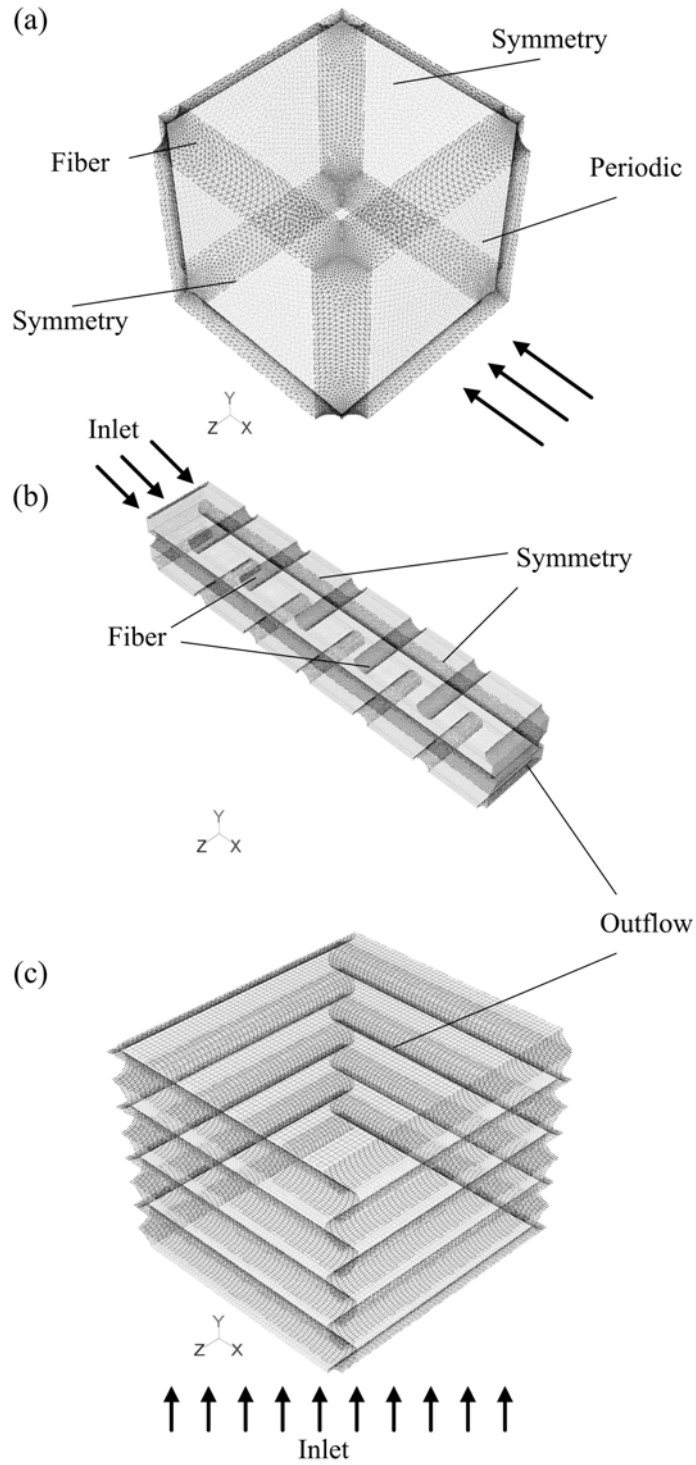
Figure 79: Typical computational domain used for modeling of flow a) through simple cubic; b) parallel to 2D; c) transverse to 2D fibrous structures.
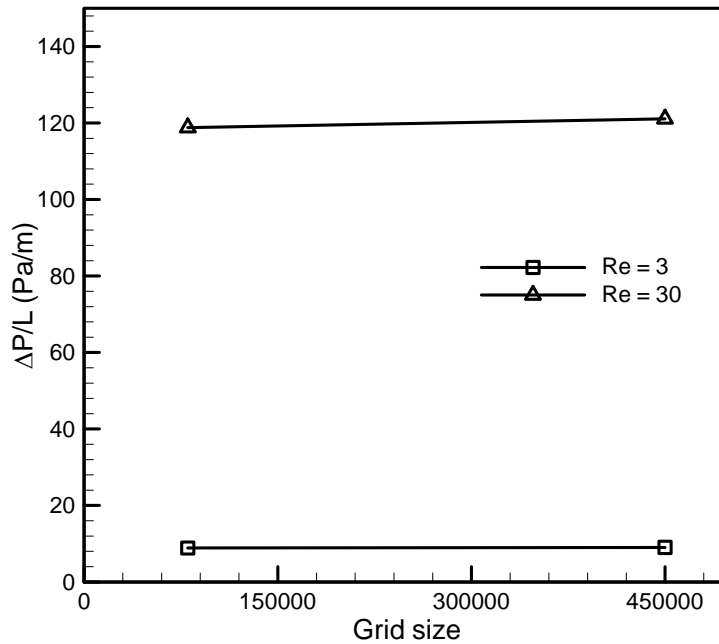
Figure 80: The pressure drop over a unit cell of simple cubic arrays of cylinders with *d*= 1 *cm* and *S* = 4 *cm* for two different Reynolds numbers, calculated with different number of grids.

Table 30: Summary of the measurements and calculation for calculating flow properties of fibrous structures in the moderate range of Reynolds number; the fiber diameter is 10 *mm*.

Porosity (ε)	Darcy velocity (*m/s*)	Pressure drop (*Pa*)	Length (*m*)	Density (*kg/m³*)	Reynolds number	$\rho U / \mu$	$\Delta P / U \mu L \times 10^6$
Normal flow, 1D structures
0.45	0.0001	0.066	0.012	100	0.008	0.8	6.81
0.45	0.0008	0.662	0.012	100	0.081	8.1	6.80
0.45	0.0081	6.700	0.012	100	0.815	81.5	6.88
0.45	0.0815	68.130	0.012	100	8.148	814.8	7.00
0.45	0.8148	965.950	0.012	100	81.48	8148.0	9.92
0.65	0.0002	0.017	0.015	100	0.02	1.7	0.68
0.65	0.0017	0.172	0.015	100	0.17	16.6	0.69
0.65	0.0166	1.72	0.015	100	1.66	166.1	0.69
0.65	0.1661	18.49	0.015	100	16.6	1661	0.74
0.65	0.3323	40.0	0.015	100	33.2	3323	0.80
0.65	0.6645	87.3	0.015	100	66.4	6645	0.88
0.65	1.6614	264.1	0.015	100	166.1	16613	1.1
0.8	0.0002	0.007	0.0198	100	0.02	2.5	0.137
0.8	0.0025	0.067	0.0198	100	0.25	24.8	0.137
0.8	0.0248	0.677	0.0198	100	2.48	247.6	0.138
0.8	0.2476	7.9	0.0198	100	24.76	2476.2	0.161
0.8	0.9905	40.3	0.0198	100	99.05	9904.9	0.206
0.8	1.4857	70.9	0.0198	100	148.57	14857.4	0.241

Porosity (ε)	Darcy velocity (*m/s*)	Pressure drop (*Pa*)	Length (*m*)	Density (*kg/m³*)	Reynolds number	$\rho U / \mu$	$\Delta P / U \mu L \times 10^6$
0.8	2.4762	142.4	0.0198	100	247.62	24762.3	0.29
0.9	0.0003	0.003	0.028	100	0.03	3.2	0.033
0.9	0.0032	0.030	0.028	100	0.32	32.2	0.033
0.9	0.0322	0.299	0.028	100	3.22	321.5	0.033
0.9	0.3215	3.43	0.028	100	32.15	3215.4	0.038
0.9	1.2862	20.51	0.028	100	128.62	12861.7	0.057
0.9	1.9293	37.90	0.028	100	192.93	19292.5	0.070
0.95	0.0004	0.0017	0.04	100	0.04	3.7	0.011
0.95	0.0037	0.0165	0.04	100	0.37	37.4	0.011
0.95	0.0374	0.168	0.04	100	3.74	373.8	0.013
0.95	0.3738	2.19	0.04	100	37.38	3738.1	0.015
0.95	0.7476	5.65	0.04	100	74.76	7476.2	0.019
Transverse flow through 2D structures							
0.35	0.00009	0.13	0.01	100	0.01	0.9	14.5
0.35	0.00862	12.54	0.01	100	0.9	86.2	14.5
0.35	0.08620	127.53	0.01	100	8.6	862.0	14.8
0.35	0.34479	638.74	0.01	100	34.5	3447.9	18.5
0.5	0.0002	0.04	0.01	100	0.02	1.8	2.17
0.5	0.0182	3.96	0.01	100	1.82	181.7	2.18
0.5	0.1817	44.50	0.01	100	18.17	1816.9	2.45
0.5	0.3634	101.49	0.01	100	36.34	3633.8	2.79
0.6	0.0002	0.0207	0.01	100	0.02	2.5	0.84
0.6	0.025	2.076	0.01	100	2.45	245.4	0.85
0.6	0.245	25.56	0.01	100	24.54	2453.5	1.04
0.6	0.491	61.2	0.01	100	49.07	4907.0	1.25
0.8	0.0004	0.0035	0.01	100	0.04	3.7	0.094
0.8	0.0373	0.364	0.01	100	3.73	372.7	0.097
0.8	0.1491	1.611	0.01	100	14.91	1490.7	0.108
0.8	0.3727	5.046	0.01	100	37.27	3726.8	0.135
0.8	0.5963	9.205	0.01	100	59.63	5962.8	0.154
Parallel flow through 2D structures							
0.5	0.000125	0.028	0.015708	100	0.012	1.25	1.43
0.5	0.0125	2.832	0.015708	100	1.25	125	1.44
0.5	0.125	30.54	0.015708	100	12.5	1250	1.56
0.5	0.5	138.2	0.015708	100	50	5000	1.76
0.6	0.00015	0.018	0.0196	100	0.015	1.5	0.61
0.6	0.015	1.8	0.0196	100	1.5	150	0.61
0.6	0.15	19.38	0.0196	100	15	1500	0.66
0.6	0.3	41.05	0.0196	100	30	3000	0.70
0.8	0.02	10.21	0.03927	10	0.02	2	0.130
0.8	0.0002	0.00973	0.03927	100	0.02	2	0.124
0.8	0.2	11.98	0.03927	100	20	2000	0.153
0.8	0.12	7.07	0.03927	100	12	1200	0.150
0.8	0.8	60.45	0.03927	100	80	8000	0.192
0.9	0.000225	0.00425	0.07854	100	0.0225	2.25	0.0241

Porosity (ε)	Darcy velocity (*m/s*)	Pressure drop (*Pa*)	Length (*m*)	Density (*kg/m³*)	Reynolds number	$\rho U / \mu$	$\Delta P / U \mu L \times 10^6$
0.9	0.0225	0.429	0.07854	100	2.25	225	0.0243
0.9	0.225	5.602	0.07854	100	22.5	2250	0.0317
0.9	0.45	12.79	0.07854	100	45	4500	0.0362
Flow through simple cubic (3D) fiber arrangements							
0.37	0.015	0.37	100	0.0006	0.0556	5.6	4.39
0.37	0.015	3.69	100	0.0056	0.5556	55.6	4.42
0.37	0.015	41.88	100	0.0556	5.5556	555.6	5.03
0.37	0.015	61.73	100	0.0778	7.7778	777.8	5.29
0.59	0.000125	0.01	0.02	100	0.0125	1.25	0.58
0.59	0.00125	0.14	0.02	100	0.125	12.5	0.58
0.59	0.025	3.00	0.02	100	2.5	250	0.60
0.59	0.1	13.66	0.02	100	10	1000	0.68
0.79	0.00002	0.001	0.03	100	0.002	0.22	0.085
0.79	0.002	0.057	0.03	100	0.22	22.22	0.085
0.79	0.022	0.59	0.03	100	2.22	222.22	0.088
0.79	0.222	7.58	0.03	100	22.22	2222.22	0.11
0.79	0.311	11.27	0.03	100	31.11	3111.11	0.12
0.87	0.00003	0.0003	0.04	100	0.003	0.28	0.030
0.87	0.003	0.03	0.04	100	0.28	28.13	0.030
0.87	0.03	0.36	0.04	100	2.81	281.2	0.032
0.87	0.28	4.75	0.04	100	28.13	2812.5	0.042
0.87	0.45	8.62	0.04	100	45	4500	0.048